Higgs Boson Phenomenology at the LHC:
the Standard Model and Beyond

by

Sze Ching Leung

B.S. in Physics, Hong Kong University of Science and Technology, 2017

Submitted to the Graduate Faculty of
the Dietrich School of Arts and Sciences in partial fulfillment
of the requirements for the degree of

Doctor of Philosophy

University of Pittsburgh

2023

UNIVERSITY OF PITTSBURGH

DIETRICH SCHOOL OF ARTS AND SCIENCES

This dissertation was presented

by

Sze Ching Leung

It was defended on

April 20, 2023

and approved by

Tao Han, Distinguished Professor, University of Pittsburgh

Adam Leibovich, Professor and Arts and Sciences Associate Dean, University of Pittsburgh

Joseph Boudreau, Professor, University of Pittsburgh

Xiao-lun Wu, Professor, University of Pittsburgh

Ming Chen, Associate Professor, University of Pittsburgh

Dissertation Director: Tao Han, Distinguished Professor, University of Pittsburgh

Higgs Boson Phenomenology at the LHC: the Standard Model and Beyond

Sze Ching Leung, PhD

University of Pittsburgh, 2023

This thesis focuses on exploring the interactions of the Higgs boson with other particles and their connections to Beyond the Standard Model (BSM) physics at the future High Luminosity LHC (HL-LHC). Four studies are presented to probe the Higgs boson couplings at high energy scales and test for new physics effects.

In Chapter 2, a novel search strategy is proposed to study the Higgs decay $H \to c\bar{c}$ in association with vector boson fusion (VBF) jets and a photon. The photon acts as an effective trigger handle, suppressing the challenging QCD background. The projected sensitivity for $H \to c\bar{c}$ at HL-LHC is about 13 times the SM charm-Yukawa coupling.

Chapter 3 explores the sensitivity to off-shell Higgs boson measurements in the process $pp \to H^* \to Z(l^+l^-)Z(\nu\bar{\nu})$ at HL-LHC. Machine-learning techniques are employed to enhance the sensitivity, leading to significant results beyond existing literature.

In Chapter 4, the $pp \to t\bar{t}H$ process at the HL-LHC is used to probe the coupling between the Higgs boson and the top quark at high energy scales. The study focuses on the boosted Higgs regime with jet substructure techniques, resulting in a strong sensitivity to the new physics scale.

Chapter 5 investigates the sensitivity to high momentum Higgs boson production through VBF. We show that even with the challenging channel $H \to b\bar{b}$, new physics up to TeV scale can be reached at the HL-LHC. We also first point out that comparable sensitivity can be obtained with the VBF jet kinematics without reconstructing the Higgs boson.

Table of Contents

Preface . . . xiii

1.0 Introduction . . . 1

1.1 Overview of the Standard Model . . . 1

1.1.1 Gauge sector . . . 5

1.1.2 Fermion sector . . . 6

1.2 The Higgs Mechanism . . . 8

1.2.1 Higgs sector . . . 8

1.2.2 Yukawa sector . . . 13

1.3 Experimental Status of the Higgs Boson . . . 16

1.3.1 Production of the Higg boson . . . 16

1.3.2 Decay of the Higgs boson . . . 19

2.0 Higgs to Charm Quarks in Vector Boson Fusion Plus a Photon . . . 25

2.1 Proposed search strategy . . . 28

2.1.1 Monte Carlo simulation . . . 29

2.1.2 Proposed trigger strategy . . . 30

2.2 Analyses and results . . . 31

2.2.1 Cut-based analysis . . . 31

2.2.2 Multivariate analysis . . . 36

2.2.3 HL-LHC sensitivity to the charm-Yukawa coupling . . . 38

2.2.4 HE-LHC and 100 TeV sensitivity to the charm-Yukawa coupling . . . 40

3.0 Off-shell Higgs Couplings in $H^* \to ZZ \to \ell\ell\nu\nu$ . . . 42

3.1 Higgs Boson Width Determination . . . 43

3.2 Effective Field Theory . . . 48

3.3 Higgs-Top Form Factor . . . 52

4.0 Directly Probing the Higgs-top Coupling at High Scales . . . 56

4.1 New Physics parametrization . . . 58

4.1.1 Effective Field Theory 58
4.1.2 Higgs-Top coupling form-factor 60
4.2 Analysis 62
4.2.1 Scale for the EFT operators 65
4.2.2 Probing the form-factor 67
5.0 Using Vector Boson Fusion for High-Scale New Physics 71
5.1 New Physics Parameterization in VBF 73
5.1.1 Higher-Dimensional Operators 73
5.1.2 Form Factors 75
5.2 VBF Kinematics 76
5.3 Event Simulation 77
5.3.1 Pre-Selection and Validation 78
5.3.2 Event Selection 79
5.4 Results 81
6.0 Conclusions 86
Appendix A. Statistical Methods 90
A.1 Gaussian Statistics 90
A.2 Binned Log-likelihood 91
Appendix B. Parton Level Analysis of VBF+γ with $h \to b\bar{b}$ 93
Appendix C. Generator-Level Cuts in VBF kinematics 99
Appendix D. Contribution from $\mathcal{O}_{\phi W}$ to VBF channel 101
Bibliography 103

List of Tables

1 Bosonic contents of Standard Model 2

2 Fermionic contents of Standard Model 3

3 Quantum numbers of fermions fields of one generation in the SM. 7

4 The production cross section for a 125 GeV SM Higgs boson in pp collisions [1]. . 17

5 The branching ratios for a 125 GeV SM Higgs boson. 22

6 Summary of existing search results at the LHC (upper two rows) and the HL-LHC projection (lower two rows). The CMS entry marked with * is scaled from the reported μ value to higher luminosity. The entries marked with † were computed from the reported μ values (see Sec. 2.2.3.) The entry marked with †† is scaled according to the description in the text following [2]. 27

7 Cross sections of signal and background at different center-of-mass energies, with the basic acceptance cuts in Sec. 2.1.1. 30

8 Expected yields of signal and multi-jet background at the HL-LHC with 3 ab^{-1} from a cut-based analysis. 36

9 Expected yields of signal and multi-jet background at the HL-LHC with 3 ab^{-1} from a BDT analysis. 40

10 The expected 95% CL_s upper limit on the signal strength and the charm-Yukawa coupling from this analysis using 3 ab^{-1} of data at 13 TeV, respectively, in comparison with other searches as quoted. 40

11 Expected sensitivity by scaling the collider c.m. energy $\sqrt{s}$. 41

12 Comparison of the sensitivity reaches between $H^* \to ZZ \to \ell\ell\nu\nu$ in this study and $H^* \to ZZ \to 4\ell$ in the literature as quoted. All results are presented at 95% CL except for the Higgs width projection derived by ATLAS with 68% CL [3]. We assume that the Wilson coefficient for the EFT framework is given by $c_t = v^2/\Lambda_{EFT}^2$. Besides the $H \to 4\ell$ channel, Ref. [4] also accounts for the $H \to \gamma\gamma$ final state with a boosted Higgs analysis. 55

13 Cut-flow for signal and backgrounds at LHC $\sqrt{s} = 14$ TeV. The selection follows the BDRS analysis described in the text. Rates are in units of fb and account for 85% (1%) b-tag (mistag) rate, hadronization, and underlying event effects. . . . 65

14 Summary results from the $t\bar{t}h$ studies for the Higgs-top coupling at high scales in terms of the dimension-6 operators and general form-factor scenarios. The results are shown at 95% CL, and we assume the HL-LHC at 14 TeV with 3 ab^{-1} of data. For comparison, we also show the results from off-shell h^* studies, the ATLAS Higgs combination with 139 fb^{-1}, and the CMS top pair bound with 35.9 fb^{-1}. . 69

15 Event yields from our simulation for `VBF` and `QCD` and expected event yields from [5], at $\sqrt{s} = 13$ TeV with an integrated luminosity of 126 fb^{-1}. 79

16 Dimension-6 results at 95% C.L. with an integrated luminosity of 3 ab^{-1}. 83

17 Expected yields of signal and multi-jet background at the HL-LHC with 3 ab^{-1} from a cut-based analysis. 98

List of Figures

1 Plots showing $V(\Phi)$ as a function of $|\Phi|$ for the cases $-\mu^2 > 0$ and $-\mu^2 < 0$. . . . 9

2 Representative Feynman diagrams of major Higgs production mechanisms at the LHC: (a) gluon fusion, (b) vector boson fusion, (c) association production with a gauge boson and (d) top quark fusion. 17

3 Production cross section of the Higgs boson at the LHC as a function of its mass [1]. 18

4 The branching ratio of the Higgs boson as a function of its mass [6]. 21

5 Representative Feynman diagrams of the signal channel (left) and QCD multi-jet background (right) 29

6 Distributions of useful observables for signal (blue) and multi-jet background (red) after pre-selections. 33

7 Distributions of useful observables for signal (blue) and multi-jet background (red) after pre-selections. 34

8 Distribution of the invariant mass of the signal c-jet pair after cuts. 35

9 The distribution of the BDT score with low, medium and high signal region defined as -0.07-0.01, 0.01-0.08 and > 0.08 respectively (top) and receiver operating characteristic (ROC) curve of the BDT (bottom). 38

10 Distribution of the invariant mass of the signal c-jet pair for events in different BDT score intervals, corresponding to the categories: low, medium and high signal. 39

11 Representative Feynman diagrams for the DY $q\bar{q} \to ZZ$ (left), GF $gg \to ZZ$ continuum (center), and s-channel Higgs signal $gg \to H^* \to ZZ$ (right). 44

12 Normalized distributions for the missing transverse momentum E_T^{miss} (left panel), azimuthal ϕ (central panel) and polar θ angles (right panel) of the charged lepton ℓ^- in the Z boson rest frame. 45

13 BDT distribution for the s-channel Higgs signal (red) and background (blue). . 47

14 95% CL bound on the Higgs width Γ_H/Γ_H^{SM} as a function of the $\sqrt{s} = 14$ TeV LHC luminosity. We display the results for the cut-based study (blue) and BDT-based analysis (red). 48

15 Feynman diagrams for the GF $gg \to ZZ$ process. The new physics effects from Eq. (3.6) display deviations on the coefficients κ_t and κ_g from the SM point $(\kappa_t, \kappa_g) = (1, 0)$. 49

16 Transverse mass distributions m_T^{ZZ} for the DY and GF $Z(\ell\ell)Z(\nu\nu)$ processes. The new physics effects are parametrized by deviations from the SM point $(\kappa_t, \kappa_g) = (1, 0)$. We follow the benchmark analysis defined in Sec 3.1. 50

17 95% CL bound on the coupling modifiers κ_t and κ_g when accounting for the off-shell Higgs measurement in the $Z(\ell\ell)Z(\nu\nu)$ channel. We assume the 14 TeV LHC with 3 ab^{-1} of data. 51

18 Transverse mass distribution m_T^{ZZ} for $gg(\to H^*) \to Z(2\ell)Z(2\nu)$ in the Standard Model (black) and with a new physics form factor (red). We assume $n = 2, 3$ and $\Lambda = 1.5$ TeV for the form factor scenario. 53

19 95% CL sensitivity on the new physics scale Λ as a function of the LHC luminosity. We assume the form factor in Eq. (3.8) with $n = 2$ (dashed line) and $n = 3$ (solid line) at the 14 TeV LHC. 54

20 Representative Feynman diagrams contributing to $t\bar{t}h$ production. The black dots represent the BSM vertices arising from the EFT operators. 59

21 Top panels: Transverse momentum distributions for the Higgs boson p_{Th} (left) and the hardest top-quark p_{Tt} (right). Bottom panels: Invariant mass distributions for the top pair m_{tt} (left) and the Higgs and top-quark m_{th} (right). Each panel shows on the top the $t\bar{t}h$ sample in the SM and new physics scenarios. The results are presented at the NLO QCD fixed order. We also show the local NLO K-factor (middle panel in each figure as NLO/LO) and the ratio between new physics and SM scenarios (bottom panel in each figure as BSM/SM). We assume the LHC at 14 TeV. 61

22 Transverse momentum distribution of the Higgs boson p_{Th} for the $t\bar{t}h$ sample in the SM (black) and new physics scenarios with $c_{tG}/\Lambda^2 = 0.1$ TeV^{-2} (red), $c_{t\phi}/\Lambda^2 = 1$ TeV^{-2} (blue). The leading backgrounds $t\bar{t}b\bar{b}$ (purple) and $t\bar{t}Z$ (green) are also presented. We assume the LHC at 14 TeV. 66

23 95% (full line) and 68% (dashed line) CL limits on the Wilson coefficients $(c_{tG}/\Lambda^2, c_{t\phi}/\Lambda^2)$ at the 14 TeV HL-LHC with 3 ab^{-1} of data. The results are presented both at the linear (black) and quadratic (red) order in dimension-6 SMEFT operator coefficients. 67

24 Transverse momentum distribution of the Higgs boson p_{Th} for the $t\bar{t}h$ sample in the SM (black) and new physics scenarios with $n = 2$ (red) and $n = 3$ (blue), assuming $\Lambda = 2$ TeV. We assume the LHC at 14 TeV. 68

25 95% CL sensitivity on the new physics scale Λ as a function of the LHC luminosity. We consider two form-factor scenarios: $n = 2$ (solid line) and $n = 3$ (dashed line). 68

26 Representative Feynman diagrams of vector boson fusion (left) and QCD background (right). 73

27 Distribution of Higgs p_T-like variables for operator $\mathcal{O}_Q^{(3)}$ (left) and for the form factor (right). 77

28 Distribution of the Higgs p_T in `QCD`, `VBF`, and `BSM`. On the left, $c_Q^{(3)}/\Lambda^2$ is set to -0.32 TeV^2, while on the right, a form factor with $n = 2$ and a scale $\Lambda = 1$ TeV is used. 81

29 Search significance as a function of cut on Higgs p_T-like variable for coefficient $c_Q^{(3)}$ (left) and for the $n = 2$ form factor (right). Variables used are described in Sec. 5.2. 82

30 Limits on Wilson coefficients of dimension-6 operators with an integrated luminosity of 3 ab^{-1}. 83

31 Search significance as a function of the scale Λ for the form factor Eq. (5.4) for $n = 2$ (blue) and for $n = 3$ (orange). An integrated luminosity of 3 ab^{-1} is used. 84

32 Limits on the scale of new physics Λ at 95% C.L. for dimension-6 operators (assuming positive coefficients) and the form factor with $n = 2$ and $n = 3$ with an integrated luminosity of 3 ab^{-1}. 85

33 Differential distributions of transverse momentum of the Higgs boson, leading and sub-leading VBF jets as well as invariant mass of the VBF jets at $\sqrt{s} = 13$ TeV. 94

34 Distributions of useful observables for signal (blue) and multi-jet background (red) after pre-selections. 95

35 Distributions of useful observables for signal (blue) and multi-jet background (red) after pre-selections. 96

36 Cross section for `BSM` sample where the coefficient of a single operator is varied. . 100

37 Differential distributions of transverse momentum of the Higgs boson, leading and sub-leading VBF jets as well as invariant mass of the VBF jets. 102

Preface

First and foremost, I would like to express my deepest gratitude to my advisor, Professor Tao Han, for his unwavering support, guidance, and encouragement throughout my PhD journey. Tao not only provided me with invaluable insight, advice, and direction at every stage of my research, but also extended his warmth and generosity by welcoming me into his home every Thanksgiving. I shall not forget the proper way to appreciate a drink for the rest of my life. His expertise, enthusiasm, and passion for science have been an inspiration and motivation for me to strive for excellence.

I also extend my sincere appreciation to the members of my committee Professor Adam Leibovich, Professor Joseph Boudreau, Professor Xiao-lun Wu and Professor Ming Chen. Their constructive feedback, insightful comments, and rigorous critique have been instrumental in shaping my research and helping me to improve my work.

I am deeply grateful to my collaborators Dorival Gonçalves, Han Qin, Roshan Mammen Abraham, Ben Carlson and Matthew Low for their support, encouragement, and contributions to my research and for making our physics discussions an absolute delight; the stimulating exchanges we shared will forever be cherished in my memory. I feel honored to have had the opportunity to work with such talented and dedicated individuals.

Speaking of guidance and support, I am thankful to all the esteemed professors who have taught me in classes: Professor Ayres Freitas, Professor Daniel Boyanovsky, Professor Brian Batell, Professor Andrew Zentner, Professor Roger Mong and Professor Colin Morningstar. Their thought-provoking classes have made my learning experience truly enjoyable. I also want to thank all the supporting staff in the Physics department for making it such a wonderful place.

I am indebted to my friends Hongbo Cai, Shuyang Cao, Lisong Chen, Yilun Guan, Andi Li, Shu Liu, Hongkai Liu, Yang Ma, Amrita Purkayastha, Han Qin, Mudit Rai, Caroline Ren, Qian Song, Si Wang, Keping Xie, Bomin Zhang, and many more who have been with me throughout this journey, offering their support and companion. They have made this journey less daunting and more enjoyable. I will cherish the memories (all the board game nights and dinner gatherings) and laughter we have shared together, and I look forward to our reunion all over the world.

My partner Pok Man Tam, who is also a physicist, deserves special recognition for his enduring love, support, and patience throughout my PhD journey. We have been together through ups and downs. He has been my pillar of strength in life and made me stronger than I was. His companion and encouragement have made this journey much more bearable and enjoyable. I eagerly look forward to unfolding the future alongside him, as we embark on a journey together, embracing new adventures, cherishing our love, and creating a lifetime of memories.

Last but not least, I want to express my heartfelt gratitude to my family. Although they do not have a slight idea of what physics is, they still support me to pursue my dream and take care of everything at home so that I have nothing to worry about. I feel lucky to be able to grow up in such an open-minded and supportive family. I am extremely grateful for their sacrifices, their unconditional love, and their belief in me.

1.0 Introduction

Throughout history, physics has made strides in understanding the fundamental elements of nature and their interactions, with the Standard Model (SM) of particle physics standing as a remarkable achievement from the 1960s, aided by modern collider technology and quantum field theory advancements. Confirming SM predictions, the discovery of the Higgs boson in 2012 at the Large Hadron Collider (LHC) by the ATLAS and CMS collaborations [7, 8] marked a significant milestone, opening avenues to explore physics Beyond the Standard Model (BSM). However, the observed Higgs boson mass of approximately 125 GeV presents a challenge, being much lower than the Planck scale of 10^{19} GeV, necessitating unnatural fine-tuning in the SM theory. To address this hierarchy problem, new BSM theories are required, and precision measurements of the Higgs properties, especially at high energy scales, hold promise for exploring new physics effects in the absence of new particles beyond the SM.

In this thesis, I examine a few proposals of probing the Higgs boson couplings at HL-LHC in the rare decay mode or high energy regime and study the phenomenological consequences of potential BSM solutions to the hierarchy problem. The goal is to offer directions for experimental searches and illuminate forthcoming explorations. This chapter serves as an introduction to the basic concepts and motivations of my study.

1.1 Overview of the Standard Model

The Standard Model (SM) of particle physics is a theoretical framework that describes the fundamental building blocks of matter and the fundamental forces that govern their interactions. It is considered one of the most successful scientific theories in history, and its development was a major milestone in our understanding of the natural world. This overview will provide a brief history of the development of the SM and introduce the particle contents and the fundamental forces described by the theory.

The SM is based on the concept of Quantum Field Theory, which describes particles as excitations of underlying fields that permeate all of space. The SM describes all known elementary particles in terms of two types: fermions and bosons. Bosons are particles that have integer spin. In the SM, there are four spin-1 bosons: gluons, photons, W and Z bosons. Gluons and photons are massless while W and Z bosons are massive. They are the force carriers of the three fundamental forces which will be introduced later. Higgs boson is the only spin-0 boson in the SM. It is responsible for generating masses for massive bosons and fermions in the SM. Fermions, on the other hand, have half-integer spin and there are twelve spin-$\frac{1}{2}$ particles in the SM. These fermions can be divided into two types: quarks and leptons. Quarks are the building blocks of protons and neutrons. They carry color charges and participate in strong interactions while leptons do not. Both quark and leptons can be grouped into three generations and each generation consists of an up-type quark, a down-type quark, a charged lepton and a neutrino. All up-type quarks carry the same amount of electric charge. This also applies to all down-type quarks and charged leptons. In general, masses of particles increase across generations. The particle contents in the SM and their basic properties are summarized in Table 1 and 2.

Name	Symbol	Spin	Charge	Mass	Force
Gluon	g	1	0	0	Strong
Photon	γ	1	0	0	Electromagnetic
W Boson	$W^{\pm}$	1	± 1	81 GeV	Weak
Z Boson	Z	1	0	91 GeV	Weak
Higgs Boson	H (or h)	0	0	125 GeV	-

Table 1: Bosonic contents of Standard Model

The SM includes three of the four fundamental forces of nature: the strong force, the weak force, and the electromagnetic force. Gravity, the fourth fundamental force, is not included in the Standard Model. The strong force is responsible for holding the nucleons of an atom together. It is mediated by particles called gluons, which interact with quarks, the building

Generation	Name	Symbol	Charge	Mass
First	up quark	u	$\frac{2}{3}$	4 MeV
	down quark	d	$-\frac{1}{3}$	7 MeV
	electron	e	-1	0.5 MeV
	electron neutrino	ν_e	0	< 0.1 eV
Second	charm quark	c	$\frac{2}{3}$	1.5 GeV
	strange quark	s	$-\frac{1}{3}$	0.2 GeV
	muon	μ	-1	0.106 GeV
	muon neutrino	ν_μ	0	< 0.1 eV
Third	top quark	t	$\frac{2}{3}$	172 GeV
	bottom quark	b	$-\frac{1}{3}$	4.7 GeV
	tau	τ	-1	1.78 GeV
	tau neutrino	ν_τ	0	< 0.1 eV

Table 2: Fermionic contents of Standard Model

blocks of protons and neutrons. The strong force was first described by Murray Gell-Mann [9] and George Zweig [10] in the early 1960s, who independently proposed the idea of quarks as the building blocks of protons, neutrons, and other hadrons. The theory of the strong force, called Quantum Chromodynamics (QCD), was developed in the 1970s, and it describes the behavior of quarks and gluons. The electromagnetic force is responsible for the interactions between charged particles and is mediated by particles called photons. The electromagnetic force is described by the theory called Quantum Electrodynamics (QED), which was started in 1920s and fully established in the late 1940s. The weak force is responsible for processes like beta-decay and is mediated by massive particles called W and Z bosons. The weak interaction is unified with the electromagnetic force, described by the electroweak theory which was first proposed in 1961 by Sheldon Glashow [11], and later completed by Steven

Weinberg [12] and Abdus Salam [13] in 1967. The mass generation of the weak bosons was a significant problem because their mass terms were not allowed by the gauge symmetry. This puzzle was solved by the Higgs mechanism which was proposed independently by Peter Higgs, François Englert, and Robert Brout [14, 15, 16] in 1964.

One of the most important aspects of the SM is the concept of gauge symmetry, which refers to the invariance of the equations describing the behavior of particles under local transformations of the gauge fields. This invariance is a fundamental principle of the SM and is essential for ensuring the consistency and predictability of the theory. Gauge symmetry is responsible for the conservation of charge and other quantum numbers, and it is a key feature of the SM. The three forces described by the SM are governed by the following gauge groups

$$SU(3)_c \times SU(2)_L \times U(1)_Y. \tag{1.1}$$

The $SU(3)_c$ group is associated with the strong force. The subscript c denotes color, which is the conserved charge of the group. For a $SU(N)$ gauge theory, there are $N^2 - 1$ generators. Therefore, the gauge bosons associated with this group are eight gluons G^i_μ. They are massless because the $SU(3)_c$ group is unbroken.

The eletromagnetic force and weak force are unified under $SU(2)_L \times U(1)_Y$ group, where subscripts L and Y denote weak isospin and hypercharge. For a $U(N)$ theory, there are N^2 generators. Thus there are four generators associated with the group, three W^i_μ and one B_μ. These gauge fields can be rotated into their mass eigenstates emerged after spontaneous symmetry breaking $SU(2)_L \times U(1)_Y \to U(1)_{\text{EM}}$. The massive eigenstates are the weak bosons: $W^\pm$ and Z^0. The electromagnetic force mediator γ is massless because the $U(1)_{\text{EM}}$ remains unbroken.

The field contents and interactions in the SM can be written in a compact form in the language of quantum field theory as follows

$$\mathcal{L}_{\text{SM}} = \mathcal{L}_{\text{gauge}} + \mathcal{L}_{\text{fermion}} + \mathcal{L}_{\text{Higgs}} + \mathcal{L}_{\text{Yukawa}}. \tag{1.2}$$

We are going to look at each term of the SM lagrangian in details in the following sections.

1.1.1 Gauge sector

The first term encodes the kinetic terms and the gauge interaction terms in the forms of field strength tensors:

$$\mathcal{L}_{\text{gauge}} = -\frac{1}{4}G^a_{\mu\nu}G^{\mu\nu a} - \frac{1}{4}W^i_{\mu\nu}W^{\mu\nu i} - \frac{1}{4}B_{\mu\nu}B^{\mu\nu}. \tag{1.3}$$

The field strength tensors are defined as follows. For $U(1)_Y$ gauge group, the field strength tensor takes the form of

$$B_{\mu\nu} = \partial_\mu B_\nu - \partial_\nu B_\mu, \tag{1.4}$$

which is the same as electromagnetism. For non-Abelian gauge theories, the field strength tensor includes a self-interacting term. In particular, for $SU(3)_C$, it is defined as

$$G^a_{\mu\nu} = \partial_\mu G^a_\nu - \partial_\nu G^a_\mu - g_s f^{abc} G^b_\mu G^c_\nu, \quad a, b, c = 1 \cdots 8, \tag{1.5}$$

where g_s is the strong coupling and f^{abc} is the antisymmetric structure constant of $SU(3)$. It is related to the generators of the $SU(3)$ group t^a as follows:

$$[t^a, t^b] = i f^{abc} t^c. \tag{1.6}$$

The generators are conventionally represented as the eight Gell-Mann matrices λ_a where $\frac{1}{2}\lambda_a = t^a$:

$$\lambda_1 = \begin{pmatrix} 0 & 1 & 0 \\ 1 & 0 & 0 \\ 0 & 0 & 0 \end{pmatrix}, \lambda_2 = \begin{pmatrix} 0 & -i & 0 \\ i & 0 & 0 \\ 0 & 0 & 0 \end{pmatrix}, \lambda_3 = \begin{pmatrix} 1 & 0 & 0 \\ 0 & -1 & 0 \\ 0 & 0 & 0 \end{pmatrix}, \lambda_4 = \begin{pmatrix} 0 & 0 & 1 \\ 0 & 0 & 0 \\ 1 & 0 & 0 \end{pmatrix},$$

$$\lambda_5 = \begin{pmatrix} 0 & 0 & -i \\ 0 & 0 & 0 \\ i & 0 & 0 \end{pmatrix}, \lambda_6 = \begin{pmatrix} 0 & 0 & 0 \\ 0 & 0 & 1 \\ 0 & 1 & 0 \end{pmatrix}, \lambda_7 = \begin{pmatrix} 0 & 0 & 0 \\ 0 & 0 & -i \\ 0 & i & 0 \end{pmatrix}, \lambda_8 = \frac{1}{\sqrt{3}}\begin{pmatrix} 1 & 0 & 0 \\ 0 & 1 & 0 \\ 0 & 0 & -2 \end{pmatrix}. \tag{1.7}$$

Similarly, for $SU(2)_L$, the field strength tensor is defined as

$$W^i_{\mu\nu} = \partial_\mu W^i_\nu - \partial_\nu W^i_\mu - g\,\epsilon^{ijk} W^j_\mu W^k_\nu, \quad i, j, k = 1 \cdots 3, \tag{1.8}$$

where g is the weak coupling and ϵ^{ijk} is the totally antisymmetric tensor such that $\epsilon^{123} = 1$. The generators of the $SU(2)$ group are denoted as τ^i, satisfying the following commutation relation:

$$[\tau^i, \tau^j] = i\epsilon^{ijk}\tau^k. \tag{1.9}$$

τ^i are represented as Pauli matrices σ^i where $\tau^i = \frac{1}{2}\sigma^i$:

$$\sigma^1 = \begin{pmatrix} 0 & 1 \\ 1 & 0 \end{pmatrix}, \sigma^2 = \begin{pmatrix} 0 & -i \\ i & 0 \end{pmatrix}, \sigma^3 = \begin{pmatrix} 1 & 0 \\ 0 & -1 \end{pmatrix}. \tag{1.10}$$

1.1.2 Fermion sector

After introducing the gauge fields in the SM, we are ready to review the gauge interactions of fermions. The Lagrangian of the fermion sector in the SM reads

$$\mathcal{L}_{\text{fermion}} = i\sum_{i=1}^{3}\left[\bar{Q^i_L}\not{D}Q^i_L + \bar{u}^i_R\not{D}u^i_R + \bar{d}^i_R\not{D}d^i_R + \bar{L^i_L}\not{D}L^i_L + \bar{e}^i_R\not{D}e^i_R\right], \tag{1.11}$$

where Q_L, L_L denote the doublets of left-handed leptons and quark, u_R, d_R, e_R denote right-handed up-type quarks, down-type quarks and charged leptons respectively. For example, for the first generation, Q_L and L_L read as

$$Q_L = \begin{pmatrix} u_L \\ d_L \end{pmatrix}, \quad L_L = \begin{pmatrix} \nu_{eL} \\ e_L \end{pmatrix} \tag{1.12}$$

The left- and right-handed chiral fermion states can be obtained by using the projection operators on an unpolarized Dirac spinor

$$\psi_R = P_R\psi, \quad \psi_L = P_L\psi, \tag{1.13}$$

where

$$P_R = \frac{1}{2}(1+\gamma^5), \quad P_L = \frac{1}{2}(1-\gamma^5). \tag{1.14}$$

The gauge interactions of fermions are encoded in the covariant derivative:

$$D_\mu = \partial_\mu - i\,g'\,B_\mu\,Y - i\,g\,\tau^i W^i_\mu - i\,g_s\,t^a G^a_\mu, \tag{1.15}$$

where g' is the hypercharge coupling and Y is the hypercharge operator while τ^i and t^a are the generators of the $SU(2)$ and $SU(3)$ groups introduced before. The covariant derivative is defined in such a way to ensure the invariance of the Lagragian under local gauge transformations:

$$\begin{aligned}
U(1)_Y: \quad & \psi_L \to e^{i\lambda_Y(x)Y}\psi_L, \qquad \psi_R \to e^{i\lambda_Y(x)Y}\psi_R \\
& B_\mu \to B_\mu + \frac{1}{g'}\partial_\mu \lambda_Y(x) \\
SU(2)_L: \quad & \psi_L \to e^{i\lambda_L^i(x)\tau^i}\psi_L, \qquad \psi_R \to \psi_R \\
& W_\mu^i \to W_\mu^i + \frac{1}{g}\partial_\mu \lambda_L^i(x) + \epsilon^{ijk} W_\mu^j \lambda_L^k(x) \\
SU(3)_c: \quad & \psi_L \to e^{i\lambda_c^a(x)t^a}\psi_L, \qquad \psi_R \to e^{i\lambda_c^a(x)t^a}\psi_R \\
& G_\mu^a \to G_\mu^a + \frac{1}{g_s}\partial_\mu \lambda_c^a(x) + f^{abc} G_\mu^b \lambda_c^c(x).
\end{aligned} \tag{1.16}$$

The transformation properties of the fermion fields are summarized in Table 3.

	Q_L	u_R	d_R	L_L	e_R
$SU(3)_c \times SU(2)_L \times U(1)_Y$ charge	$(\mathbf{3},\mathbf{2},\frac{1}{6})$	$(\mathbf{3},\mathbf{1},\frac{2}{3})$	$(\mathbf{3},\mathbf{1},-\frac{1}{3})$	$(\mathbf{1},\mathbf{2},-\frac{1}{2})$	$(\mathbf{1},\mathbf{1},-1)$

Table 3: Quantum numbers of fermions fields of one generation in the SM.

We can see that under the above local gauge transformation, mass terms of the gauge fields (such as $\sim B^\mu B_\mu$) are not gauge invariant, thus not allowed in the Lagrangian. For fermions, although the kinetic and gauge interaction terms can be separated into terms involving left-chiral fields or right-chiral fields only, this is not the case if we try to write down the mass term of fermion fields

$$-m\bar{\psi}\psi = -m\bar{\psi}_R\psi_L - m\bar{\psi}_L\psi_R. \tag{1.17}$$

The mass terms involve fermion fields of both chiralities. Since the left-chiral fields and right-chiral fields transform differently under $SU(2)_L \times U(1)_Y$, the mass terms are manifestly not gauge invariant, thus forbidden in the Lagrangian. The mass generation problem of massive gauge bosons and fermions can be solved by the Higgs mechanism which will be discussed later.

1.2 The Higgs Mechanism

1.2.1 Higgs sector

To resolve the mass generation problem of the massive gauge bosons and fermions in the SM, we need to introduce an $SU(2)_L$ doublet scalar field, which triggers the spontaneous symmetry breaking of $SU(2)_L \times U(1)_Y$ through the Higgs mechanism [14, 15, 16]. The Lagrangian of the Higgs sector in the SM is written as:

$$\mathcal{L}_{\text{Higgs}} = (D_\mu \Phi)^\dagger \, D^\mu \Phi \, - \, V(\Phi), \tag{1.18}$$

where Φ is the complex $SU(2)_L$ doublet scalar field as

$$\Phi = \begin{pmatrix} \phi^+ \\ \phi^0 \end{pmatrix} = \frac{1}{\sqrt{2}} \begin{pmatrix} \phi_1 + i\phi_2 \\ \phi_3 + i\phi_4 \end{pmatrix}. \tag{1.19}$$

$\phi_{1,2,3,4}$ are real scalar fields.

$V(\Phi)$ is the Higgs potential and given by

$$V(\Phi) = -\mu^2 \Phi^\dagger \Phi + \lambda (\Phi^\dagger \Phi)^2. \tag{1.20}$$

When both $-\mu^2$ and λ are positive, the Higgs potential has a minimum at $\sqrt{\Phi^\dagger \Phi} = 0$, the electroweak symmetry is unbroken. When $-\mu^2$ is negative and λ is positive, the Higgs potential has a minimum at $\sqrt{\Phi^\dagger \Phi} = \sqrt{\mu^2/2\lambda}$. In this case, the vacuum is not invariant under $SU(2)_L \times U(1)_Y$ symmetry, which means the gauge symmetry is spontaneously broken. These two cases are depicted in Fig. 1.

If we expand the minimum condition in terms of the four real scalar fields, it looks like

$$\Phi^\dagger \Phi = \frac{1}{2}(\phi_1^2 + \phi_2^2 + \phi_3^2 + \phi_4^2) = \frac{\mu^2}{2\lambda}. \tag{1.21}$$

Now the condition resembles a fixed-length vector in the space spanned by $\phi_{1\ldots4}$. Since it is free to rotate our basis states $\phi_{1\ldots4}$, we can choose a basis such that the vacuum expectation values of the fields are

$$\langle \phi_3 \rangle = \sqrt{\frac{\mu^2}{\lambda}}, \qquad \langle \phi_{1,2,4} \rangle = 0. \tag{1.22}$$

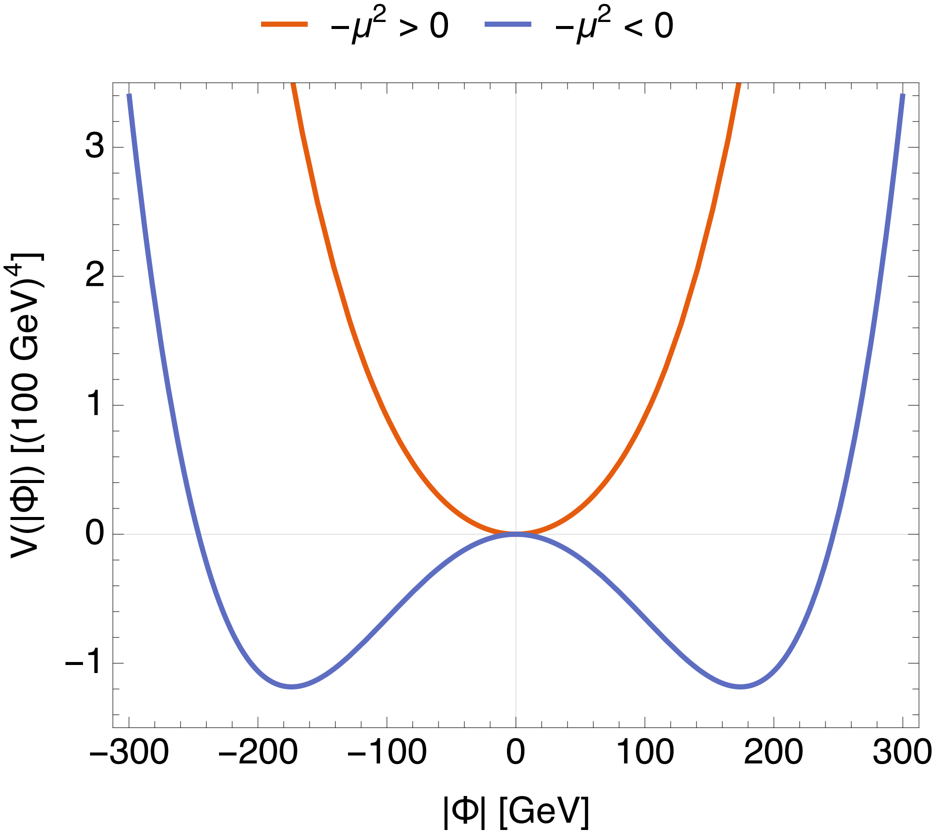

Figure 1: Plots showing $V(\Phi)$ as a function of $|\Phi|$ for the cases $-\mu^2 > 0$ and $-\mu^2 < 0$.

We can rewrite the field ϕ_3 as the vacuum expectation value (vev) v and a real scalar field h which represents the fluctuation around the vev:

$$\phi_3 = v + h, \qquad v \equiv \sqrt{\frac{\mu^2}{\lambda}}. \tag{1.23}$$

With this new definition, we expand the Higgs potential and take a look at the mass terms:

$$V \supset 0 \cdot \phi_1^2 + 0 \cdot \phi_2^2 + \lambda v^2 \cdot h^2 + 0 \cdot \phi_4^2. \tag{1.24}$$

We can see that $\phi_{1,2,4}$ correspond to three massless Goldstone boson while h corresponds to the Higgs boson with a mass

$$m_h = \sqrt{2\lambda v^2}. \tag{1.25}$$

The latest measurement of the Higgs boson mass reported by the Particle Data Group (PDG) [17] is

$$m_h = 125.25 \pm 0.17\mathrm{GeV}. \tag{1.26}$$

If we calculate the one-loop radiative corrections to the Higgs boson mass, we obtain

$$m_h^2 = m_{h,0}^2 + \frac{3\Lambda^2}{8\pi^2 v^2}(m_h^2 + 2M_W^2 + M_Z^2 - 4m_t^2), \tag{1.27}$$

where Λ is the cut-off scale of the loop integral and $m_{h,0}$ is the bare mass of the Higgs boson. The contributions from the other SM particles are not included because they are less significant. We observe that the radiative corrections have a quadratic dependence on the cut-off scale. Λ can be interpreted as the scale up to which the SM is valid. If there is no new physics below the Planck scale, meaning that $\Lambda \sim 10^{19}$, one would need a very precise cancellation between the bare mass of the Higgs boson and the radiative corrections to be consistent with the measured Higgs boson mass which is around the electroweak scale. This is known as the hierarchy problem or fine-tuning problem. This problem has been the major motivation for new physics at the TeV scale.

Many BSM models have been proposed to address the hierarchy problem. One possible solution is to introduce new particles and symmetries, such as supersymmetry. This would eliminate the quadratic divergences that plague the Higgs mass calculation, and bring the Higgs mass down to a more natural scale. However, despite decades of searches, no evidence for supersymmetry has been found yet. An alternative solution is to consider the Higgs boson as a composite bound state of more fundamental constituents, rather than an elementary particle. In this scenario, the Higgs mass arises from the strong interactions of these constituents, and is naturally much smaller than the energy scale of the theory. This is the basic idea behind composite Higgs models, which have been extensively studied in recent years. Another approach to studying the effects of BSM physics is to use effective field theory (EFT) techniques. An EFT allows us to parametrize the deviations from the SM predictions that could arise from new physics, in terms of higher-dimensional operators that respect the symmetries of the Standard Model. This approach provides a model-independent way to search for deviations from the SM, and is a key tool in interpreting the results of experiments at the LHC. These new physics models will modify the the Higgs couplings to other SM particles and lead to interesting phenomenological consequences. Chapter 3, 4 and 5 are dedicated to study the Higgs couplings at high energy in various production channels and explore the experimental signatures of different BSM scenarios.

To reveal the physics nature of the Goldstone modes, we can put them together and rewrite the Higgs doublet in such a way

$$\Phi = \frac{1}{\sqrt{2}}\exp\left(2i\,\frac{\pi^i\tau^i}{v}\right)\begin{pmatrix}0\\ v+h\end{pmatrix}, \tag{1.28}$$

where τ^i are the generators of the $SU(2)$ group defined before and π^i represents the three massless fields. Under the local gauge transformation, it transforms as

$$\begin{aligned} U(1)_Y: &\qquad \Phi \to e^{i\lambda_Y(x)Y}\Phi \\ SU(2)_L: &\qquad \Phi \to e^{i\lambda_L^i(x)\tau^i}\Phi, \end{aligned} \tag{1.29}$$

with quantum number $(\mathbf{1},\mathbf{2},\frac{1}{2})$. It does not transform under $SU(3)_c$ because it is a singlet under $SU(3)_c$. We can gauge away the Goldstone bosons by choosing $\lambda_L^i(x) = -2\pi^i/v$. This is the so-called unitary gauge. The fact that we can remove the Goldstone bosons by fixing a gauge shows that they are not physical. Now the Higgs doublet takes a simpler form with only physical degree of freedom

$$\Phi = \frac{1}{\sqrt{2}}\begin{pmatrix}0\\ v+h\end{pmatrix}, \tag{1.30}$$

and we are going to work with this from now on.

The kinetic term and gauge interactions of the Higgs field are encoded in the covariant derivative

$$D_\mu\Phi = \partial_\mu\Phi - i\,g'\,\frac{1}{2}B_\mu\Phi - i\,g\,W_\mu^i\tau^i\Phi. \tag{1.31}$$

Expanding the covariant derivative term, we will get

$$|D_\mu\Phi|^2 = \frac{1}{2}\partial_\mu h\partial^\mu h+\frac{1}{8}g^2(v+h)^2(W_\mu^1-iW_\mu^2)(W^{1\mu}+iW^{2\mu})+\frac{1}{8}(v+h)^2(-g'B_\mu+gW_\mu^3)^2. \tag{1.32}$$

The first term is the kinetic term of the Higgs boson. For the second term, the combinations of W_μ^1 and W_μ^2 correspond to the two charged W bosons:

$$W_\mu^\pm = \frac{W_\mu^1 \mp i\,W_\mu^2}{\sqrt{2}}. \tag{1.33}$$

The combination of B_μ and W^3_μ in the third term corresponds to the Z boson. By defining

$$\cos\theta_W = \frac{g}{\sqrt{g^2+g'^2}}, \qquad \sin\theta_W = \frac{g'}{\sqrt{g^2+g'^2}}, \tag{1.34}$$

where θ_W is the weak mixing angle, B_μ and W^3_μ can be rotated into their mass eigenstates:

$$\begin{pmatrix} A_\mu \\ Z_\mu \end{pmatrix} = \begin{pmatrix} \cos\theta_W & \sin\theta_W \\ -\sin\theta_W & \cos\theta_W \end{pmatrix} \begin{pmatrix} B_\mu \\ W^3_\mu \end{pmatrix} \tag{1.35}$$

Now we can rewrite the Lagrangian in terms of the mass eigenstates. Keeping only the quadratic terms, it reads

$$\mathcal{L}_{\text{Higgs}} \supset \frac{g^2v^2}{4} W^+_\mu W^{-\mu} + \frac{1}{2}\frac{(g^2+g'^2)v^2}{4} Z_\mu Z^\mu. \tag{1.36}$$

We can directly read out the masses of W bosons and Z boson from the Lagrangian

$$M_W = \frac{g\,v}{2}, \qquad M_Z = \frac{v}{2}\sqrt{g^2+g'^2}. \tag{1.37}$$

This is how the masses of massive gauge bosons are generated after spontaneous symmetry breaking. The latest measurements of the W and Z boson masses reported by the PDG [17] are

$$M_W = 80.377 \pm 0.012\,\text{GeV}, \qquad M_Z = 91.1876 \pm 0.0021\,\text{GeV}. \tag{1.38}$$

It is also noted that A_μ does not couple to the Higgs field, thus does not get a mass. This is due to the fact that $U(1)_{\text{EM}}$ remains unbroken after spontaneous symmetry breaking. Therefore, A_μ corresponds to the electromagnetic force mediator, photon.

In addition to the mass terms, the interaction terms in the Lagrangian expand as follows:

$$\mathcal{L}_{\text{Higgs}} \supset \frac{g^2v}{2} hW^+_\mu W^{-\mu} + \frac{g^2}{4} h^2 W^+_\mu W^{-\mu} + \frac{(g^2+g'^2)v}{4} hZ_\mu Z^\mu + \frac{(g^2+g'^2)}{8} h^2 Z_\mu Z^\mu. \tag{1.39}$$

From the Lagrangian, we can conveniently extract the Higgs couplings to the massive gauge bosons:

$$\begin{aligned} g_{hWW} &= (ig_{\mu\nu})\frac{g^2v}{2} = (ig_{\mu\nu})2\frac{M_W^2}{v} \\ g_{hhWW} &= (ig_{\mu\nu})\frac{g^2}{4}\cdot 2! = (ig_{\mu\nu})2\frac{M_W^2}{v^2} \\ g_{hZZ} &= (ig_{\mu\nu})\frac{(g^2+g'^2)v}{4}\cdot 2! = (ig_{\mu\nu})2\frac{M_Z^2}{v} \\ g_{hhZZ} &= (ig_{\mu\nu})\frac{(g^2+g'^2)}{8}\cdot 2!\cdot 2! = (ig_{\mu\nu})2\frac{M_Z^2}{v^2}. \end{aligned} \tag{1.40}$$

Now that we have work out the mass eigenstates of the gauge bosons, we can rewrite Eq. 1.15 in terms of the mass eigenstates:

$$\begin{aligned} D_\mu = &\partial_\mu - ig_s G^a_\mu t^a - i\frac{g}{\sqrt{2}}(W^+_\mu \tau^+ + W^-_\mu \tau^-) - iZ_\mu(g\cos\theta_W \tau^3 - g'\sin\theta_W Y) \\ &- iA_\mu(g\sin\theta_W \tau^3 + g'\cos\theta_W Y), \end{aligned} \tag{1.41}$$

where $\tau^\pm = (\tau^1 \pm i\tau^2)/\sqrt{2}$. The second term represents the strong interactions with gluons, which is unaffected. The third and fourth terms encode the weak interactions mediated by $W^\pm$ and Z bosons, which produce the charged and neutral currents when acted on fermions. Recognizing the last term as the electromagnetic interactions, we can establish the relationship between the electromagnetic coupling and weak or hypercharge coupling:

$$\begin{aligned} &- iA_\mu(g\sin\theta_W \tau^3 + g'\cos\theta_W Y) = -ieA_\mu Q \\ \Rightarrow &e = g\sin\theta_W = g'\cos\theta_W = \frac{gg'}{\sqrt{g^2 + g'^2}}, \qquad Q = \tau^3 + Y. \end{aligned} \tag{1.42}$$

1.2.2 Yukawa sector

After examining the mass generation mechanism of the massive gauge bosons, we will move our focus to the mass generation of fermions. In the SM, fermions acquire masses through Yukawa interactions. The Lagrangian of the Yukawa sector in the SM is:

$$\mathcal{L}_{\text{Yukawa}} = -y^l_{ij}\, \bar{L_L}^i \Phi e^j_R - y^d_{ij}\, \bar{Q_L}^i \Phi d^j_R - y^u_{ij}\, \bar{Q_L}^i \tilde{\Phi} u^j_R + h.c. \tag{1.43}$$

where $\tilde{\Phi}$ is the conjugate Higgs doublet given by

$$\tilde{\Phi} \equiv i\sigma^2 \Phi^* = \begin{pmatrix} \phi^{0*} \\ -\phi^- \end{pmatrix}, \tag{1.44}$$

L_L and Q_L are $SU(2)_L$ doublets of leptons and quark introduced before, i, j run from 1 to 3, representing the three generations. After spontaneous symmetry breaking, plugging in the Higgs doublet in Eq. 1.30, we will get the mass terms for the fermions. For simplicity, we first look at the lepton mass of the first generation:

$$\begin{aligned} \mathcal{L}_{\text{Yukawa}} &\supset -y_e \frac{1}{\sqrt{2}}(v + h)(\bar{e}_L e_R + \bar{e}_R e_L) \\ &= -\frac{y_e v}{\sqrt{2}}\bar{e}e - \frac{y_e}{\sqrt{2}}h\bar{e}e. \end{aligned} \tag{1.45}$$

The first term is the mass term for electron and the second term shows the coupling of electron to the Higgs boson:

$$m_e = \frac{y_e v}{\sqrt{2}}, \qquad g_{hee} = (-i)\frac{y_e}{\sqrt{2}} = -i\frac{m_e}{v}. \tag{1.46}$$

This can be generalized to the second and third generation of leptons. In general, y^l_{ij} is a 3×3 complex matrix. However, since neutrinos are massless in the SM, it is meaningless to consider couplings that mix generations. The mass generation for quarks is slightly more complicated because we need to consider mixing among generations. After the Higgs field gets a vev, the Yukawa interaction of the quarks will generate mass terms in a form of:

$$\mathcal{L}_{\text{Yukawa}} \supset -\left(\bar{u}_1\, \bar{u}_2\, \bar{u}_3\right)_R \mathcal{M}^u \begin{pmatrix} u_1 \\ u_2 \\ u_3 \end{pmatrix}_L - \left(\bar{d}_1\, \bar{d}_2\, \bar{d}_3\right)_R \mathcal{M}^d \begin{pmatrix} d_1 \\ d_2 \\ d_3 \end{pmatrix}_L + h.c., \tag{1.47}$$

where

$$\mathcal{M}^u_{ij} = \frac{v}{\sqrt{2}} y^u_{ij}, \qquad \mathcal{M}^d_{ij} = \frac{v}{\sqrt{2}} y^d_{ij}. \tag{1.48}$$

Both $\mathcal{M}^u_{ij}$ and $\mathcal{M}^d_{ij}$ are 3×3 complex matrices. To find the mass eigenstates, we need to diagonalize both matrices by bi-unitary transformations:

$$U_R^{-1}\mathcal{M}^u U_L = \begin{pmatrix} m_u & 0 & 0 \\ 0 & m_c & 0 \\ 0 & 0 & m_t \end{pmatrix}, \qquad D_R^{-1}\mathcal{M}^d D_L = \begin{pmatrix} m_d & 0 & 0 \\ 0 & m_s & 0 \\ 0 & 0 & m_b \end{pmatrix}, \tag{1.49}$$

where $U_{L,R}, D_{L,R}$ are unitary matrices defined by

$$u^i_{L,R} = U_{L,R} \begin{pmatrix} u \\ c \\ t \end{pmatrix}_{L,R}, \; d^i_{L,R} = D_{L,R} \begin{pmatrix} d \\ s \\ b \end{pmatrix}_{L,R}, \tag{1.50}$$

and u, c, t, d, s, b are the mass eigenstates of the quarks. Note that the diagonalization of the mass matrices leads to the diagonalization of the Yukawa matrices y^u_{ij} and y^d_{ij}. Thus the couplings of the Higgs boson to the quarks are also real and diagonal in the mass eigenstates and we summarize:

$$m_q = \frac{y_q v}{\sqrt{2}}, \qquad g_{hqq} = -i\frac{m_q}{v}, \tag{1.51}$$

where y_q are the eigenvalues of matrices y^u_{ij} and y^d_{ij}.

Since we rotate the up-type quarks and down-type quarks by different unitary matrices, we need to discuss the implications to electroweak interactions. For the neutral current interactions (interactions with Z boson or photon), we have bilinear forms such as

$$\mathcal{L}_{\text{N.C.}} \supset \begin{pmatrix} \bar{u}_1 \, \bar{u}_2 \, \bar{u}_3 \end{pmatrix}_L \gamma^\mu \begin{pmatrix} u_1 \\ u_2 \\ u_3 \end{pmatrix}_L = \begin{pmatrix} \bar{u} \, \bar{c} \, \bar{t} \end{pmatrix}_L U_L^\dagger \gamma^\mu U_L \begin{pmatrix} u \\ c \\ t \end{pmatrix}_L = \begin{pmatrix} \bar{u} \, \bar{c} \, \bar{t} \end{pmatrix}_L \gamma^\mu \begin{pmatrix} u \\ c \\ t \end{pmatrix}_L , \tag{1.52}$$

because $U_L^\dagger U_L = 1$. As a result, there is no mixing among generations and this is why there is no flavor changing neutral current at tree level in the SM. While neutral currents are flavor diagonal, this is not the case in the charged currents (interactions with W bosons). The charged current interactions take the form as

$$\mathcal{L}_{C.C.} \supset \begin{pmatrix} \bar{u}_1 \, \bar{u}_2 \, \bar{u}_3 \end{pmatrix}_L \gamma^\mu \begin{pmatrix} d_1 \\ d_2 \\ d_3 \end{pmatrix}_L = \begin{pmatrix} \bar{u} \, \bar{c} \, \bar{t} \end{pmatrix}_L U_L^\dagger \gamma^\mu D_L \begin{pmatrix} d \\ s \\ b \end{pmatrix}_L = \begin{pmatrix} \bar{u} \, \bar{c} \, \bar{t} \end{pmatrix}_L \gamma^\mu V \begin{pmatrix} d \\ s \\ b \end{pmatrix}_L \tag{1.53}$$

where $V = U_L^\dagger D_L$ is the Cabibbo–Kobayashi–Maskawa (CKM) matrix. U_R and D_R do not play a role here because u_R and d_R do not couple in the SM. We can show that the CKM matrix is unitary:

$$V^\dagger V = (U_L^\dagger D_L)^\dagger U_L^\dagger D_L = D_L^\dagger U_L U_L^\dagger D_L = 1. \tag{1.54}$$

The magnitudes of the CKM matrix elements obtained using a global fit [17] are given by

$$V_{CKM} = \begin{pmatrix} V_{ud} & V_{us} & V_{ub} \\ V_{cd} & V_{cs} & V_{cb} \\ V_{td} & V_{ts} & V_{tb} \end{pmatrix} = \begin{pmatrix} 0.97435 \pm 0.00016 & 0.22500 \pm 0.00067 & 0.00369 \pm 0.00011 \\ 0.22486 \pm 0.00067 & 0.97349 \pm 0.00016 & 0.04182^{+0.00085}_{-0.00074} \\ 0.00857^{+0.00020}_{-0.00018} & 0.04110^{+0.00083}_{-0.00072} & 0.999118^{+0.000031}_{-0.000036} \end{pmatrix} . \tag{1.55}$$

1.3 Experimental Status of the Higgs Boson

After reviewing the theoretical framework of the Higgs boson, it would be incomplete to not discuss its experimental status. After decades of theoretical work and experimental searches, the Higgs boson was finally observed at the Large Hadron Collider (LHC) in 2012 by the ATLAS and CMS experiments [7, 8]. The discovery of the Higgs boson is a major milestone in the history of particle physics, and it has had a profound impact on our understanding of fundamental physics. It not only confirms the existence of the Higgs field, filling in the last missing piece of the SM particle spectrum, but also opens up new avenues for research into physics beyond the SM. Since then, substantial progress has been made in understanding its properties and probing its nature through various measurements, including its mass, width and couplings to other particles, some of which will be highlighted in the following sections.

1.3.1 Production of the Higg boson

There are four major production mechanisms of the Higgs boson at the LHC, namely the gluon fusion (ggF), the vector boson fusion (VBF), the association production with a gauge boson (VH) and top quark fusion ($t\bar{t}H$). The representative Feynman diagrams of these production channels are shown in Fig. 2. Their respective production cross sections at the LHC are shown as a function of the Higgs boson mass in Fig. 3. For a 125 GeV Higgs boson, the production cross sections predicted by the SM are listed in Table 4 [1].

At LHC, the dominant production mechanism of the Higgs boson is gluon fusion, mediated by a fermionic loop. Since the couplings of fermions to Higgs boson are dictated by their masses, the main contribution to the loop is from the heaviest quark, top quark. Therefore the gluon fusion process can also be utilized to indirectly probe Higgs-top coupling, which we will study in Chapter 3. More importantly, gluon fusion can be sensitive to new heavy state propagating in the loop, thus provides a mean to test new physics. The gluon fusion process has been established with overwhelming evidences and currently the measured rate agrees with the SM prediction.

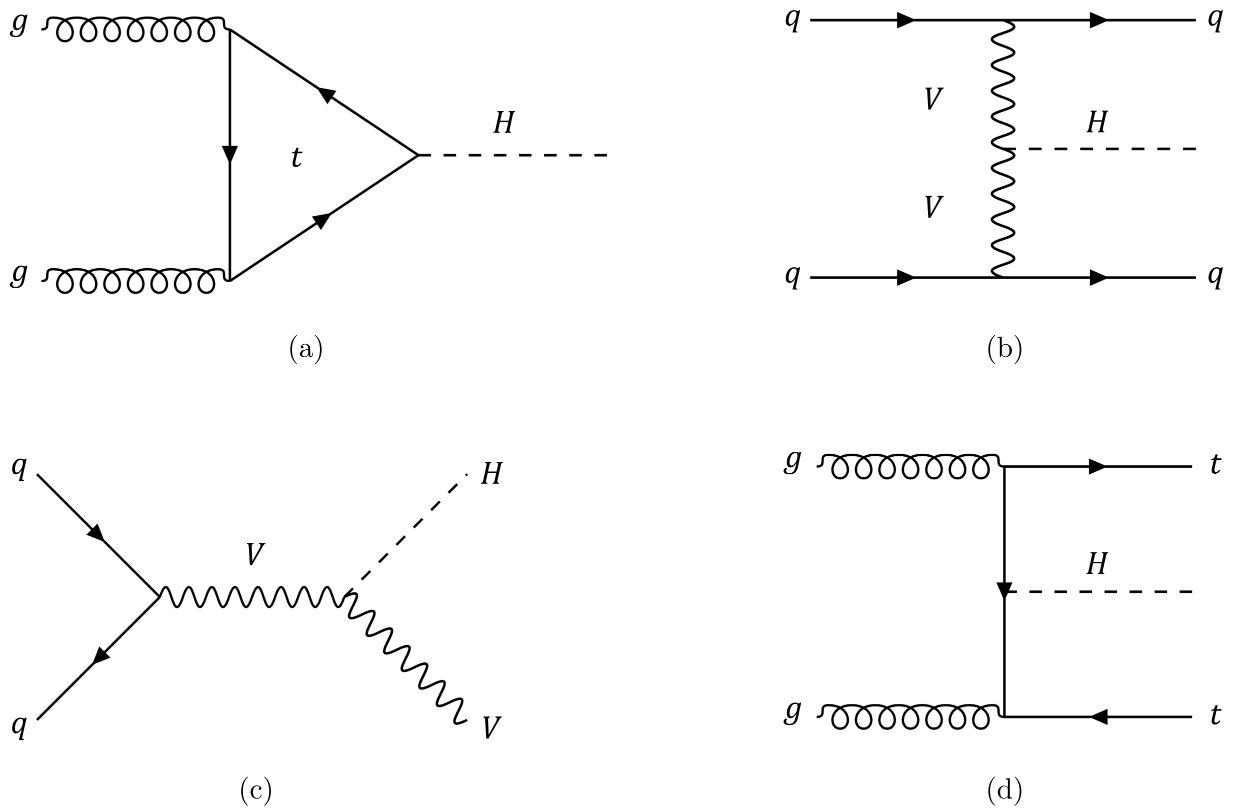

Figure 2: Representative Feynman diagrams of major Higgs production mechanisms at the LHC: (a) gluon fusion, (b) vector boson fusion, (c) association production with a gauge boson and (d) top quark fusion.

$\sqrt{s}$ (TeV)	Production cross section (pb)			
	ggF	VBF	VH	$t\bar{t}H$
13	48.57	3.925	2.256	0.4987
14	54.67	4.445	2.499	0.6037

Table 4: The production cross section for a 125 GeV SM Higgs boson in pp collisions [1].

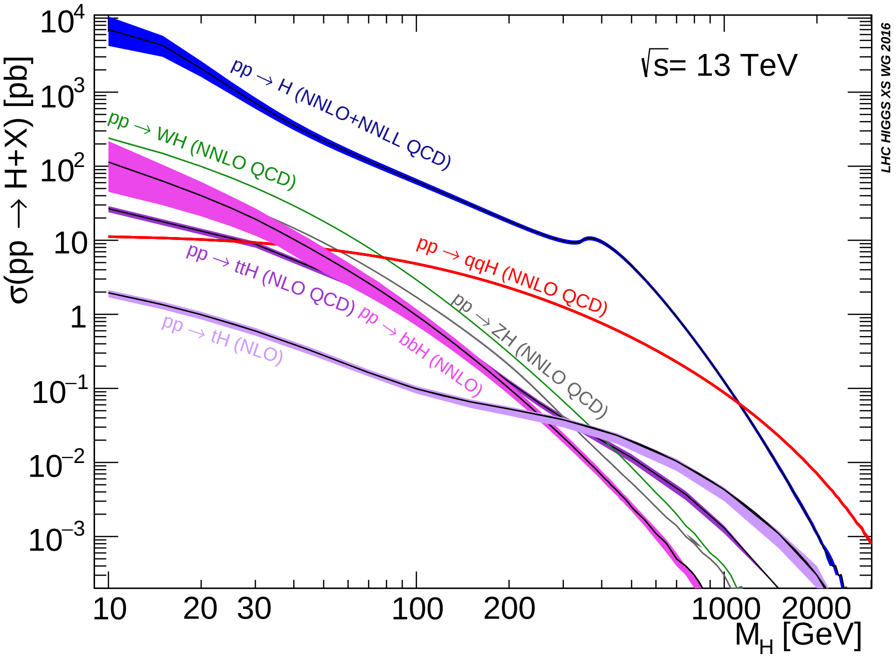

Figure 3: Production cross section of the Higgs boson at the LHC as a function of its mass [1].

The Higgs production channel with the second largest cross section at the LHC is vector boson fusion. In this process, the Higgs boson is produced by the t- or u-channel exchange of virtual W or Z bosons between two incoming quarks. As a result of the scattering, two hard jets are produced in the forward and backward regions of the detector, separated by large rapidity gap. Gluon radiation in the central region is strongly suppressed due to the color-singlet nature of the weak gauge boson exchange. These striking experimental signatures of the VBF process are useful to distinguish it from enormous QCD background and other Higgs production mechanisms. The production of Higgs bosons through VBF is an important process to study, as it provides complementary information to the more dominant Higgs production mechanism, gluon fusion. VBF can be used to measure the Higgs boson's coupling to vector bosons, which is a key prediction of the SM. ATLAS and CMS produced a combined observation of 5.4σ [18, 19], establishing this process with a rate compatible with expectation in the SM. Two interesting use cases with this channel are presented in details in Chapter 2 and 5.

The next major production mechanism is association production of Higgs boson with weak gauge boson, also called Higgsstrahlung process. This process occurs when two quarks or anti-quarks produce a Higgs boson and a weak gauge boson, mediated by an s-channel W or Z. With the weak boson decaying leptonically, this channel is relatively clean and can be useful to probe rare Higgs decay, such as $H \to c\bar{c}$. In fact, this channel provides the most stringent constraint to charm-Yukawa coupling. A complementary way to probe charm-Yukawa coupling is studied in Chapter 2. ATLAS and CMS have independently observed the VH production mode through $H \to b\bar{b}$ in an unambiguous manner, with 5.4σ and 5.6σ respectively [20, 21].

The $t\bar{t}H$ production cross section at the LHC is small, but it is still considered a major production mechanism of the Higgs boson for it provides the direct evidence of Higgs-top coupling, which will be presented in Chapter 4 in more details. The role of the Higgs-top coupling is significant in the electroweak symmetry breaking mechanism in the SM. Although the observed rates of the Higgs boson in gluon fusion provide considerable indirect evidence for top-quark Yukawa coupling, direct evidence and subsequent precise measurement at the LHC are available mainly through the ttH channel. With a large increase of $t\bar{t}H$ cross section from LHC Run 1 to Run 2 due to the upgrade of center-of-mass energy, both ATLAS and CMS were able to independently observe the Higgs production in association with a top-quark pair [22, 23]. The establishment of the $t\bar{t}H$ production channel is one of the great success of LHC Run 2 physics program and so far all production processes have been established with LHC Run 2 data.

1.3.2 Decay of the Higgs boson

The Higgs boson is not a stable particle, instead of observing it directly at the collider, its decay products are detected and used to reconstruct the Higgs boson. Therefore it is essential to understand the various decay modes of the Higgs boson. Once the Higgs boson mass is known, its decay width and decay branching ratios in to different SM particles can be well predicted by the SM. For the observed 125 GeV Higgs boson, its decay width is precisely predicted to be

$$\Gamma_H = 4.1\,\text{MeV}. \tag{1.56}$$

The partial width of the Higgs boson decays to weak bosons is

$$\Gamma(H \to VV) = \frac{G_F M_H^3}{16\pi\sqrt{2}}\delta_V\sqrt{1-4\frac{M_V^2}{M_H^2}}\left(1-4\frac{M_V^2}{M_H^2}+12\frac{M_V^4}{M_H^4}\right), \tag{1.57}$$

where $\delta_W = 2$, $\delta_Z = 1$, and the partial width of the Higgs boson decays to fermions is

$$\Gamma(H \to f\bar{f}) = \frac{N_c G_F}{4\sqrt{2}\pi}M_H\left(m_f^2\Big(1-\frac{4m_f^2}{M_H^2}\Big)^{\frac{3}{2}}\right), \tag{1.58}$$

where N_c is the number of colors of the final state fermion ($N_c = 1$ for leptons and $N_c = 3$ for quarks). Fig. 4 shows how the various decay branching ratios change as a function of the Higgs boson mass [6]. When $M_H > M_Z$, the decay mode $H \to Z\gamma$ becomes available. When $2m_b < M_H < 2M_W$, the decay mode $H \to b\bar{b}$ dominates while $M_H > 2M_W$, the decays to weak gauge bosons take over. A 125 GeV Higgs boson allows us to explore quite many different decay channels to other SM particles. The dominant Higgs boson decay modes include $H \to b\bar{b}$ and $H \to WW^*$, followed by $H \to gg$, $\tau^+\tau^-$, $c\bar{c}$ and ZZ^*. The Higgs boson can also decay into $H \to \gamma\gamma$, $Z\gamma$ and $\mu^+\mu^-$, albeit with much smaller rates. Decays into gg, $\gamma\gamma$, and $Z\gamma$ are loop-induced, which provide information on the Higgs boson couplings to WW, ZZ, and $t\bar{t}$ in different combinations. The predicted branching ratios of these decay modes in the SM are shown in Table 5 [1].

This very narrow width makes it very challenging to measure at the LHC. At the collider, only the product of cross section and branching fraction can be measured in all production modes. As a result, it is not possible to determine the total width of the Higgs boson from measurements of Higgs boson rates. Direct constraints on the Higgs boson width can be obtained from reconstructed mass line-shape. Two of the cleanest channels $H \to \gamma\gamma$ and $H \to ZZ^* \to 4l$ have been studied but only upper limit can be set due to limited mass resolution. Therefore, the constraints on the Higgs boson width that can be obtained directly from these measurements are still much larger than the expected width of the Higgs boson in the SM. Another approach to constrain the Higgs boson width is to utilize the on-shell and

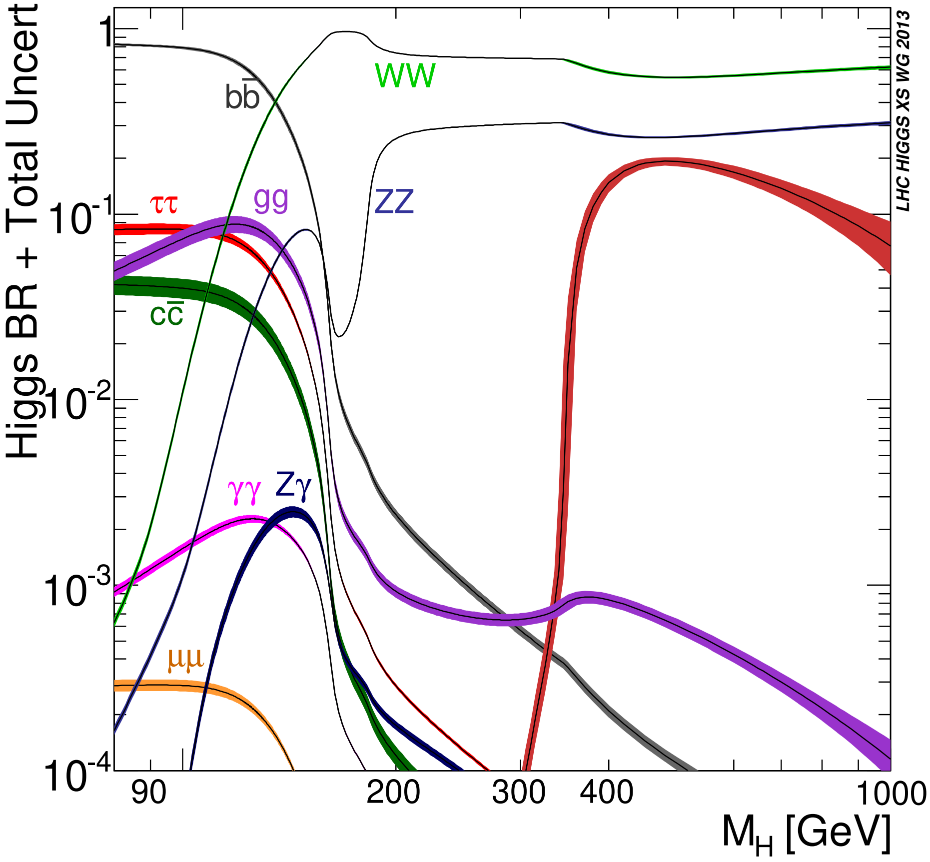

Figure 4: The branching ratio of the Higgs boson as a function of its mass [6].

Decay mode	Branching ratio
$H \to b\bar{b}$	5.824×10^{-1}
$H \to W^+W^-$	2.137×10^{-1}
$H \to gg$	8.187×10^{-2}
$H \to \tau^+\tau^-$	6.272×10^{-2}
$H \to c\bar{c}$	2.891×10^{-2}
$H \to ZZ$	2.619×10^{-2}
$H \to \gamma\gamma$	2.270×10^{-3}
$H \to Z\gamma$	1.533×10^{-3}
$H \to \mu^+\mu^-$	2.176×10^{-4}

Table 5: The branching ratios for a 125 GeV SM Higgs boson.

off-shell measurements at the same time in the $H \to VV$ channels. Assuming the running of the Higgs boson couplings is negligible in the off-shell regime,

$$\frac{\mu_{\text{off-shell}}}{\mu_{\text{on-shell}}} = \frac{\Gamma_H}{\Gamma_H^{\text{SM}}}, \tag{1.59}$$

where μ_i denotes the signal strength. The off-shell production limits from both ATLAS and CMS have been employed to limit the possible range of the Higgs boson width. At 95% C.L., they observed $\Gamma_H < 14.4$ MeV and 9.16 MeV respectively [24, 25]. More details about leveraging the off-shell measurements to constrain the Higgs boson width and the projecting bound at future High Luminosity (HL-)LHC are presented in Chapter 3.

In the SM, gauge bosons acquire masses through electroweak symmetry breaking as introduced in the last section. Therefore, establishments of decay of the Higgs boson to weak bosons are important tests of the mechanism of electroweak symmetry breaking. In fact, the earliest observed decay modes are the decay of the Higgs boson to vector bosons ($\gamma\gamma$, ZZ and WW) because the Higgs boson discovery mainly relied on its decay to bosonic final states. $H \to \gamma\gamma$ has a relatively small branching fraction of about 0.2%, but it has a very clean signature, with the two high energy photons producing a sharp peak in the invariant mass spectrum. In the SM, the decay of the Higgs boson to photons, which occurs only through loops, is dominated by the coupling of the Higgs boson to W bosons so this channel also probes the Higgs boson coupling to W bosons. Another discovery channel is $H \to ZZ^* \to 4l$, where a search is conducted to identify a narrow mass peak over a small, continuous background. The Higgs boson signal is characterized by two pairs of isolated leptons, where each pair consists of two leptons with opposite charges and the same flavor. In addition to these two primary channels, the Higgs boson has also been observed in $H \to WW^* \to l\nu l\nu$. This decay mode is more challenging due to the presence of neutrinos in the final states, which show up as missing energy in the detectors. For the same reason, instead of invariant mass, a new observable transverse mass M_T is constructed,

$$M_T = \sqrt{(E_T^{ll} + E_T^{missing})^2 + |p_T^{ll} + p_T^{missing}|^2} \tag{1.60}$$

as an effective discriminant against backgrounds. This observable is not only useful for the $H \to WW$ channel, but also in the $H \to ZZ$ channel when one of the Z decays into a pair of neutrinos, which is studied in Chapter 3.

Fermion masses are generated through the Yukawa interactions in the SM after electroweak symmetry breaking. One of the key properties of the Yukawa couplings in the SM is that it is proportional to fermion mass and thus has a non-universal pattern, in contrast to gauge couplings. Therefore, observations of the Higgs boson decays into fermions are of fundamental importance to provide direct evidences of Higgs-fermion couplings and test the predicted pattern of these couplings. The heaviest quark in the SM is top quark, thus it has the strongest coupling with the Higgs boson among fermions. However, Higgs boson decay into a pair of top quark is kinematically suppressed since top quark is heavier than the Higgs boson. This coupling can be directly probed via $t\bar{t}H$ production. The most promising channels to establish Higgs couplings to fermions are Higgs boson decays to third-generation quark and lepton $H \to b\bar{b}$ and $\tau^+\tau^-$. $H \to b\bar{b}$ is the dominant decay mode of the Higgs boson, with a branching ratio of 58% and $H \to \tau^+\tau^-$ contributes to 6% of the total decay width. Event rates are conceivable with such high branching ratios but the presence of huge backgrounds makes the isolation of a Higgs boson signal very challenging. The most sensitive production mode for the search of $H \to b\bar{b}$ is the Higgsstrahlung process which utilize the leptonic W and Z decays to trigger and improve the signal-to-background ratio. One of the key challenges in this search is to tag b-jets with high efficiency and low misidentification. With the addition of large amounts of data at Run 2 and increase in signal rates, observation of $H \to b\bar{b}$ was obtained independently by both ATLAS and CMS in the VH production mode. The observed significance of excess were 5.4σ and 5.6σ respectively [20, 21]. ATLAS and CMS have also searched for $H \to b\bar{b}$ in the VBF production mode, which is utilized to constrain new physics scales in Chapter 5. The search for $H \to \tau^+\tau^-$ has the highest sensitivity in the VBF production channel, although all production mechanisms are considered in experiments. At Run 1 of the LHC, the combined measurements of ATLAS and CMS [18, 19] observed an excess of signal of 5.5σ in $H \to \tau^+\tau^-$, but only with the larger dataset of Run 2 data, the two experiments were able to independently discover $H \to \tau^+\tau^-$ with 6.4σ and 5.9σ respectively [26, 27]. In short, the establishment of Higgs boson couplings to all third-generation fermions ($t-$, $b-$quark and τ lepton) is one of the major achievements at LHC Run 2.

Probing the Yukawa couplings to second- or even first-generation quarks is highly challenging due to the small signal rates and overwhelming backgrounds. Decay modes $H \to \mu^+\mu^-$ and $H \to c\bar{c}$ are in active search. $H \to \mu^+\mu^-$ has a very tiny branching ratio of about 0.02%, which is orders of magnitude smaller than its dominant background $Z/\gamma^* \to \mu^+\mu^-$. No excess of signal was observed at LHC Run 1. ATLAS and CMS have performed analysis with full Run 2 data and employed deep learning algorithms to distinguish signal from background. They were able to achieve significances of 2σ and 3σ respectively [28, 29], which are first evidence of the Higgs boson coupling to second-generation fermions. This decay mode is currently limited by statistics, therefore with the upgrade of LHC Run 3, it is expected to be discovered in the near future. $H \to c\bar{c}$, on the other hand, has a much larger branching ratio of about 3% but its search is even more difficult. The challenges lie in enormous multi-jet background, efficient triggering and accurate charm jet tagging. ATLAS and CMS have carried out search for $H \to c\bar{c}$ in the VH production mode and only upper limits can be set. We have proposed a new approach to search for $H \to c\bar{c}$ in Chapter 2.

2.0 Higgs to Charm Quarks in Vector Boson Fusion Plus a Photon

Since the discovery of the Higgs boson (H) by the ATLAS [7] and CMS [8] collaborations, determining its properties has become a high priority for the experiments at the LHC. Higgs boson couplings to weak gauge bosons are governed by the spontaneous symmetry breaking of the gauge theory, and have been well measured. However, the mass generation of fermions is a distinctive question. In the Standard Model (SM), fermion mass terms emerge from Higgs boson Yukawa interactions and thus the Yukawa couplings are proportional to the fermion mass. Therefore, it is crucial to establish the pattern of the Yukawa couplings to fermions in order to verify the SM and seek hints of Beyond-the-Standard-Model (BSM) physics. To date, Higgs couplings to third generation fermions have been observed to $b\bar{b}$ [30, 31], $t\bar{t}$ [32, 33] and to $\tau^+\tau^-$ [34, 35, 36]. Direct observations of the Higgs couplings to the second generation of fermions are thus of critical importance to further confirm the non-universal pattern of Yukawa couplings [37, 38]. Because of its distinctive experimental signature, the decay mode $H \to \mu^+\mu^-$ via the gg fusion production [39] and the vector-boson fusion production (VBF) [40] is promising to be observed in the near future [41, 42]. Testing the Higgs Yukawa coupling to the charm quark (y_c), on the other hand, is known to be challenging at hadron colliders due to the formidable QCD backgrounds.

At the LHC, billions of pp collisions happen every second but only a small fraction of these events will be recorded due to limitations in data storage capacity and rate limitations of the detector readout electronics. The judicious selection of events as using triggers such as isolated leptons, photons, or jets with high transverse momentum, are needed to record events of physical interest. Searching for the decay mode $H \to c\bar{c}$ with limited energy for the decay products requires incorporating the Higgs boson production mechanism to develop an efficient trigger strategy. There are currently two experimental probes of the charm-Yukawa coupling at the LHC. One approach is to use Higgs association production with a leptonically decaying Z boson (ZH channel) [43, 44]. The ZH channel provides a bound on μ of 110 for 36.1 fb^{-1} of data, where μ is defined as the ratio of the new physics cross section and the SM expectation. An extrapolation of the ATLAS analysis leads to a projection of $\mu <$

6 using 3 ab^{-1} at the HL-LHC [45]. A recent preliminary result from ATLAS improves the sensitivity to $\mu < 26$ by utilizing $139\mathrm{fb}^{-1}$ and the leptonic decays of the W boson as well as Z to invisible decays [46]. A similar result from CMS also incorporating associated production with a W boson, Z to invisible decay modes and utilizing substructure techniques yields an observed constraint of $\mu < 70$ [47]. The LHCb experiment has provided limits using 1.98 fb^{-1} of data, providing an observed constraint of $\mu < 6400$ [48], with a projection of an upper limit on the μ of 50 after collecting 300 fb^{-1} of data at 14 TeV assuming no improvements in the detector performance or analysis [49].

Another approach does not rely on tagging charm quarks from the Higgs decay, but instead uses the decay of a Higgs boson $H \to J/\psi + \gamma$ [50, 51, 2, 52, 53], a process that has been searched for by ATLAS [54, 55] and CMS [56]. This process gives a looser bound on charm-Yukawa coupling of 50 times the SM prediction even at the HL-LHC [57], due to the contamination from $H \to \gamma\gamma^*$ with a vector meson dominance in γ^*-J/ψ mixing, which is about an order of magnitude larger than that from the direct $Hc\bar{c}$ coupling [50, 2, 58].

In Table 6, we collect the current results from the LHC searches (upper two rows) and the HL-LHC projection (lower two rows). For the VH channel, the HL-LHC projections at CMS are estimated by simply scaling for the signal strength μ from the increase of the luminosity. We further translate the results to estimate the sensitivity to the modification from the SM coupling $\kappa_c = y_c^{\mathrm{BSM}}/y_c^{\mathrm{SM}}$ as described in Sec. 2.2.3. For the channel $H \to J/\psi + \gamma$, κ_c does not have a simple relation with μ due to the contamination from $H \to \gamma\gamma^*$ as noted above. It is instead estimated using Eq. (53a) in [2].

Rather than search for $H \to c\bar{c}$, it has also been proposed to constrain y_c by requiring a charm tag in the production $gc \to Hc$ with $H \to \gamma\gamma$. This channel yields a 95% CL_s limit on κ_c ranging from 2.6 to 3.9 at HL-LHC, depending on theoretical uncertainties [60]. An attempt to perform a global fit for the Higgs couplings may lead to a tighter bound on the charm-Yukawa coupling [53, 61, 62, 63], with a few model-dependent assumptions. In particular, a 95% CL_s upper bound on κ_c of 1.2 at HL-LHC is claimed in [62], obtained from the upper limit of branching ratio of Higgs boson decays to untagged BSM particles assuming $|\kappa_V| \leq 1$. Exploiting kinematic information of the Higgs boson, such as transverse momentum distribution and rapidity distribution, was proposed in probing the light-quark

Channel	$\sigma(VH) \times \mathcal{B}(H \to c\bar{c})$			$\mathcal{B}(H \to J/\psi\gamma)$
Experiment	ATLAS	CMS	LHCb	ATLAS
Data set	13 TeV 139 fb^{-1}	13 TeV 35.9 fb^{-1}	8 TeV 1.98 fb^{-1}	13 TeV 36.1 fb^{-1}
μ (95% CL$_s$)	26 [46]	70 [47]	6400 [48]	120 [55]
HL-LHC on μ	6.3 [45]	7.7*	50 (300 fb^{-1}) [59]	15 [57]
HL-LHC on κ_c	2.7†	3.1†	7 (300 fb^{-1}) [49]	50††

Table 6: Summary of existing search results at the LHC (upper two rows) and the HL-LHC projection (lower two rows). The CMS entry marked with * is scaled from the reported μ value to higher luminosity. The entries marked with † were computed from the reported μ values (see Sec. 2.2.3.) The entry marked with †† is scaled according to the description in the text following [2].

Yukawa couplings [64, 65, 66] and implemented in a combined fit by CMS [67]. The asymmetry between W^+ and W^- production has also been proposed to constrain y_c [61, 68]. It has also been proposed to constrain y_c using Di-Higgs production [69, 70]. There are proposals to further enhance the sensitivity of $H \to c\bar{c}$ by utilizing an additional photon radiation [71, 72, 73].

In this work, we propose a novel approach to probe the Yukawa coupling of charm quark via VBF for the Higgs boson production with an additional photon. This work builds off of the idea of introducing a new subset of the VBF production mode utilizing photon radiation as an additional handle [74, 75, 76, 77, 78, 79, 80] for triggering and background suppression. The new channel we propose can provide complementary information to the existing searches using the WH and ZH channels.

The rest of the chapter is organized as follows. We first lay out our search strategy in Sec. 2.1, in particular a proposal for triggering the signal events. We then present our analyses and the results in Sec. 2.2, including HL-LHC projections.

2.1 Proposed search strategy

The decay branching fraction for $H \to c\bar{c}$ is about 3%, which leads to a cross section about 0.1 pb (1 pb) from the VBF (gg) production at the 13 TeV LHC [81]. This yields a sizeable signal sample with the currently achievable luminosity. However, the process $H \to c\bar{c}$ is not only difficult to trigger, but also challenging to distinguish from large QCD multi-jet background. More sophisticated search strategies should be developed to reach the needed sensitivity for signal observation. First, the VBF channel has striking experimental signature where a central Higgs boson is accompanied by two light jets with a large rapidity gap. Second, the addition of the photon improves the trigger efficiency compared to what can be achieved using only multi-jet final states as well as suppresses the gluon-rich dominant multi-jet background. We therefore propose to search for the signal process

$$pp \to qqH\gamma \quad \text{with} \quad H \to c\bar{c}. \tag{2.1}$$

Our signal process has distinctive features, which are characterized by two c-jets from the Higgs boson decay and an energetic photon in the central region, with two light jets separated by a large rapidity gap. The dominant background is QCD multi-jet production associated with a photon, where at least two jets are tagged (or mistagged) as c-jets. Other backgrounds include $Z\gamma$+jets and VBF Higgs production+γ with $H \to b\bar{b}$, where both b-jets are mistagged as c-jets. However, their contributions are expected to be much less significant than the QCD multi-jet background, thus not included in this analysis. The representative Feynman diagrams of the signal and leading background are shown in Fig. 5 for illustration.

Our analyses are designed to isolate the signal based on their kinematic features, described in detail in Sec. 2.2. To estimate the achievable sensitivity to the signal at the hadronic collider environment, we use simulated events from Monte Carlo tools. With the very large hadronic production rate at the LHC, the trigger system is designed to record events of physical interest. For the relatively soft final states in our signal process, a dedicated trigger strategy is essential to record the signal events.

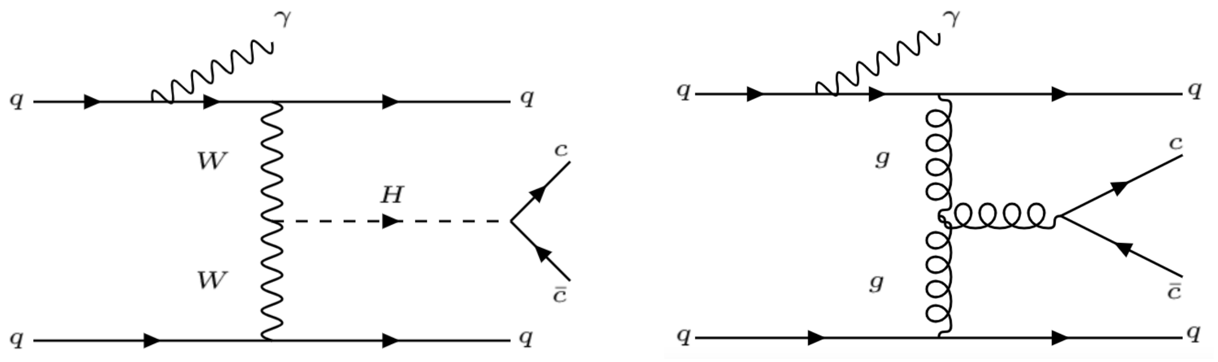

Figure 5: Representative Feynman diagrams of the signal channel (left) and QCD multi-jet background (right)

2.1.1 Monte Carlo simulation

Our targeted signal as seen in Eq. (2.1) is $H \to c\bar{c}$ plus an additional γ. Both signal and QCD multi-jet background are generated at LO with **MG5@MCNLO v2.6.5** [82] at the pp collider center of mass (c.m.) energy $\sqrt{s} = 13$ TeV using the PDF4LHC15_nlo_mc PDFs [83]. The Higgs boson in the signal process is then decayed into $c\bar{c}$ by **MadSpin** [84]. The renormalization and factorization scales are set to be at the EW scale of the W-mass (m_W). To enhance generation efficiency, both samples are generated with the following parton-level requirements, which are slightly looser than the thresholds used in analysis. We require two VBF jets inside the detector acceptance in pseudo-rapidity (η), with transverse momenta

$$p_{\rm T}^{j} > 35\,{\rm GeV}, \quad |\eta_j| < 5, \tag{2.2}$$

and an isolated photon in the central region with transverse momentum

$$p_{\rm T}^{\gamma} > 25\,{\rm GeV}, \quad |\eta_\gamma| < 3. \tag{2.3}$$

The parton shower and hadronization are simulated with **Pythia8** [85] and a fast detector simulation is implemented with **Delphes3** using the default cards [86, 87]. Jets are reconstructed using the anti-$k_{\rm t}$ algorithm [88] with a radius parameter

$$R = 0.4. \tag{2.4}$$

After these basic acceptance cuts, the cross-sections of signal and leading background processes at different center-of-mass energies are listed in Table 7 using the same calculation set-up. We see that the signal rates are sizeable with the current and anticipated luminosities. However, the signal-to-background ratios are quite low, roughly at the order of 10^{-5}, rendering the signal identification extremely challenging.

	13 TeV	14 TeV	30 TeV	100 TeV
$\sigma_{\mathrm{VBF}+\gamma}$ (pb)	0.024	0.027	0.099	0.43
$\sigma_{pp\to 4j+\gamma}$ (pb)	830	940	3700	21000

Table 7: Cross sections of signal and background at different center-of-mass energies, with the basic acceptance cuts in Sec. 2.1.1.

2.1.2 Proposed trigger strategy

The ATLAS [89] and CMS [90] experiments both contain a two-level trigger system. The first level, or level-1, trigger system is composed of custom electronics while the second level, or high-level trigger (HLT) runs software algorithms. The level-1 trigger systems of both experiments currently only utilize information from the calorimeter or muon subssystems, and as a consequence, have shared items to trigger on electrons and photons [91]. Furthermore, due to the importance of selecting electrons with $p_T \approx m_W/2$, approximately 25% of the total level-1 rate is devoted to electron/photon triggers. More information on the breakdown of rate and specific implementation can be found in the documents describing the ATLAS trigger menu [92, 93, 94, 95].

After events have been selected from the level-1 trigger using a single EM object, these events can be used to seed a variety of triggers in the HLT, including requiring additional VBF jets or jets with a b-tag to reduce the rate. Relevant to our current considerations, the ATLAS analyses described in [96, 97] utilize a trigger with the following offline requirements:

- Photon $E_{\mathrm{T}}^{\gamma} > 30$ GeV;
- At least four jets with $p_{\mathrm{T}}^{j} > 40$ GeV;

- At least one pair of jets with $m_{jj} > 700$ GeV;
- At least one b-tagged jet with 77% efficiency.

There are also VBF triggers described in [95, 98] with higher m_{jj} threshold and jet p_T threshold, which would have a lower acceptance for the genuine VBF events. To develop a trigger for $H \to c\bar{c}$ final states, it seems plausible that the trigger described above for $H \to b\bar{b}$ could be modified for charm final states, by either requiring a charm tag or by raising the m_{jj} threshold. We leave the exact details and optimization to the experiments, and proceed by providing motivation for the use case of such a trigger.

2.2 Analyses and results

2.2.1 Cut-based analysis

To obtain a physical intuition on the characteristics of our signal and background processes, we start with a simple cut-based analysis which utilize thresholds on different kinematic observables.

Pre-selections

The event pre-selections, inspired by [96, 97], aim at capturing the basic features of a VBF signal. We require a photon in the central region with

$$p_{\mathrm{T}}^{\gamma} > 30 \text{ GeV}, \quad |\eta^{\gamma}| < 1.37 \text{ or } 1.52 < |\eta^{\gamma}| < 2.37. \tag{2.5}$$

Events are required to have 4 jets with

$$p_{\mathrm{T}}^{j} > 40 \text{ GeV and } |\eta^{j}| < 4.4. \tag{2.6}$$

At least 2 jets in the central region $|\eta^{j}| < 2.5$ are required to be c-tagged using fixed efficiency values depending on the truth flavor of the jet inspired by [44]. Charm jets are assumed to have a tagging efficiency of 41%, while b-jets have a contamination probability of 25% and light jets a contamination probability of 5%. The two highest-p_{T} c-tagged jets are identified as signal jets from Higgs boson decay while the remaining jets are identified as the VBF jets.

The VBF jet pair is required to have invariant mass of at least 800 GeV so that the trigger requirement is fully efficient. In addition, the signal c-jet pair is required to have $p_{\mathrm{T}}^{cc} > 80$ GeV to remove potential bias in m_{cc} distribution caused by the p_{T}^{j} thresholds in the trigger.

Optimized analysis selections

In order to exploit the full phase space of the kinematic features, we choose several additional kinematic observables which are useful to further distinguish signal and background. The distributions of these observables after the pre-selections are shown in Figure 6 and 7. In addition to the pre-selections, we make some further judicious cuts based on the signal kinematics as follows. The invariant mass of the VBF jets (and photon) is large due to their back-to-back nature, so we require

$$m_{jj}, \quad m_{jj\gamma} > 1000\,\mathrm{GeV}. \tag{2.7}$$

The transverse momentum of the VBF jet pair is governed by the W/Z exchange and thus relatively low. We limit their value to be

$$p_{\mathrm{T}}^{jj} = |\vec{p}_{\mathrm{T}}^{j_1} + \vec{p}_{\mathrm{T}}^{j_2}| < 300\,\mathrm{GeV}. \tag{2.8}$$

Since final states from electroweak processes tend to be more back-to-back than the QCD multi-jet background, we select events with the following ratio between the magnitudes of the vector and scalar sums of the jets and photon momenta

$$p_{\mathrm{T}}^{\mathrm{balance}} = \frac{|\vec{p}_{\mathrm{T}}^{j1} + \vec{p}_{\mathrm{T}}^{j2} + \vec{p}_{\mathrm{T}}^{c1} + \vec{p}_{\mathrm{T}}^{c2} + \vec{p}_{\mathrm{T}}^{\gamma}|}{p_{\mathrm{T}}^{j1} + p_{\mathrm{T}}^{j2} + p_{\mathrm{T}}^{c1} + p_{\mathrm{T}}^{c2} + p_{\mathrm{T}}^{\gamma}} < 0.2 \tag{2.9}$$

Furthermore, because VBF signal features a large rapidity gap between the two forward-backward jets, events with large pseudo-rapidity separation between the two jets are selected for

$$\Delta\eta_{jj} = |\eta_{j_1} - \eta_{j_2}| > 4. \tag{2.10}$$

The reason that the multi-jet background also peaks at a relatively high value in Figure 6 is due to the m_{jj} requirement in the pre-selections.

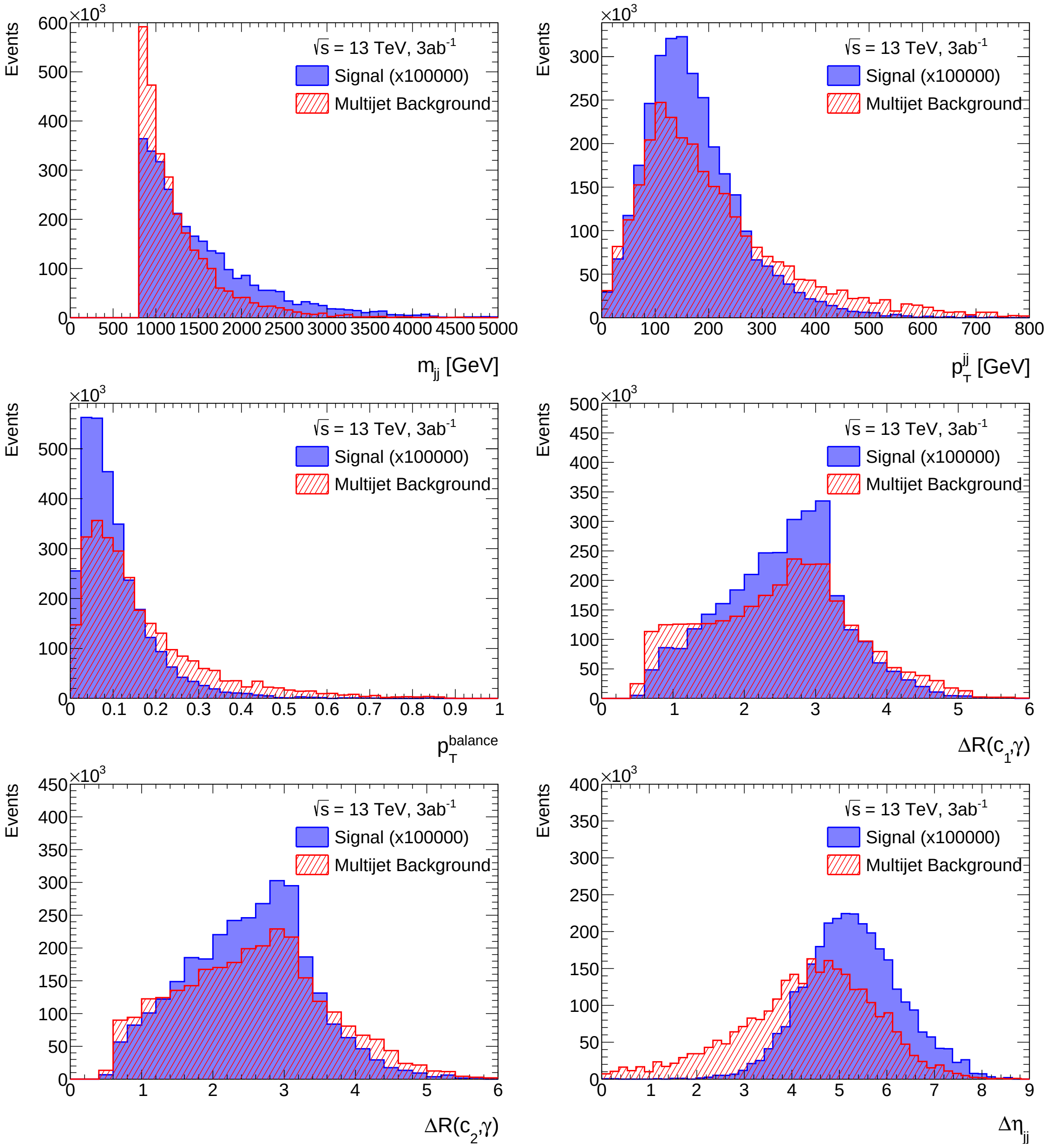

Figure 6: Distributions of useful observables for signal (blue) and multi-jet background (red) after pre-selections.

As the photon is not radiated from c-jets from Higgs decay in our signal process, the angular separation between the signal c-jets and the photon tends to be larger in contrast

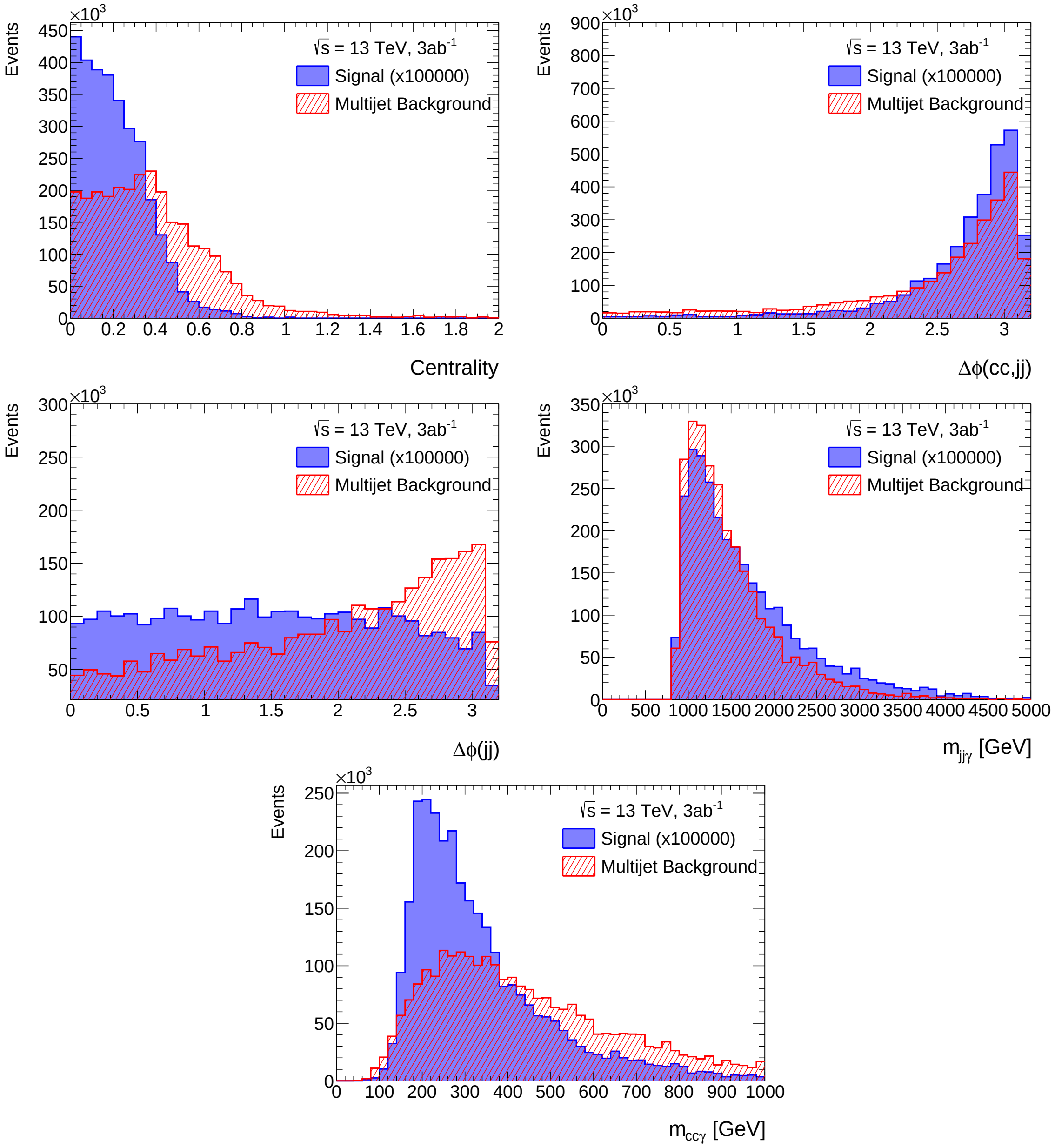

Figure 7: Distributions of useful observables for signal (blue) and multi-jet background (red) after pre-selections.

to the QCD processes. Therefore, we require

$$\Delta R(c_{1,2}, \gamma) > 1.4, \tag{2.11}$$

where $c_{1,2}$ are leading and sub-leading c-jets. We also make use of the centrality of the photon relative to the VBF jets and require

$$\text{centrality} = \left|\frac{y_\gamma - \frac{y_{j1}+y_{j2}}{2}}{y_{j1}-y_{j2}}\right| < 0.35, \tag{2.12}$$

where y is the rapidity of the jet or photon.[1] Additionally, we utilize the azimuthal angular information on the transverse plane and require

$$\Delta\phi(cc, jj) > 2.3, \quad \Delta\phi(jj) < 2.1 \tag{2.13}$$

It should be noted that the $\Delta\phi(jj)$, which is motivated by [99], has not been used to our knowledge before in the $H \to b\bar{b}$ searches. We then require the invariant mass of the c-jets and photon system

$$m_{cc\gamma} < 700\,\text{GeV}. \tag{2.14}$$

Since this observable is highly correlated with m_{cc}, we choose a relatively loose cut here.

The invariant mass of the signal c-jet pair m_{cc} is used as the final discriminant. After the above selection requirements, the distribution of m_{cc} is shown in Fig. 8. As expected, the Higgs signal peaks at $m_H \approx 125$ GeV, while the multi-jet background has a more flat

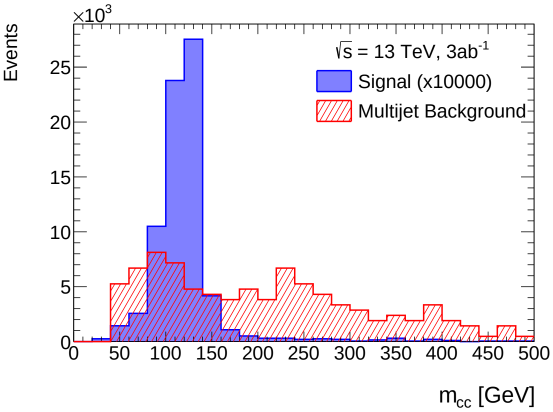

Figure 8: Distribution of the invariant mass of the signal c-jet pair after cuts.

---

[1] For a massless object, the rapidity y reduces to the pseudo-rapidity η.

shape. Anticipating finite jet-mass resolution, we therefore require the c-jet pair to be in the Higgs mass window

$$100 \text{ GeV} < m_{cc} < 140 \text{ GeV}. \tag{2.15}$$

The expected numbers of events from signal and background of integrated luminosity 3 ab^{-1} are shown in Table 8. The truth flavor components of the c-tagged jet pairs in background are also shown in Table 8. The major component is true c-jet pair as expected, but it should also be noted that the sub-leading components mainly involve light jets mistagged as c-jet. This suggests that improving the discrimination between c-jets and light jets can enhance the significance of such search.

Cut-Based		
	S	B
Pre-selections	31	2.8×10^6 (cc: 38%, cb: 5.6%, cj: 28%, bb: 4.6%, bj: 5.7%, jj: 18%)
Optimized selections	7.4	8.8×10^4
mass cut Eq. (2.15)	5.1	1.2×10^4
$S/\sqrt{B}$	0.047	

Table 8: Expected yields of signal and multi-jet background at the HL-LHC with 3 ab^{-1} from a cut-based analysis.

2.2.2 Multivariate analysis

Recent analyses of data in high energy physics have made extensive use of machine learning techniques, including the use of boosted decision trees (BDT) [100, 30, 31]. To improve the sensitivity reached by the simple cut-based studies in the last section 2.2.1, a multivariate analysis is employed, starting with only the pre-selection cuts. A BDT is trained using the **TMVA** [101] package with the same set of observables shown in Figures 6 and 7 as inputs.

The BDT is constructed by 850 trees, each with maximum depth of 3. A small depth is chosen because they are less susceptible to over-training but still perform very well with the aid of boosting algorithms. At each node of a tree, events are split into two subsets by cutting on an observable. The performance of the separation is assessed by Gini Index, defined by $p(1-p)$ where p is the ratio of signal events to all events in that node. Therefore, a pure signal or background node corresponds to a zero Gini Index. The event sample is randomly split by half into training and test samples, where the former is used for BDT training and the latter is used for analysis and deriving limits. The distribution of the BDT score from signal and background along with a receiver operator characteristic (ROC) curve are shown in Figure 9. The background rejection in the ROC curve on the right panel is defined as one minus the background survival probability after the selection cuts. The BDT performs as expected with a positive score as more "signal-like" and a negative score as more "background-like". We can see that the separation between signal and background is fairly well. The test sample distribution is superimposed with the training sample distribution, showing similar performance and thus indicates no occurrence of over-training.

To maximize the sensitivity, instead of a single cut, the BDT score is divided into three signal regions: low signal region with BDT score from -0.07 to 0.01, medium signal region with BDT score from 0.01 to 0.08, and high signal region with BDT score > 0.08, as indicated in Table 9. The invariant mass distribution of the c-jet pair is not used in the BDT training but as a final discriminator and shown in Figure 10. The invariant mass distribution m_{cc} could be included in the BDT training to improve the separation between signal and background. However, as is commonly practiced by experiments, we reserved m_{cc} as a most discriminative variable that can be used in a combined fit for signal plus background. A mass window of 100 GeV$-$140 GeV is again selected in the m_{cc} distribution. The expected numbers of events from signal and background of integrated luminosity 3 ab^{-1} are shown in Table 9 for different BDT score intervals. With the BDT cut, we can reach a signal efficiency (background rejection in the interval of BDT score) of 15% (72%), 28% (85%) and 51% (95%) in the low, medium and high signal region respectively. In comparison, the signal efficiency (background rejection) of the optimized selection cuts in Sec. 2.2.1 is 24% (97%), shown together with the BDT ROC curve on the right panel in Figure 9. For the

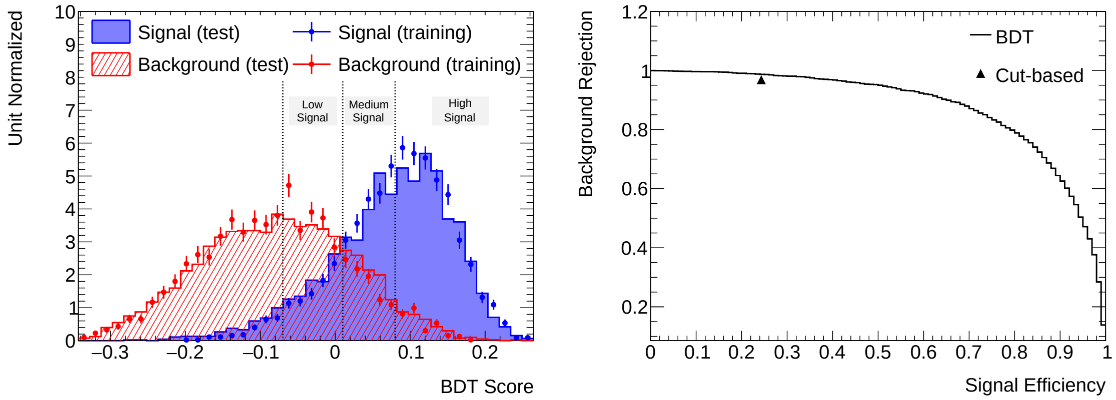

Figure 9: The distribution of the BDT score with low, medium and high signal region defined as -0.07-0.01, 0.01-0.08 and > 0.08 respectively (top) and receiver operating characteristic (ROC) curve of the BDT (bottom).

same background rejection, BDT can achieve a signal efficiency of 40%, outperforming the cut-based analysis. The overall significance is calculated by combining the significance in the three signal regions in quadrature, with the largest contribution coming from the high signal region. A relative change in significance of roughly 50% is seen, where the relative change is defined as $(\delta^{\text{BDT}} - \delta^{\text{cut-based}})/\delta^{\text{cut-based}}$, and $\delta = S/\sqrt{B}$.

Like the other extrapolations to the HL-LHC [102, 45], we have not considered the effects from the systematic errors. On the one hand, it is important to include the systematic effects to draw robust conclusions, especially given the rather small S/B for the signal searches. On the other hand, the systematic effects due to the background measurement are largely unknown for the HL-LHC. We believe that when the large data sample becomes available, the systematic errors may be controlled to a desirable level of a few percent or lower.

2.2.3 HL-LHC sensitivity to the charm-Yukawa coupling

The expected 95% CL_s upper limit on the signal strength μ in the absence of systematic uncertainties is approximated by $2\sqrt{B}/S$. The BSM modification of the charm-Yukawa

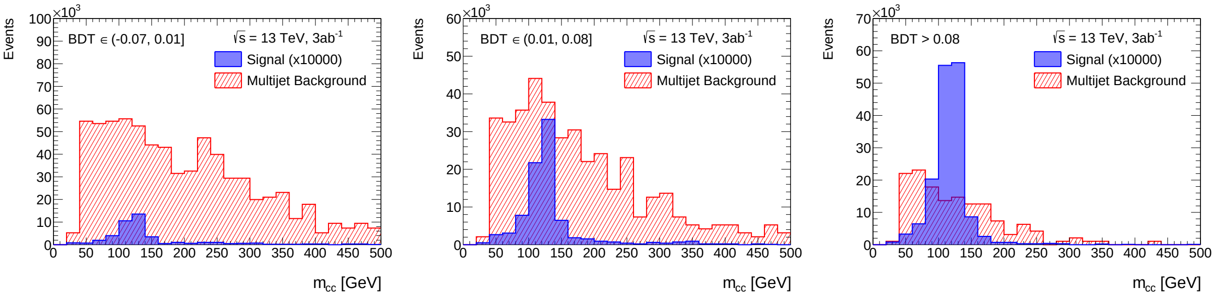

Figure 10: Distribution of the invariant mass of the signal c-jet pair for events in different BDT score intervals, corresponding to the categories: low, medium and high signal.

coupling is parametrized using the κ-scheme as

$$y_c^{\rm BSM} = \kappa_c y_c^{\rm SM}, \tag{2.16}$$

then the number of signal events would approximately scale as

$$N_{\rm sig} \simeq \frac{\kappa_c^2}{\kappa_H^2} N_{\rm sig}^{\rm SM}, \tag{2.17}$$

where κ_H denotes the BSM modification of the Higgs width. In principle, κ_H depends on all BSM modifications of SM Higgs decay channels and any new channels. If we assume that κ_c is the only non-SM modification, the upper limit on the signal strength can be translated into limit on the charm-Yukawa coupling:

$$\mu = \frac{\kappa_c^2}{1 + Br_{cc}^{\rm SM}(\kappa_c^2 - 1)}, \tag{2.18}$$

which are shown in Table 10, in comparison with some of the existing literature.

	Low signal		Medium signal		High signal	
	S	B	S	B	S	B
BDT cut	4.5	7.6×10^5	8.5	4.1×10^5	16	1.5×10^5
mass cut Eq. (2.15)	2.4	1.1×10^5	5.5	8.2×10^4	11	2.8×10^4
$S/\sqrt{B}$	0.0073		0.019		0.066	
$S/\sqrt{B}$ combined	0.070					

Table 9: Expected yields of signal and multi-jet background at the HL-LHC with 3 ab^{-1} from a BDT analysis.

2.2.4 HE-LHC and 100 TeV sensitivity to the charm-Yukawa coupling

It is natural to ask to what extend the probe to the charm-Yukawa coupling can be improved at the future higher energy hadron colliders, such as the HE-LHC [103] and the FCC-hh [104]. The answer obviously depends on the detector performance of the charm-tagging, photon detection, and the QCD jet rejection, we nevertheless perform a crude estimate the sensitivity reach by assuming the same detector performance as the HL-LHC study. The sensitivity is estimated by extrapolating the HL-LHC performance as shown in the previous sections. We again calculate the signal cross section and the leading QCD

	Cut-based	BDT	ZH [45]	Fit [62]	Hc [60]	$H \to c\bar{c}\gamma$ [72]
μ	43	29	6.3	–	–	75
κ_c	–	13	2.7	1.2	2.6 - 3.9	8.8

Table 10: The expected 95% CL_s upper limit on the signal strength and the charm-Yukawa coupling from this analysis using 3 ab^{-1} of data at 13 TeV, respectively, in comparison with other searches as quoted.

background for $\sqrt{s}$ values of 30 TeV and 100 TeV. By scaling the expected number of signal and background events for $\sqrt{s} = 13$ TeV to higher energies, we extrapolate the sensitivities, assuming the same luminosity of 3 ab^{-1} as shown in Table 11.

$\sqrt{s}$	13 TeV	30 TeV	100 TeV
$S/\sqrt{B}$ (3 ab^{-1})	0.07	0.14	0.25
κ_c reach	13	5	3

Table 11: Expected sensitivity by scaling the collider c.m. energy $\sqrt{s}$.

We have assumed that the cross section increase from $\sqrt{s} = 13$ TeV to higher energy values does not change as a function of kinematic variables that are used as input to the BDT. Since both signal and background cross sections increase approximately linearly with center-of-mass energy, we see that the sensitivity scales roughly as the square root of center-of-mass energy for the same integrated luminosity, reaching $S/\sqrt{B}$ of 0.25 and $\kappa_c \sim 3$.

3.0 Off-shell Higgs Couplings in $H^* \to ZZ \to \ell\ell\nu\nu$

Following the discovery of the Higgs boson at the Large Hadron Collider (LHC) [14, 105, 106, 107, 108], understanding the properties of this unique particle has become a primary focus in the search for new physics beyond the Standard Model (BSM). The Higgs boson's mysteries encompass various puzzles, such as the mass hierarchy between the unprotected electroweak (EW) scale (v) and the Planck scale (M_{PL}), neutrino mass generation, potential connections to dark matter, and the nature of the electroweak phase transition in the early universe. Precision examinations of the Higgs boson's properties hold the potential to reveal new physics effects at higher scales. Specifically, new physics at a scale Λ could result in effects of the order v^2/Λ^2.

Up to this point, measurements at the LHC based on the Higgs signal strength have been consistent with Standard Model (SM) predictions. However, these measurements have primarily focused on on-shell Higgs boson production, exploring Higgs properties at low energy scales around v. It has been suggested that studying the Higgs physics at a higher scale Q could enhance sensitivity as Q^2/Λ^2. A particularly interesting approach is investigating the Higgs sector across different energy scales using the sizable off-shell Higgs boson rates at the LHC [109, 110, 111, 112, 113]. While off-shell Higgs new physics sensitivity is typically derived at the LHC through the $H^* \to ZZ \to 4\ell$ channel [114, 115, 116, 117, 118, 119, 120, 121], we demonstrate in this study that extending the analysis to the $ZZ \to \ell\ell\nu\nu$ channel can significantly contribute to potential discoveries. Despite the presence of two missing neutrinos in the final state, this channel offers two key advantages for probing the high-energy regime with sufficient statistics. Firstly, it exhibits a six-fold higher event rate compared to the four charged lepton channel. Secondly, the transverse mass for the ZZ system provides a precise phenomenological probe to the underlying physics, setting the physical scale Q^2.

In this chapter, we expand on previous studies by conducting comprehensive analyses for an off-shell channel in Higgs decay

$$pp \to H^* \to ZZ \to \ell^+\ell^- \ \nu\bar{\nu}, \tag{3.1}$$

where $\ell = e, \mu$ and $\nu = \nu_e, \nu_\mu, \nu_\tau$. Our focus lies on the leading production channel of the Higgs boson via gluon fusion, benefiting from the clean decay modes. Initially, we explore a theoretical scenario incorporating additional unobserved Higgs decay channels, leading to an increased Higgs boson width ($\Gamma_H/\Gamma_H^{SM} > 1$). The distinctive dependence of the on-shell and off-shell cross-sections on the Higgs boson width enables precise measurements of this crucial aspect of the Higgs sector. To enhance signal sensitivity, we employ Machine-learning techniques in the form of Boosted Decision Trees (BDT). This analysis serves as a foundation for subsequent investigations. Next, we delve into the effective field theory framework, capitalizing on the characteristic energy-dependence of certain operators. Additionally, we address a more general hypothesis featuring a non-local momentum-dependent Higgs-top interaction [121], represented by a form factor, which generically represents the composite substructure. Overall, our goal in this chapter is to underscore the complementarity across various frameworks [117, 116, 122, 118, 119, 120, 121], utilizing the promising process at the LHC $H^* \to Z(\ell\ell)Z(\nu\nu)$. This encompasses models predicting invisible Higgs decays, the effective field theory approach, and the non-local form-factor scenario. Our results demonstrate significant sensitivities at the High-Luminosity LHC (HL-LHC) to the new physics scenarios considered here, surpassing existing literature.

The remaining part of this chapter is structured as follows. In Sec. 3.1, we calculate the Higgs width limit at HL-LHC. Subsequently, in Sec. 3.2, we investigate the sensitivity to new physics within the effective field theory framework. Then, in Sec. 3.3, we analyze the effects of a non-local Higgs-top form-factor. Finally, we present a summary table in Table.12 for comparing our reach of new physics scale with other channels and existing literature. We conclude our study in Chapter 6.

3.1 Higgs Boson Width Determination

The combination of on-shell and off-shell Higgs boson rates addresses a significant limitation of the LHC, specifically the Higgs boson width measurement [109, 110]. This method

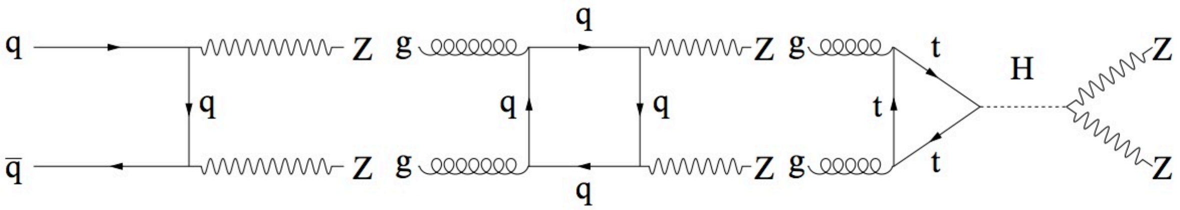

Figure 11: Representative Feynman diagrams for the DY $q\bar{q} \to ZZ$ (left), GF $gg \to ZZ$ continuum (center), and s-channel Higgs signal $gg \to H^* \to ZZ$ (right).

overcomes the degeneracy present in on-shell Higgs coupling studies

$$\sigma^{\text{on-shell}}_{i\to H\to f} \propto \frac{g_i^2(m_H)g_f^2(m_H)}{\Gamma_H}\,, \tag{3.2}$$

where the total on-shell rate can be held constant under the transformation $g_{i,f}(m_H) \to \xi g_{i,f}(m_H)$ with $\Gamma_H \to \xi^4\Gamma_H$. However, the off-shell Higgs rate, due to its sub-leading dependence on the Higgs boson width Γ_H

$$\sigma^{\text{off-shell}}_{i\to H^*\to f} \propto g_i^2(\sqrt{\hat{s}})g_f^2(\sqrt{\hat{s}})\,, \tag{3.3}$$

breaks this degeneracy. Here, $\sqrt{\hat{s}}$ represents the partonic center-of-mass energy characterizing the scale of the off-shell Higgs. Notably, if new physics effects result in the same coupling modifiers in both kinematical regimes [117, 116, 118, 119], the relative measurement of the on-shell and off-shell signal strengths can unveil the Higgs boson width, given by $\mu_{\text{off-shell}}/\mu_{\text{on-shell}} = \Gamma_H/\Gamma_H^{SM}$.

In this section, we present a projection for measuring the Higgs boson width at the high-luminosity LHC with a center-of-mass energy of $\sqrt{s} = 14$ TeV, focusing on the $ZZ \to 2\ell 2\nu$ final state. The signal channel is defined as in Eq. (3.1), where two same-flavor opposite sign leptons ($\ell = e$ or μ) reconstruct a Z boson and recoil against a large missing transverse momentum from $Z \to \nu\bar{\nu}$. The main backgrounds for this search include the Drell-Yan (DY) processes $q\bar{q} \to ZZ, ZW$ and the gluon fusion (GF) process $gg \to ZZ$, as shown in Fig. 11. While the Drell-Yan component exhibits the largest rate, the gluon fusion box diagrams

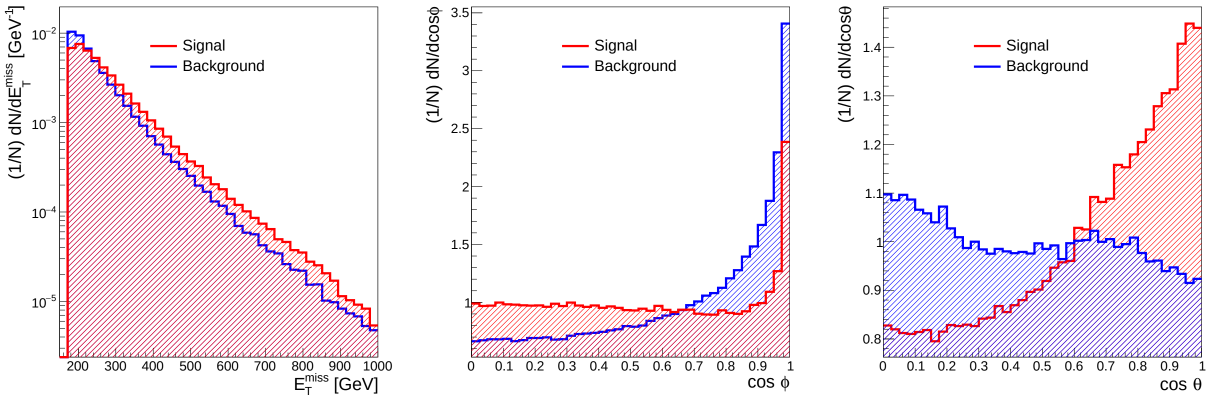

Figure 12: Normalized distributions for the missing transverse momentum $E_T^{\rm miss}$ (left panel), azimuthal ϕ (central panel) and polar θ angles (right panel) of the charged lepton ℓ^- in the Z boson rest frame.

interfere with the Higgs signal, contributing significantly, particularly at the off-shell Higgs regime [109].

In our calculations, we generate the signal and background samples using MadGraph5 aMC@NLO [82, 123]. For the Drell-Yan background, we employ the NLO MC@NLO algorithm [124]. To account for higher-order QCD effects in the loop-induced gluon fusion component, we include a universal K-factor [111, 125]. Spin correlation effects for the decays of the Z and W bosons are incorporated using the MadSpin package [84]. The renormalization and factorization scales are set based on the invariant mass of the gauge boson pair, $Q = m_{VV}/2$, using the PDF set nn23nlo [126]. To account for hadronization and underlying event effects, we utilize Pythia8 [85], while detector effects are considered with the Delphes3 package [86].

We initiate our analysis by applying some basic lepton selections. Specifically, we require two same-flavor and opposite-sign leptons satisfying $|\eta_\ell| < 2.5$ and $p_{T\ell} > 10$ GeV, within the invariant mass window of 76 GeV $< m_{\ell\ell} <$ 106 GeV. To suppress SM backgrounds, we impose a large missing energy selection of $E_T^{\rm miss} > 175$ GeV and a minimum transverse mass for the ZZ system, with $m_T^{ZZ} > 250$ GeV, defined as

$$m_T^{ZZ} = \sqrt{\left(\sqrt{m_Z^2 + p_{T(\ell\ell)}^2} + \sqrt{m_Z^2 + (E_T^{\text{miss}})^2}\right)^2 - \left|\vec{p}_{TZ} + \vec{E}_T^{\text{miss}}\right|^2} . \tag{3.4}$$

We verify the consistency of our event simulation and analysis setup by conducting a cross-check with the ATLAS study presented in Ref. [112].

To further control the large Drell-Yan background, we implement a Boosted Decision Tree (BDT) using the Toolkit for Multivariate Data Analysis with ROOT (TMVA) [127]. The BDT is trained to distinguish between the full background events and the s-channel Higgs production. The variables utilized in the BDT include the missing transverse energy, the momenta and rapidity for the leading and sub-leading leptons ($p_T^{\ell 1}, \eta^{\ell 1}, p_T^{\ell 2}, \eta^{\ell 2}$), the leading jet ($p_T^{j1}, \eta^{j1}$), the separation between the two charged leptons $\Delta R_{\ell\ell}$, the azimuthal angle difference between the di-lepton system and the missing transverse energy $\Delta\phi(\vec{p}_T^{\,\ell\ell}, \vec{E}_T^{\text{miss}})$, and the scalar sum of jets and lepton transverse momenta H_T. Additionally, we include the polar θ and azimuthal ϕ angles of the charged lepton ℓ^- in the Z rest frame [128, 129]. For the Z rest frame's coordinate system, we adopt the Collins-Soper frame [130]. In Fig. 12, we illustrate the signal and background distributions for these observables. Significant differences between the s-channel signal and background can be observed in the (θ, ϕ) angle distributions. These kinematic features arise from the different Z boson polarizations for the signal and background components at the large di-boson invariant mass m_T^{ZZ} [118, 131]. While the s-channel Higgs tends to have Z_L dominance, the DY background is mostly Z_T dominated.

We present the effectiveness of the implemented BDT analysis in separating the s-channel Higgs from the background contributions in Fig. 13. The BDT discriminator is defined in the range $[-1, 1]$, where events with a discriminant close to -1 are classified as background-like, and those close to 1 are signal-like. The optimal BDT score selection has been determined using TMVA. To assess the BDT treatment's effectiveness, we find that at an integrated luminosity of 273 fb^{-1}, one can achieve $S/\sqrt{S+B} = 5$ with a signal efficiency of 88% and a background rejection of 34%, by setting the requirement $\text{BDT}_{\text{response}} > -0.26$. With the dominant backgrounds $q\bar{q} \to ZZ, ZW$ effectively controlled, we proceed with the new physics sensitivity study.

To maximize the sensitivity of the Higgs width measurement, we focus on the most

Figure 13: BDT distribution for the s-channel Higgs signal (red) and background (blue).

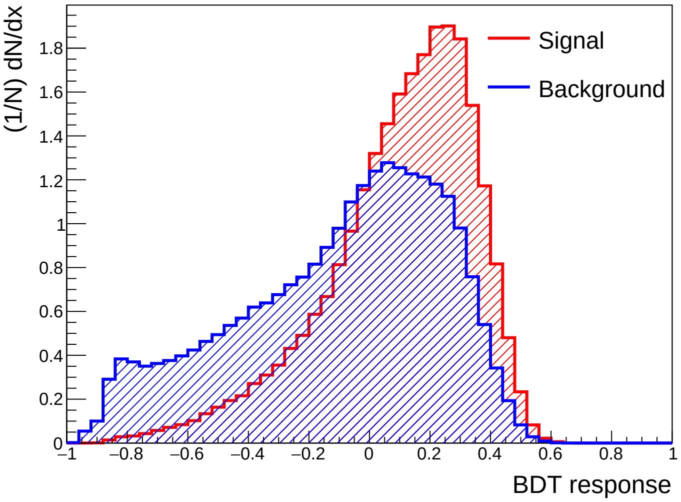

sensitive variable, the m_T^{ZZ} distribution, and perform a binned log-likelihood ratio analysis. Fig. 14 displays the 95% confidence level (CL) on the Higgs width Γ_H/Γ_H^{SM} as a function of the $\sqrt{s} = 14$ TeV LHC luminosity. To assess the relevance of the multivariate analysis, which specifically explores the observables $(E_T^{\text{miss}}, \theta, \phi)$ depicted in Fig. 12, we present the results in two analysis scenarios: the cut-based analysis in blue and the results accounting for the BDT-based framework in red. The significant sensitivity enhancement due to the BDT demonstrates the importance of considering the full kinematic dependence, including the Z-boson spin correlation effects. The Higgs width can be constrained to $\Gamma_H/\Gamma_H^{SM} < 1.35$ at the 95% CL level following the cut-based analysis, while the BDT-based study achieves $\Gamma_H/\Gamma_H^{SM} < 1.31$ assuming $\mathcal{L} = 3$ ab^{-1} of data. Consequently, the BDT limits improve the final Higgs width sensitivity by approximately 5%. These results are competitive with the HL-LHC estimates for the four charged lepton final state derived by ATLAS and CMS, where the respective limits are $\Gamma_H/\Gamma_H^{SM} < \mathcal{O}(1.3)$ and $\mathcal{O}(1.5)$ at the 68% CL [3, 4].

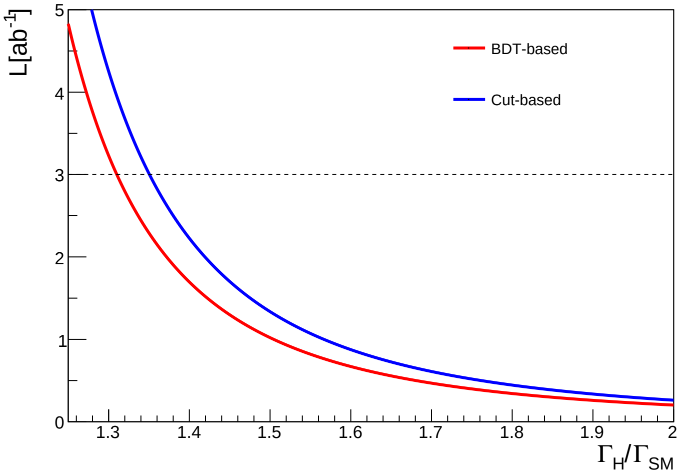

Figure 14: 95% CL bound on the Higgs width Γ_H/Γ_H^{SM} as a function of the $\sqrt{s} = 14$ TeV LHC luminosity. We display the results for the cut-based study (blue) and BDT-based analysis (red).

3.2 Effective Field Theory

The Effective Field Theory (EFT) offers a coherent framework to describe beyond the Standard Model (SM) effects when there is a mass gap between the SM and new physics states. In this context, the new physics states can be integrated out, and their effects can be parametrized in terms of higher dimension operators [132]. In this section, we adopt the EFT framework [133, 134] to parametrize the new physics effects. Instead of conducting a global coupling fit, we focus on a relevant subset of higher dimension operators that influence Higgs production through gluon fusion. This allows us to explore the new physics sensitivity specifically for the off-shell $pp \to H^* \to Z(\ell\ell)Z(\nu\nu)$ channel. Our effective Lagrangian can be written as

$$\mathscr{L} \supset c_g \frac{\alpha_s}{12\pi v^2} |\mathcal{H}|^2 G_{\mu\nu}G^{\mu\nu} + c_t \frac{y_t}{v^2} |\mathcal{H}|^2 \bar{Q}_L \tilde{\mathcal{H}} t_R + \text{h.c.} \ , \tag{3.5}$$

where $\mathcal{H}$ is the SM Higgs doublet and $v = 246$ GeV is the vacuum expectation value of the SM Higgs field. The couplings are normalized in a way that facilitates future convenience. To

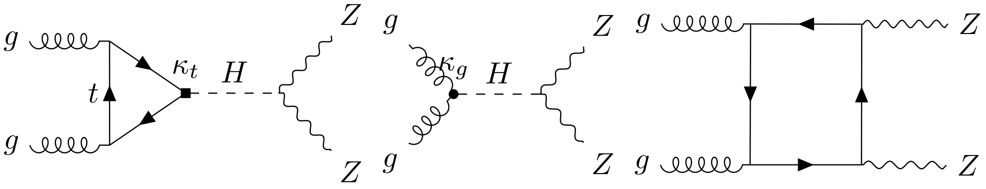

Figure 15: Feynman diagrams for the GF $gg \to ZZ$ process. The new physics effects from Eq. (3.6) display deviations on the coefficients κ_t and κ_g from the SM point $(\kappa_t, \kappa_g) = (1, 0)$.

establish a connection with the new physics scale Λ, the scaling of the couplings is as follows: c_g and c_t are proportional to v^2/Λ^2, where v represents the electroweak symmetry breaking scale. After electroweak symmetry breaking, Eq. (3.5) yields the following interaction terms involving a single Higgs boson

$$\mathscr{L} \supset \kappa_g \frac{\alpha_s}{12\pi v} H G_{\mu\nu} G^{\mu\nu} - \kappa_t \frac{m_t}{v} H \left(\bar{t}_R t_L + \text{h.c.} \right) \ , \tag{3.6}$$

where the coupling modifiers $\kappa_{g,t}$ and the Wilson coefficients $c_{g,t}$ are related by $\kappa_g = c_g$ and $\kappa_t = 1 - \mathrm{Re}(c_t)$. In Fig. 15, we present the Feynman diagrams for $gg \to ZZ$ that incorporate the effects of the new physics couplings mentioned earlier.

While Eq. (3.5) represents only a subset of high-dimensional operators affecting Higgs interactions [133, 134], we focus on it to highlight the effectiveness of off-shell Higgs measurements in resolving a well-known degeneracy involving these terms. The gluon fusion Higgs production at the low-energy regime can be well approximated by the Higgs Low Energy Theorem [135, 136], where the total Higgs production cross-section scales as $\sigma_{\text{GF}} \propto |\kappa_t + \kappa_g|^2$. Consequently, low-energy measurements, such as on-shell and non-boosted Higgs production [137, 138, 139, 140, 141, 116, 142, 118, 143], are incapable of resolving the $|\kappa_t + \kappa_g| = \text{constant}$ degeneracy. Although the combination of $t\bar{t}H$ and gluon fusion Higgs production has the potential to break this degeneracy [144], we will demonstrate that Higgs production in the off-shell regime can also make significant contributions in resolving this degeneracy.

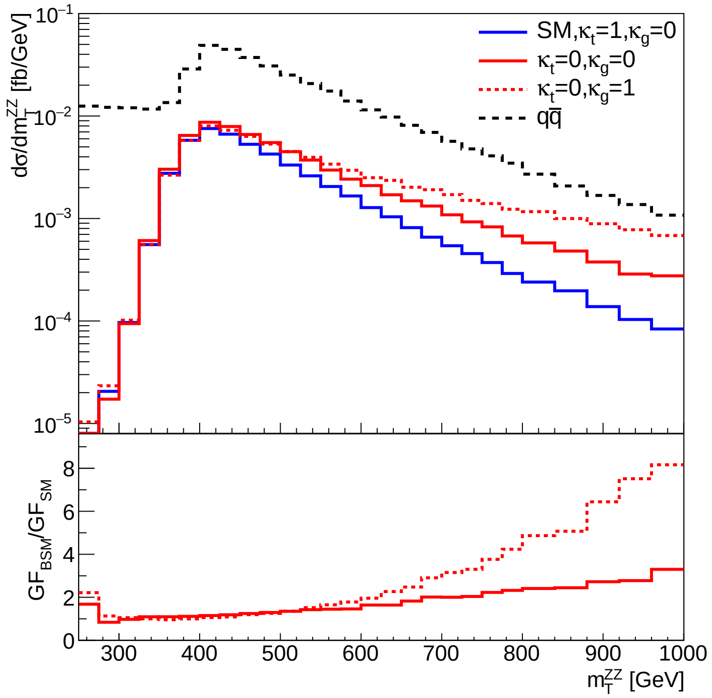

Figure 16: Transverse mass distributions m_T^{ZZ} for the DY and GF $Z(\ell\ell)Z(\nu\nu)$ processes. The new physics effects are parametrized by deviations from the SM point $(\kappa_t, \kappa_g) = (1, 0)$. We follow the benchmark analysis defined in Sec 3.1.

Given that the Higgs boson predominantly decays into longitudinal gauge bosons in the high-energy regime, it is instructive to examine the signal amplitude for the longitudinal components. At $m_{ZZ} \gg m_t, m_H, m_Z$, the amplitudes associated with each contribution depicted in Fig. 15 can be approximated as follows [145, 116, 118]

$$
\begin{aligned}
\mathcal{M}_t^{++00} &\approx +\frac{m_t^2}{2m_Z^2} \log^2 \frac{m_{ZZ}^2}{m_t^2} \,, \\
\mathcal{M}_g^{++00} &\approx -\frac{m_{ZZ}^2}{2m_Z^2} \,, \\
\mathcal{M}_c^{++00} &\approx -\frac{m_t^2}{2m_Z^2} \log^2 \frac{m_{ZZ}^2}{m_t^2} \,.
\end{aligned}
\tag{3.7}
$$

Two important observations can be made. First, both the s-channel top loop amplitude $\mathcal{M}_t$ and the continuum amplitude $\mathcal{M}_c$ exhibit logarithmic dependencies on m_{ZZ}/m_t in the far off-shell regime. In the Standard Model scenario, the ultraviolet logarithm between these two amplitudes cancels out, ensuring a proper high-energy behavior when calculating the full amplitude. Second, there is a difference in sign between the s-channel contributions $\mathcal{M}_t$ and $\mathcal{M}_g$. This results in a destructive interference between $\mathcal{M}_t$ and $\mathcal{M}_c$, whereas a constructive interference is observed between $\mathcal{M}_g$ and $\mathcal{M}_c$. These interference effects play a crucial role in the subsequent exploration of new physics sensitivity with higher precision.

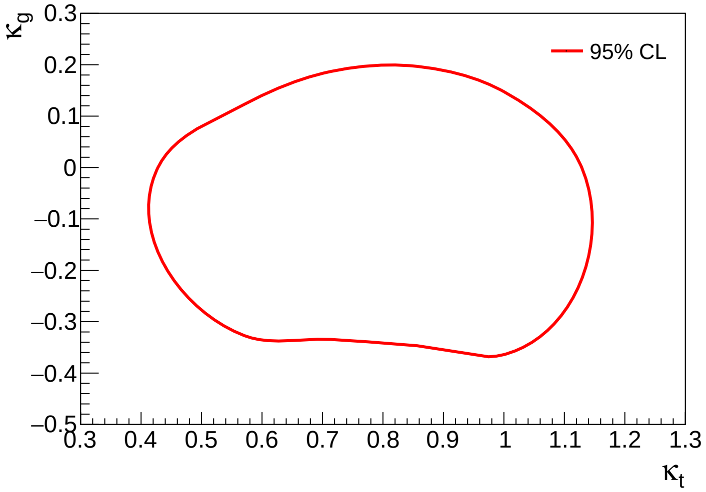

Figure 17: 95% CL bound on the coupling modifiers κ_t and κ_g when accounting for the off-shell Higgs measurement in the $Z(\ell\ell)Z(\nu\nu)$ channel. We assume the 14 TeV LHC with 3 ab^{-1} of data.

By taking advantage of the larger rate for $ZZ \to \ell\ell\nu\nu$ compared to $ZZ \to 4\ell$ [116, 117, 118], we explore the off-shell Higgs physics at the High-Luminosity LHC (HL-LHC). To fully simulate the loop-induced effects, we incorporate Eq. (3.6) into FeynRules/NLOCT [146, 147] by introducing a new fermion state and adjusting its parameters to match the low-energy Higgs interaction $HG_{\mu\nu}G^{\mu\nu}$ [135, 136]. The Feynman rules are then exported to a Universal FeynRules Output (UFO) format [148], and Monte Carlo event generation is performed using MadGraph5aMC@NLO [82].

In Fig. 16, we present the Drell-Yan (DY) and gluon-fusion (GF) m_T^{ZZ} distributions for various signal hypotheses. The bottom panel displays the ratio between the gluon fusion beyond the Standard Model (BSM) scenarios and the gluon fusion in the Standard Model

(SM). Consistent with Eq. (3.7), we observe a suppression of the full process when accounting for the s-channel top loop contributions and an enhancement when including the new physics terms associated with $\mathcal{M}_g$ at high energies.

Following the benchmark analysis defined in Sec. 3.1, we conduct a binned log-likelihood analysis with the m_T^{ZZ} distribution using the events resulting from the BDT study. This analysis takes advantage of the characteristic high-energy behavior of the new physics terms highlighted in Eq. (3.7) and illustrated in Fig. 16. The resulting 95% confidence level (CL) sensitivity to the new physics parameters (κ_t, κ_g) at the high-luminosity LHC is presented in Fig. 17. Specifically, we observe that the LHC can constrain the top Yukawa within the range $\kappa_t \approx [0.4, 1.1]$ at 95% CL using this single off-shell channel. The asymmetry in the limit, with respect to the SM point, is a consequence of the large and negative interference term between the s-channel and the continuum amplitudes. The upper bound on κ_t obtained from this analysis is complementary to the direct Yukawa measurement via ttH [59] and can be further improved through a combination with other relevant off-shell Higgs final states. The results derived in this section are competitive with the CMS HL-LHC projection, which considers the boosted Higgs production and combines the $H \to 4\ell$ and $H \to \gamma\gamma$ channels [4]. The CMS projection yields an upper bound on the top Yukawa of $\kappa_t \lesssim 1.2$ at 95% CL.

3.3 Higgs-Top Form Factor

The fact that the observed mass of the Higgs boson is much lighter than the Planck scale indicates the existence of an unnatural cancellation between the bare mass and the quantum corrections. This observation motivates considering alternative possibilities, such as the idea that the Higgs boson may not be a fundamental particle but rather a composite particle [149, 150, 151, 152]. In this scenario, the Higgs boson is proposed to be a bound state of a strongly interacting sector with a composite scale denoted by Λ. Moreover, in such a composite Higgs scenario, the heaviest particle in the Standard Model, the top quark, can also be composite. This would lead to modifications in the top Yukawa coupling, which can be parametrized by a momentum-dependent form factor at a scale q^2 close to or above the new physics scale Λ^2. However, finding a general construction for such a form factor is challenging without detailed knowledge of the underlying dynamics. To address this, we adopt a phenomenological ansatz inspired by the nucleon form factor [153]. This ansatz provides a useful approach to parametrize the momentum dependence of the top Yukawa coupling in the composite Higgs scenario. It is defined as

$$\Gamma(q^2/\Lambda^2) = \frac{1}{(1+q^2/\Lambda^2)^n}\,, \tag{3.8}$$

where q^2 is the virtuality of the Higgs boson. For the case $n = 2$, the form factor corresponds to a dipole form and describes an exponential spatial distribution. Following the work in Ref. [121], we investigate the effects of this form factor on the process $gg \to H^* \to ZZ$ with the complementary final state $\ell^+\ell^-\nu\bar{\nu}$.

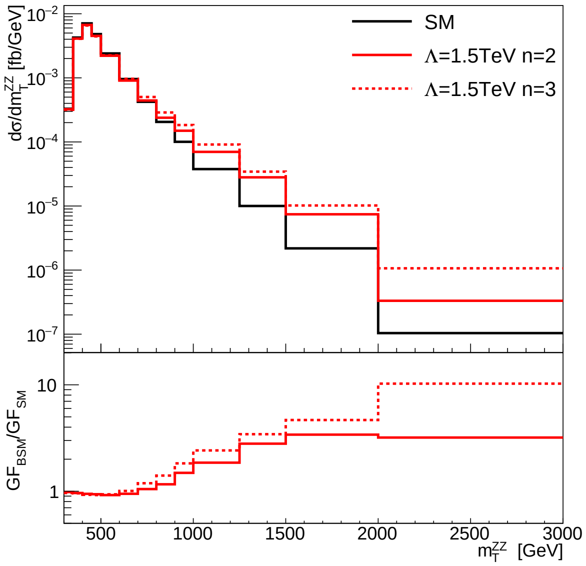

Figure 18: Transverse mass distribution m_T^{ZZ} for $gg(\to H^*) \to Z(2\ell)Z(2\nu)$ in the Standard Model (black) and with a new physics form factor (red). We assume $n = 2, 3$ and $\Lambda = 1.5$ TeV for the form factor scenario.

In Figure 18, we present the m_T^{ZZ} distribution for the full gluon fusion process $gg \to H^* \to ZZ$. We compare the Standard Model prediction (black curve) with scenarios involving the Higgs-top form factor with $n = 2$ or $n = 3$ and a new physics scale $\Lambda = 1.5$

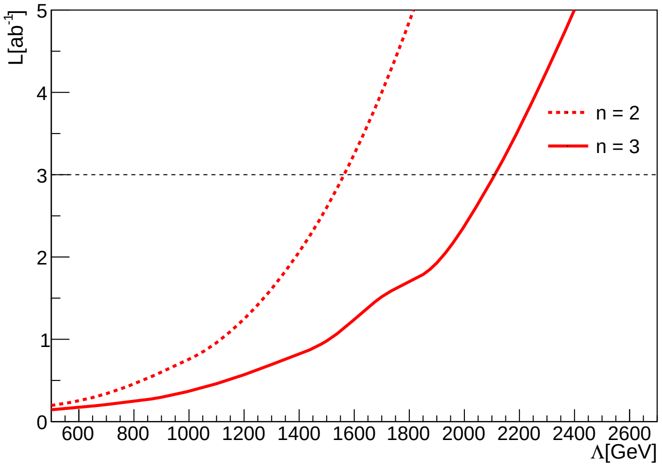

Figure 19: 95% CL sensitivity on the new physics scale Λ as a function of the LHC luminosity. We assume the form factor in Eq. (3.8) with $n = 2$ (dashed line) and $n = 3$ (solid line) at the 14 TeV LHC.

TeV. The differences between the Standard Model and the form factor scenarios become more pronounced when the energy scales are comparable to or above Λ, as the destructive interference between the Higgs signal and the continuum background is suppressed. To fully explore this effect, we perform the same BDT procedure as introduced in Sec. 3.1, followed by a binned log-likelihood ratio test in the m_T^{ZZ} distribution. In Figure 19, we show the sensitivity reach of the LHC in probing the Higgs-top form factor. The LHC can constrain these new physics effects up to a scale of $\Lambda = 1.5$ TeV for $n = 2$ and $\Lambda = 2.1$ TeV for $n = 3$ at the 95% confidence level. The sizable event rate for the $H^* \to ZZ \to \ell\ell\nu\nu$ signal provides a more precise probe into the ultraviolet regime compared to the $H^* \to ZZ \to 4\ell$ channel, where the limits on the new physics scale are $\Lambda = 0.8$ TeV for $n = 2$ and $\Lambda = 1.1$ TeV for $n = 3$ at the 95% confidence level [121].

Table 12: Comparison of the sensitivity reaches between $H^* \to ZZ \to \ell\ell\nu\nu$ in this study and $H^* \to ZZ \to 4\ell$ in the literature as quoted. All results are presented at 95% CL except for the Higgs width projection derived by ATLAS with 68% CL [3]. We assume that the Wilson coefficient for the EFT framework is given by $c_t = v^2/\Lambda^2_{EFT}$. Besides the $H \to 4\ell$ channel, Ref. [4] also accounts for the $H \to \gamma\gamma$ final state with a boosted Higgs analysis.

	Γ_H/Γ_H^{SM}	Λ_{EFT}	$\Lambda^{n=2}_{Composite}$
$H^* \to ZZ \to \ell\ell\nu\nu$	1.31	0.8 TeV	1.5 TeV
$H^* \to ZZ \to 4\ell$	1.3 (68% CL) [3]	0.55 TeV [4]	0.8 TeV [121]

4.0 Directly Probing the Higgs-top Coupling at High Scales

The top-quark Yukawa coupling (y_t) holds significant importance in the Standard Model (SM) as it represents the strongest interaction of the Higgs boson with a value close to 1. Its magnitude plays a central role in Higgs phenomenology within the SM and serves as a potential probe for physics beyond the Standard Model (BSM), particularly associated with electroweak symmetry breaking [154]. This coupling's role is crucial for ensuring the stability of the SM vacuum during the electroweak phase transition in the early universe [155, 156]. Additionally, it contributes the largest quantum correction to the Higgs boson mass, and in various well-motivated new physics scenarios, it can drive the electroweak symmetry breaking [157, 150, 158, 149, 159, 151]. Hence, accurately measuring y_t can be essential in discerning potential new physics effects.

The top-quark Yukawa coupling has been indirectly determined at the LHC through the Higgs discovery channel $gg \to h$ via the top-quark loop [160]. Additionally, it can be directly measured through the process of top pair production in association with a Higgs boson, denoted as $t\bar{t}h$. Both the ATLAS and CMS collaborations reported the observation of this channel in 2018, with respective significances of 6.3 and 5.2 standard deviations [32, 33]. These measurements confirm the Standard Model (SM) expectation that the Higgs boson interacts with the top-quark with a Yukawa coupling of order one. Excitingly, the high-luminosity LHC (HL-LHC) projections anticipate probing the top Yukawa coupling with remarkable precision by the end of the LHC run, achieving an accuracy of approximately $\delta y_t \lesssim \mathcal{O}(4)\%$ [59].

Indeed, current measurements at the LHC mainly probe the electroweak scale $Q \sim v$, where v is the Higgs vacuum expectation value. However, if the new physics scale Λ is significantly larger than the LHC energies, the effects of physics beyond the Standard Model (BSM) are generally suppressed and scale as $(Q/\Lambda)^n$, where n is a positive integer [132, 133, 134], until the energy reaches a new resonance associated with the BSM physics. To enhance the sensitivity to new physics effects, it is desirable to explore the high-energy regime associated with Higgs physics. Recently, there have been proposals to study the off-shell Higgs signals $gg \to h^* \to VV$, where VV represents a pair of electroweak gauge bosons [116, 117, 118, 119, 120, 121, 161]. This process offers the potential to probe and reveal new physics effects related to the tth^* and VVh^* interactions or to observe the propagation of a heavy Higgs-like particle h^* at high energy scales $Q > v$. By exploring this high-energy regime, we can gain valuable insights into possible new physics phenomena beyond the Standard Model.

In this study, we directly investigate the Higgs-top coupling at high energy scales by exploring the $t\bar{t}h$ production channel. This process allows us to probe the top-quark Yukawa interaction at a high scale in both the space-like and time-like regimes when the Higgs is produced on-shell with high transverse momentum. Unlike the off-shell Higgs physics, which primarily probes the time-like domain, the on-shell production of the Higgs allows us to explore complementary physics in both domains [120, 121, 161]. To study the potential Beyond the Standard Model (BSM) effects on the Higgs-top Yukawa interaction, we adopt the Effective Field Theory (EFT) framework. We focus on two relevant higher-dimensional contributions that could modify the Higgs-top interaction. Additionally, we investigate a BSM hypothesis involving a non-local momentum-dependent form factor that describes the Higgs-top interaction [121, 161]. This form factor is motivated by the possibility that the top Yukawa coupling may arise from a composite substructure of the top quark. To optimize our analysis, we concentrate on the channel with the largest Higgs decay branching fraction, $\mathcal{BR}(h \to b\bar{b}) \sim 58\%$, and utilize jet substructure techniques in the boosted Higgs regime. This allows us to combine the large event yield with a high-energy physics probe to maximize the sensitivity to potential BSM effects on the Higgs-top coupling. By adopting this approach, we aim to shed light on the high-energy behavior of the top-quark Yukawa interaction and explore possible new physics phenomena beyond the Standard Model.

The subsequent sections of this chapter are structured as follows. In Section 4.1, we introduce the theoretical parameterization related to potential new physics effects on the Higgs-top couplings within the framework of Effective Field Theory (EFT), along with the inclusion of an interaction form factor. Subsequently, in Section 4.2, we explore the sensitivity of the new physics interactions in the context of the $t\bar{t}h$ production channel, highlighting the advantages of the boosted Higgs regime, which benefits from energy enhancement.

4.1 New Physics parametrization

In this section, we present two distinct parametrizations for potential beyond-the-Standard Model effects on the Higgs-top coupling at high energy scales. The first parametrization is based on the effective field theory (EFT) framework, which involves introducing a few relevant dimension-6 operators. These operators arise from integrating out heavy degrees of freedom that mediate the interactions between the Higgs and top particles. The second parametrization is a non-local Higgs-top form factor, inspired by a strongly interacting composite theory that involves the Higgs and top quarks. These two approaches represent representative forms of new physics parameterizations, capturing the general characteristics of the beyond-the-Standard Model couplings involving the Higgs and top quark.

4.1.1 Effective Field Theory

The Standard Model Effective Field Theory (SMEFT) provides a comprehensive and systematic bottom-up framework for searching for new physics beyond the Standard Model [133, 134, 162, 163, 164, 119, 165]. In this scenario, the particles associated with the new physics are considered to be too heavy to be directly produced on-shell at the energies probed by current experiments. As a result, these heavy states are "integrated out" and their effects are effectively encoded in the form of higher dimension operators, commonly referred to as contact interactions [132]. These higher dimensional operators parametrize the possible deviations from the predictions of the Standard Model and provide a way to explore a wide range of new physics scenarios. In general, the EFT Lagrangian can be written as

$$\mathscr{L}_{\mathrm{EFT}} = \mathscr{L}_{\mathrm{SM}} + \sum_i \frac{c_i}{\Lambda^2}\mathcal{O}_i + \mathcal{O}\left(\frac{1}{\Lambda^4}\right) , \tag{4.1}$$

where Λ is the scale of new physics, $\mathcal{O}_i$ are effective operators of dimension-six compatible with the SM symmetries, and c_i are corresponding Wilson coefficients. Higher dimensional operators can alter the established interactions of the Standard Model and also introduce new Lorentz structures. These modifications and new structures can result in significant

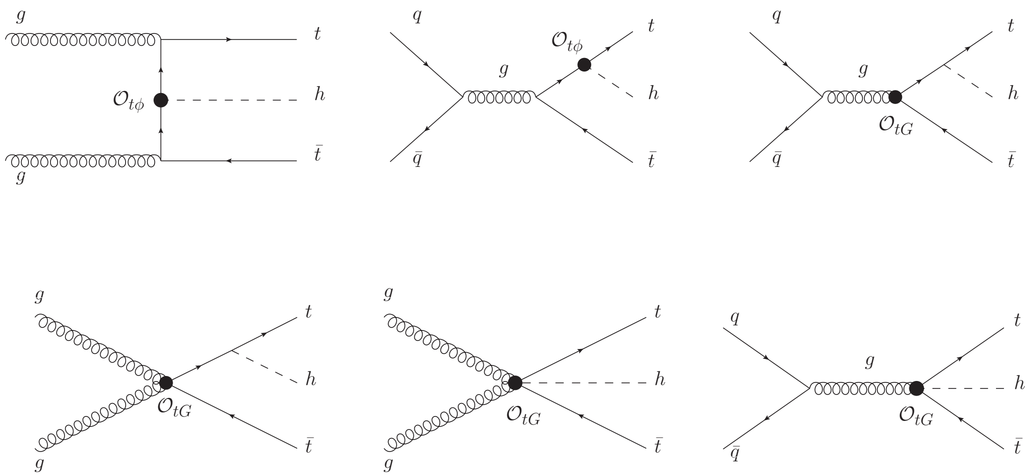

Figure 20: Representative Feynman diagrams contributing to $t\bar{t}h$ production. The black dots represent the BSM vertices arising from the EFT operators.

energy enhancements in the scattering amplitudes, which have important implications for phenomenology.

In our study of new physics effects on the Higgs-top coupling at high scales, we utilize the SMEFT framework and work within the Warsaw basis of operators [134]. Specifically, we concentrate on two-fermion operators, which contribute to $t\bar{t}h$ production at the LHC and are relatively unconstrained at present

$$\mathcal{O}_{t\phi} = (H^\dagger H)(\bar{Q}t)\tilde{H} + \text{h.c.}\,, \tag{4.2}$$

$$\mathcal{O}_{tG} = g_s(\bar{Q}\sigma^{\mu\nu}T_A t)\tilde{H}G^A_{\mu\nu} + \text{h.c.}\,. \tag{4.3}$$

The first operator, denoted as $\mathcal{O}_{t\phi}$, scales the SM top Yukawa coupling. The second operator, denoted as $\mathcal{O}_{tG}$, corresponds to the chromomagnetic dipole moment of the top-quark. The presence of $\mathcal{O}_{t\phi}$ modifies the tth vertex in the SM and leads to a rescaling of the top Yukawa coupling. On the other hand, $\mathcal{O}_{tG}$ not only modifies the gtt vertex, but also gives rise to new interaction vertices, such as $ggtt$, $gtth$, and $ggtth$. This operator has significant phenomenological effects on $t\bar{t}$ processes and can lead to substantial new physics sensitivity in the $t\bar{t}h$ channel [166]. As a result, we include $\mathcal{O}_{tG}$ in our analysis to explore its high energy behavior. In Fig. 20, we present a representative set of Feynman diagrams for $t\bar{t}h$ production arising from the EFT interactions. These diagrams illustrate the possible contributions from the new physics operators to the associated processes. The experimental LHC analyses constrain these Wilson coefficients at 95% Confidence Level (CL) to the ranges [167, 168]

$$c_{t\phi}/\Lambda^2 = [-2.3, 3.1]/\text{TeV}^2, \quad c_{tG}/\Lambda^2 = [-0.24, 0.07]/\text{TeV}^2.$$

Guided by these results, we choose illustrative values of the coefficients as

$$|c_{tG}/\Lambda^2| = 0.1 \text{ TeV}^{-2} \quad \text{and} \quad |c_{t\phi}/\Lambda^2| = 1 \text{ TeV}^{-2}, \tag{4.4}$$

for our following representative kinematic distributions. For recent phenomenological SMEFT global fit studies, see Refs. [162, 163].

4.1.2 Higgs-Top coupling form-factor

The top-quark Yukawa coupling plays a significant role in the naturalness problem, being responsible for the dominant quantum corrections to the Higgs mass. Hence, it becomes crucial to investigate the Higgs-top interaction at high energy scales, even into the ultraviolet regime. One intriguing possibility is that the top-quark and Higgs boson may not be fundamental particles, but rather composite states emerging from new strongly interacting dynamics at a scale Λ [149, 151, 152, 169]. In such scenarios, the top Yukawa coupling might exhibit a momentum-dependent form factor near or above the new physics scale Λ, deviating from a simple point-like interaction. However, writing down a general form factor without specific knowledge of the underlying strong dynamics in the composite scenario can be challenging. To address this, we draw inspiration from the nucleon form factor [153] and adopt the following phenomenological ansatz

$$\Gamma(Q^2/\Lambda^2) = \frac{1}{(1 + Q^2/\Lambda^2)^n}\,, \tag{4.5}$$

where Q is the energy scale associated with the physical process. This educated guess leads to a dipole form-factor for the $n = 2$ scenario, characterized by an exponential spatial

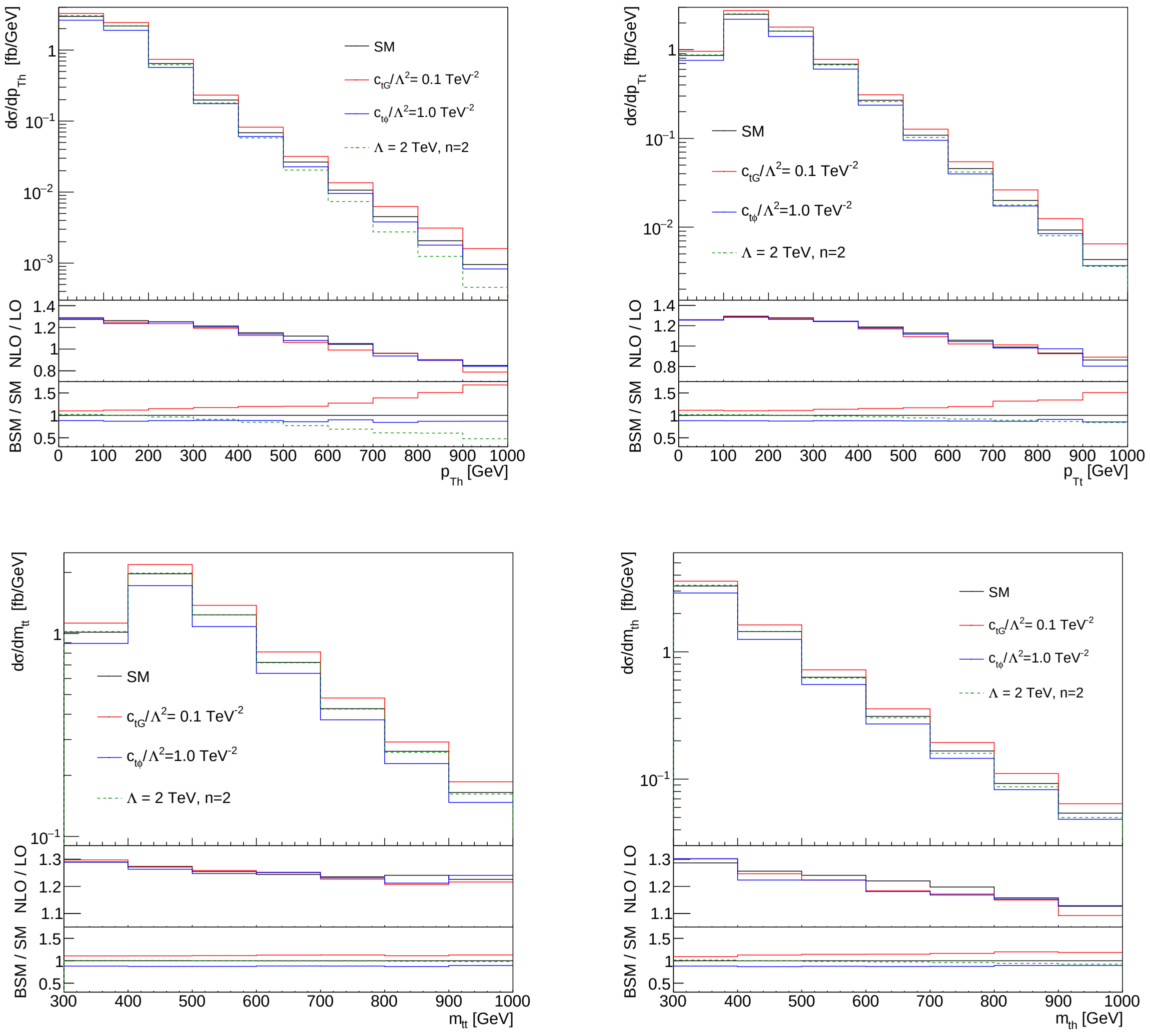

Figure 21: Top panels: Transverse momentum distributions for the Higgs boson p_{Th} (left) and the hardest top-quark p_{Tt} (right). Bottom panels: Invariant mass distributions for the top pair m_{tt} (left) and the Higgs and top-quark m_{th} (right). Each panel shows on the top the $t\bar{t}h$ sample in the SM and new physics scenarios. The results are presented at the NLO QCD fixed order. We also show the local NLO K-factor (middle panel in each figure as NLO/LO) and the ratio between new physics and SM scenarios (bottom panel in each figure as BSM/SM). We assume the LHC at 14 TeV.

distribution in a space-like probe. For higher values of n, we encounter higher multi-poles, which usually result in a more significant suppression of the form factor.

4.2 Analysis

To investigate these new physics effects, we analyze the $pp \to t\bar{t}h$ channel at high energy scales. To achieve this, we exploit the sizable signal event rate along with controlled backgrounds, focusing on the boosted $h \to b\bar{b}$ final state in combination with leptonic top-quark pair decays. The signal signature is characterized by the presence of four b-tagged jets and two opposite-sign leptons. Among the leading backgrounds, in order of significance, are $t\bar{t}b\bar{b}$ and $t\bar{t}Z$.

To simulate the signal and background events, we use `MadGraph5_aMC@NLO` [82]. The samples for $t\bar{t}h$ and $t\bar{t}Z$ processes are generated at NLO in QCD, while the $t\bar{t}b\bar{b}$ sample is generated at LO. The contributions from dimension-six Effective Field Theory (EFT) operators are included through the FeynRules model `SMEFT@NLO` [170]. This implementation allows for one-loop QCD computations, incorporating the EFT effects and accounting for relevant additional radiation at the matrix element level [171]. The event simulation includes showering, hadronization, and underlying event effects, which are modeled using `Pythia8` [85] with the `Monash` tune [172]. To accurately describe the top-quark decays and account for spin correlation effects, we utilize `MadSpin` [84]. For the parton distribution functions (PDFs), we use MMHT2014 NLO with $\alpha_S(m_Z) = 0.118$ [173] in the five-flavor scheme. The values of relevant parameters are set to $m_t = 172$ GeV, $m_h = 125$ GeV, $m_Z = 91.1876$ GeV, $m_W = 79.82$ GeV, and $G_F = 1.16637 \times 10^{-5}$ GeV^{-2}. We fix the scales to a constant value of $\mu_F = \mu_R = m_t + m_h/2$ to be consistent with previous studies [166]. The LHC center-of-mass energy is assumed to be $\sqrt{s} = 14$ TeV.

Precise theoretical calculations are essential for robust new physics studies at the LHC. Higher order QCD corrections play a significant role and can be conventionally estimated by a K-factor, representing the ratio between NLO and LO predictions. These higher order corrections can have a substantial impact on the results. To illustrate the effects of higher order

QCD corrections and new physics contributions at high energies, we present in Fig. 21 the NLO fixed-order parton-level distributions for several relevant kinematic observables associated with the $t\bar{t}h$ signal sample. Specifically, we show the transverse momentum distribution of the Higgs boson, denoted as p_{Th} (upper left), the transverse momentum distribution of the hardest top-quark, denoted as p_{Tt} (upper right), the invariant mass distribution of the top quark pair, denoted as m_{tt} (lower left), and the invariant mass distribution of the Higgs and top-quark system, denoted as m_{th} (lower right). These distributions provide valuable insights into the dynamics of the $t\bar{t}h$ production and serve as the basis for further analysis of the new physics effects and precision studies. Indeed, the higher order QCD corrections are not universal and can exhibit significant kinematic dependencies. This is evident in the NLO/LO ratio, where we observe variations of about $20\% - 30\%$ across different kinematic observables, as shown in the panels of Fig. 21. This highlights the importance of including higher order predictions in the full differential analysis, as a global NLO K-factor would not be sufficient to capture these kinematic-dependent corrections accurately.

The panels of BSM/SM in Fig. 21 demonstrate that new physics contributions can indeed sensitively depend on the kinematics of the process. For instance, at high transverse momenta of the on-shell top quark or Higgs boson, the $t\bar{t}h$ production process can probe both the space-like and time-like regimes for the top-Higgs interactions. Notably, the operator $\mathcal{O}_{tG}$ exhibits a significant energy enhancement, particularly evident in the transverse Higgs momentum distribution. This enhancement starts with a 10% increase in the non-boosted regime with $p_{Th} < 100$ GeV and can reach up to 65% enhancement for $p_{Th} = 1$ TeV. In contrast, the form-factor scenario displays a depletion in the cross-section at higher energies due to the generic dipole suppression. The rate is reduced by 5% at $p_{Th} = 200$ GeV, and the suppression becomes even more pronounced, reaching 55% at $p_{Th} = 1$ TeV. For the form-factor scenario, we adopt a representative scale $Q = p_{Th}$ to account for the suppression. On the other hand, new physics effects associated with the operator $\mathcal{O}_{t\phi}$ do not result in a distinct energy profile with respect to the SM. In the $t\bar{t}h$ process, this operator only contributes with a shift to the top Yukawa coupling, resulting in a flat rescaling of the cross-section compared to the SM, independent of the process energy scale. Despite the lack of a manifest energy enhancement, this new physics contribution can still be probed in our high energy scale analysis, benefiting from the controlled backgrounds at the boosted Higgs regime, as we will show in the subsequent sections.

The boosted Higgs analysis, in conjunction with jet substructure techniques, effectively suppresses the initially overwhelming backgrounds for the $t\bar{t}h$ signal with dileptonic top decays and $h \to b\bar{b}$, as demonstrated in Ref. [174]. In our approach, we adopt a similar strategy. Our analysis begins by requiring the presence of two isolated and opposite sign leptons with transverse momentum $p_{T\ell} > 10$ GeV and pseudorapidity $|\eta_\ell| < 3$. For the hadronic part of the event, we reconstruct jets using the Cambridge-Aachen algorithm with a jet radius parameter of $R = 1.2$ [175]. We then demand the presence of at least one boosted fat-jet with transverse momentum $p_{TJ} > 200$ GeV and pseudorapidity $|\eta_J| < 3$. Furthermore, we require that one of the fat-jets be Higgs tagged using the Butterworth-Davison-Rubin-Salam (BDRS) algorithm [176, 177]. The Higgs tagging procedure with the BDRS algorithm involves identifying three subjets within the fat-jet. This is achieved by gradually shrinking the jet radius until the fat-jet splits into three filtered jets. The radius of separation among the filtered jets is defined as $R_{\text{filt}} = \min(0.3, R_{bb}/2)$. Among the three filtered jets, the two hardest are required to be b-tagged, while the third filtered jet corresponds to the dominant $\mathcal{O}(\alpha_s)$ radiation from the Higgs decay. This Higgs tagging technique helps to distinguish the $t\bar{t}h$ signal from the background processes with similar final states, significantly improving the signal-to-background ratio.

Since we have only one hadronically decaying heavy particle, namely the Higgs boson, we can improve the event reconstruction by using a smaller jet size to reduce the contamination from the underlying event. Thus, we remove all hadronic activity associated with the Higgs fat-jet and re-cluster the remaining particles using the anti-k_t jet algorithm with a jet radius of $R = 0.4$. We then require the presence of two b-tagged jets with transverse momentum $p_{tb} > 30$ GeV and pseudorapidity $|\eta_b| < 3$. As our final state includes a total of four b-tagged jets, we take advantage of the expected improvements in the central tracking system for the HL-LHC run to enhance the event rate for our signal. Based on the ATLAS report [178], we assume an 85% b-tagging efficiency and a 1% mistag rate for light jets. To further suppress the backgrounds, we impose a cut on the filtered mass for the Higgs candidate to be around the Higgs boson mass, requiring $|m_h^{\text{BDRS}} - 125 \text{ GeV}| < 10$ GeV. More details on the cut-flow analysis are provided in Table 13. These selection criteria help to significantly enhance the signal-to-background ratio and improve the sensitivity to the $t\bar{t}h$ process.

Table 13: Cut-flow for signal and backgrounds at LHC $\sqrt{s} = 14$ TeV. The selection follows the BDRS analysis described in the text. Rates are in units of fb and account for 85% (1%) b-tag (mistag) rate, hadronization, and underlying event effects.

cuts	$t\bar{t}h$	$t\bar{t}b\bar{b}$	$t\bar{t}Z$
BDRS h-tag, $p_{T\ell} > 10$ GeV, $\lvert\eta_\ell\rvert < 3$, $n_\ell = 2$	3.32	6.35	1.02
$p_{Tj} > 30$ GeV, $\lvert\eta_j\rvert < 3$, $n_j \geq 2$, n_b=2	0.72	1.97	0.22
$\lvert m_h^{\mathrm{BDRS}} - 125\rvert < 10$ GeV	0.15	0.14	0.009

4.2.1 Scale for the EFT operators

In Fig. 22, we move beyond the partonic level calculation and present the hadron level transverse momentum distribution (p_{Th}) for the Higgs boson candidate from the $pp \to t\bar{t}h$ channel, including contributions from the Standard Model (SM) as well as the Effective Field Theory (EFT) operators. We also include the leading backgrounds $t\bar{t}b\bar{b}$ and $t\bar{t}Z$. The boosted Higgs search complements our study of new physics effects, as shown in Fig. 21. At higher energy scales, both the backgrounds are further suppressed, while the new physics contributions become more pronounced. Notably, we observe a significant enhancement from the $\mathcal{O}_{tG}$ operator at high energy scales. This suggests that the boosted Higgs regime provides a promising avenue for probing and distinguishing new physics effects from the SM background in the $t\bar{t}h$ channel.

In order to quantify the sensitivity of the boosted Higgs analysis to the new physics effects, we perform a binned log-likelihood analysis on the p_{Th} distribution. The results are presented in Fig. 23, showing the 68% and 95% confidence level (CL) limits on the Wilson coefficients ($c_{tG}/\Lambda^2, c_{t\phi}/\Lambda^2$). For our analysis, we assume the High-Luminosity LHC (HL-LHC) operating at 14 TeV with an integrated luminosity of 3 ab^{-1}. To account for the uncertainty in the EFT expansion, we consider terms up to linear and quadratic order in

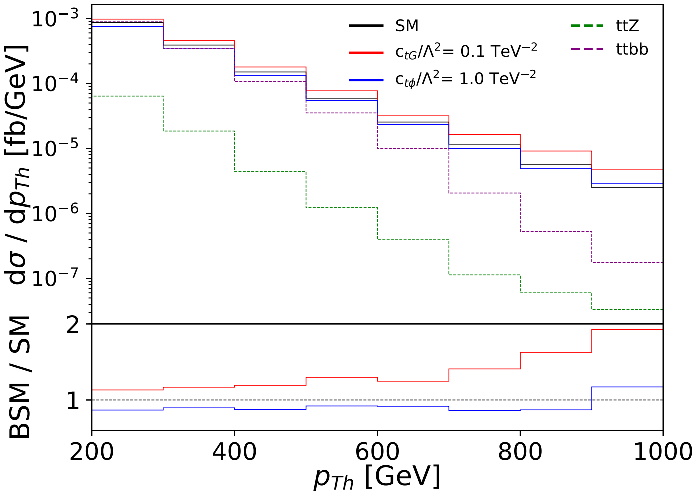

Figure 22: Transverse momentum distribution of the Higgs boson p_{Th} for the $t\bar{t}h$ sample in the SM (black) and new physics scenarios with $c_{tG}/\Lambda^2 = 0.1$ TeV^{-2} (red), $c_{t\phi}/\Lambda^2 = 1$ TeV^{-2} (blue). The leading backgrounds $t\bar{t}b\bar{b}$ (purple) and $t\bar{t}Z$ (green) are also presented. We assume the LHC at 14 TeV.

the Wilson coefficients c_i/Λ^2. We find that the differences between these two scenarios are small, indicating the robustness of our results.

Recently, CMS reported an EFT interpretation using associated top quark production data with an integrated luminosity of $\mathcal{L} = 41.5$ fb^{-1} [179]. The signal samples included the $t\bar{t}h$ and thq processes, which are directly sensitive to the top-quark Yukawa coupling. The resulting constraints at the 95% confidence level (CL) for the chromomagnetic operator were in two regions: $c_{tG}/\Lambda^2 = [-1.26, -0.69]$ TeV^{-2} and $[0.08, 0.79]$ TeV^{-2}. For the $\mathcal{O}_{t\phi}$ operator, the constraints were $c_{t\phi} = [-14.12, -1.46]$ TeV^{-2} and $[32.30, 44.48]$ TeV^{-2}. While the CMS analysis did not focus on very high energy scales and used the leptonic Higgs decays, our study explores the largest Higgs branching ratio, $h \to b\bar{b}$, in the boosted Higgs regime, leading to significantly higher sensitivities at the HL-LHC.

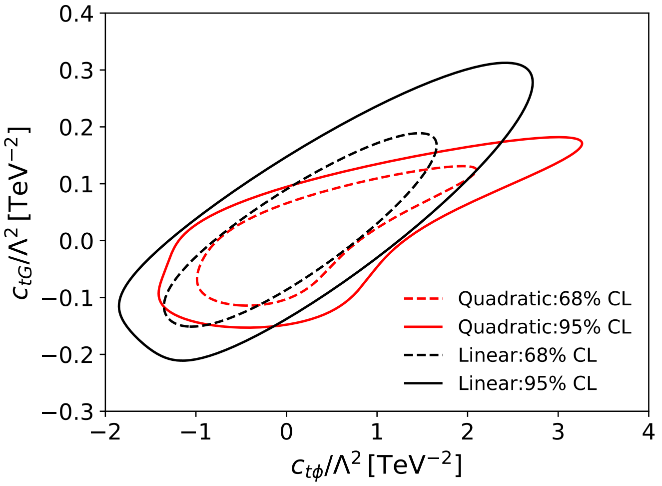

Figure 23: 95% (full line) and 68% (dashed line) CL limits on the Wilson coefficients $(c_{tG}/\Lambda^2, c_{t\phi}/\Lambda^2)$ at the 14 TeV HL-LHC with 3 ab^{-1} of data. The results are presented both at the linear (black) and quadratic (red) order in dimension-6 SMEFT operator coefficients.

4.2.2 Probing the form-factor

In Fig. 24, we present the transverse momentum distribution (p_{Th}) for the Higgs boson candidate from the $pp \to t\bar{t}h$ channel in the Standard Model (SM) and the form-factor contribution. We consider two hypotheses: $n = 2$ and $n = 3$, with the new physics scale $\Lambda = 2$ TeV. While it can be challenging to probe beyond-the-Standard Model (BSM) effects at relatively small scales, these contributions can be effectively enhanced in the boosted regime. For instance, starting at $p_{Th} \sim 200$ GeV with $n = 2$ ($n = 3$), we observe a 5% (9%) effect. Moving to $p_{Th} \sim 400$ GeV, the new physics results in a larger depletion of 18% (25%) compared to the SM hypothesis.

With our boosted $h \to b\bar{b}$ analysis, which provides a relatively large event rate, we have the advantage of probing large energy scales with sufficient statistics. To achieve this, we conduct a comprehensive study of the p_{Th} distribution using a binned log-likelihood analysis. The results of the new physics sensitivity are presented in Fig. 25. The High-Luminosity

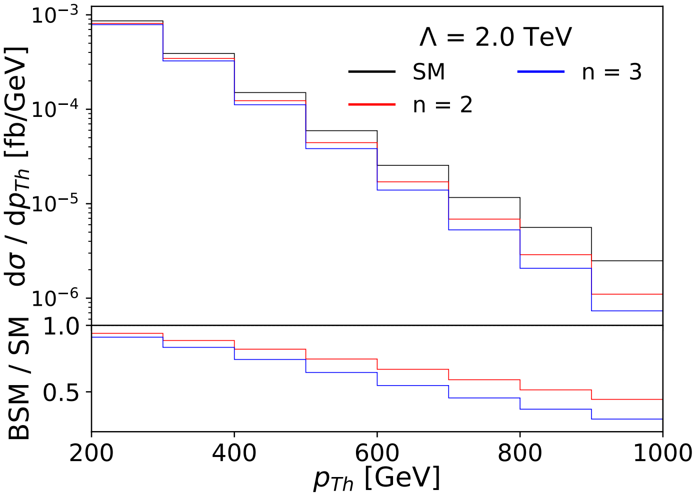

Figure 24: Transverse momentum distribution of the Higgs boson p_{Th} for the $t\bar{t}h$ sample in the SM (black) and new physics scenarios with $n = 2$ (red) and $n = 3$ (blue), assuming $\Lambda = 2$ TeV. We assume the LHC at 14 TeV.

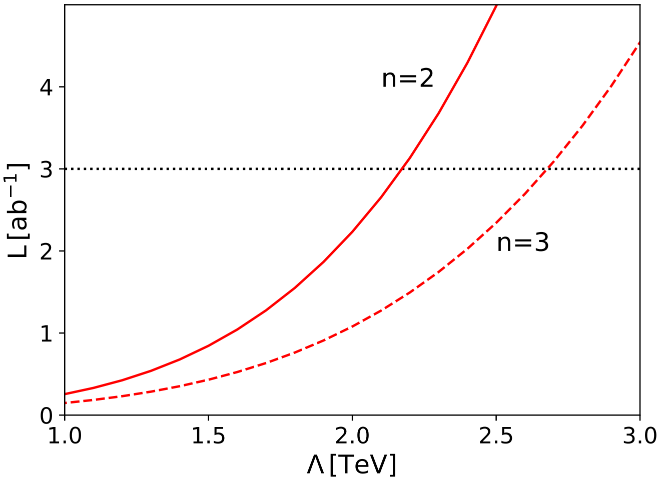

Figure 25: 95% CL sensitivity on the new physics scale Λ as a function of the LHC luminosity. We consider two form-factor scenarios: $n = 2$ (solid line) and $n = 3$ (dashed line).

LHC (HL-LHC) running with 3 ab^{-1} of data will be capable of probing these new physics effects up to a scale of $\Lambda = 2.1$ TeV for $n = 2$ and $\Lambda = 2.7$ TeV for $n = 3$ at 95% confidence level (CL). These findings complement the off-shell Higgs analyses ($gg \to h^* \to ZZ$), where, assuming $n = 3$, the limits on the new physics scale are $\Lambda = 1.1$ TeV for the 4ℓ final state and $\Lambda = 2.1$ TeV for the $\ell\ell\nu\nu$ final state [121, 161]. Our boosted Higgs analysis offers a valuable and distinct approach to explore new physics effects at high energy scales and complements the information gained from other channels.

Table 14: Summary results from the $t\bar{t}h$ studies for the Higgs-top coupling at high scales in terms of the dimension-6 operators and general form-factor scenarios. The results are shown at 95% CL, and we assume the HL-LHC at 14 TeV with 3 ab^{-1} of data. For comparison, we also show the results from off-shell h^* studies, the ATLAS Higgs combination with 139 fb^{-1}, and the CMS top pair bound with 35.9 fb^{-1}.

	channel	c_i/Λ^2 [TeV^{-2}] 95% CL bounds	$\Lambda/\sqrt{c_i}$ [TeV] BSM scale
$c_{t\phi}$	$t\bar{t}h$ (this work)	$[-1.04, 1.00]$	1.0
	$h^* \to ZZ \to \ell\ell\nu\nu$ [161]	$[-2.8\ , 1.5]$	0.6
	$h^* \to ZZ \to 4\ell$ [121]	$[-3.3\ , 3.3]$	0.55
	Higgs comb. ATLAS [167]	$[-2.3\ , 3.1]$	0.57
c_{tG}	$t\bar{t}h$ (this work)	$[-0.11\ , 0.12]$	2.9
	$t\bar{t}$ CMS [168]	$[-0.24\ , 0.07]$	2.1
form-factor $n = 2$	$t\bar{t}h$ (this work)	-	2.1
	$h^* \to ZZ \to \ell\ell\nu\nu$ [161]	-	1.5
	$h^* \to ZZ \to 4\ell$ [121]	-	0.8
form-factor $n = 3$	$t\bar{t}h$ (this work)	-	2.7
	$h^* \to ZZ \to \ell\ell\nu\nu$ [161]	-	2.1
	$h^* \to ZZ \to 4\ell$ [121]	-	1.1

Table 14 presents a summary of the new physics scale reach obtained in our work and other studies for different channels. It is evident from the table that the direct probe of $t\bar{t}h$ in the boosted Higgs regime provides highly competitive and improved sensitivity to new physics effects compared to other channels. The large event rate and the use of jet substructure techniques in the boosted $h \to b\bar{b}$ analysis enable us to explore high energy scales with enhanced statistics, leading to stronger constraints on the new physics scale Λ.

5.0 Using Vector Boson Fusion for High-Scale New Physics

The milestone discovery of the Higgs boson (h) by the ATLAS [180] and CMS [181] collaborations at the CERN Large Hadron Collider (LHC) is of great theoretical and experimental significance in understanding our microscopic world. The Standard Model (SM) of the strong and electroweak interactions, along with the Higgs mechanism, provides us with a consistent theoretical framework valid up to high scales. On the other hand, we are still lacking an understanding of if and how the Higgs mass, the only dimensionful parameter in the theory, is stabilized against quantum corrections from a higher new physics scale $-$ the mass hieraracy problem [182, 183, 184]. It is thus of fundamental importance to experimentally probe the Higgs interactions at higher energy scales, which should hold the key to understanding the hierarchy problem.

Some efforts have been made along these lines to probe the largest SM coupling $ht\bar{t}$ at the LHC in high scales via the leading production $gg \to h \to ZZ$ [161] and the associated production $gg \to t\bar{t}h$ [185]. The next leading production mechanism of the Higgs boson is the process by which two vector bosons collider to produce a Higgs boson, known as vector boson fusion (VBF). With the Higgs coupling directly proportional to the gauge boson mass, this process is one of the most direct probes of electroweak symmetry breaking that we have. It is well known that without a Higgs boson, the amplitude for the longitudinally polarized gauge boson scattering exhibits quadratic growth with energy, violating perturbative unitarity at a scale of $\Lambda \approx 2.2$ TeV [186, 187]. This is cornerstone of the no-lose theorem of the Large Hadron Collider (LHC) uncovering the first step of electroweak symmetry breaking [11, 188, 12].

The traditional VBF signal leverages the fact that the two outgoing quarks exchange a relatively low amount of momentum with the vector bosons. These quarks, often called tagging jets, tend to have high pseudorapidity (η) and low transverse momentum (p_T), dictated by the (collinear) W propagator (see Refs. [189, 190, 191, 192, 193, 194] for reviews). Signal regions are then defined by an upper cut on the tagging jet and a lower cut on the tagging jet. As expected, the VBF processes have contributed to the Higgs boson discovery [195, 196]. In the hope to probe Higgs physics at a high scale, an alternative approach is to examine the Higgs boson with a higher momentum. This signal region, by contrast, would look to isolate events with a large momentum exchange between the vectors and the quarks. At a cost of lower signal event rate, we may have increased sensitivity to physics beyond the Standard Model (BSM).

The first demonstration of this signal configuration was performed in Ref. [197] where the authors showed that VBF with a high momentum Higgs has sensitivity to dimension-6 operators. They primarily used the $\gamma\gamma$ decay channel of the Higgs which has a small branching ratio, but allows the Higgs four-vector to be fully reconstructed. They found with 300 fb^{-1} a limit of $\Lambda > 2.9$ TeV (at 68% C.L., assuming $\mathcal{O}(1)$ Wilson coefficients) could be set on the scale of new physics. [198, 199, 200, 80, 197, 201, 202, 203] [1]

In this work, we first point out that the high momentum Higgs region can be effectively isolated by cutting on the tagging jets (instead of the Higgs p_T). It it still optimal to cut on Higgs p_T, however, in channels where that is not possible, for example $W(\ell\nu)W(\ell\nu)$, cutting on the tagging jets only loses a little sensitivity.

Secondly, we compare the results using the $b\bar{b}$ decay of the Higgs, including detector simulation and backgrounds. A sample Feynman diagram for this process is shown in Fig. 26. We find that sensitivity is not as good as the $\gamma\gamma$ channel, primarily due to the fact that the Higgs mass resolution is reduced. Combining the multiple channels would further improve the overall sensitivity.

---

[1] Note that diboson events probe the same dimension-6 operators and have a better reach for new physics [204, 205, 206, 207, 208, 209, 210, 211, 212, 213, 214, 215, 216, 217, 218].

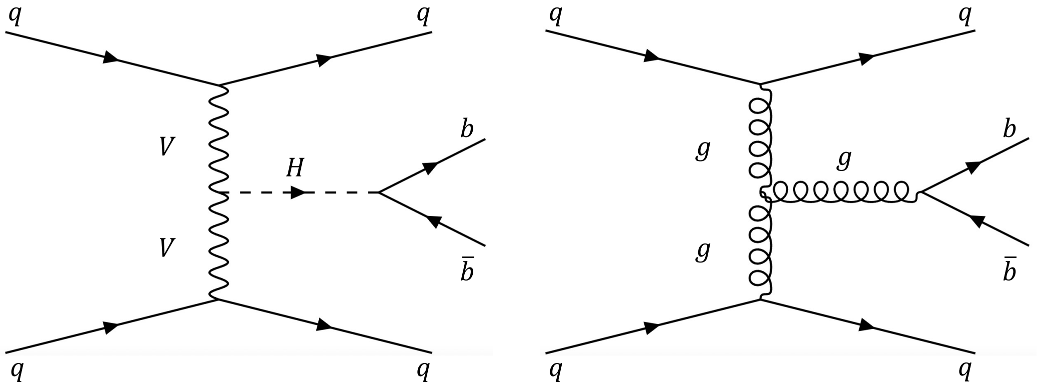

Figure 26: Representative Feynman diagrams of vector boson fusion (left) and QCD background (right).

The outline of this chapter is as follows. In Sec. 5.1 we describe the parametrizations we use for new physics. Section 5.2 studies the kinematics of this topology and compares a few approximations. Next, we discuss the details of our simulation in Sec. 5.3. The results are shown in Sec. 5.4.

5.1 New Physics Parameterization in VBF

In this section, we describe the parametrizations we use for exploring new physics associated with the Higgs production at high scales.

5.1.1 Higher-Dimensional Operators

A consistent and convenient scheme to parameterize new physics effects from a higher scale is the effective field theory (EFT) approach with higher dimensional operators. At the dimension-6 level, there are four operators to contribute to the interactions of our current interest $q\bar{q}VH$. In the Warsaw basis [134], they are written as $\mathcal{O}_Q^{(3)}$, $\mathcal{O}_Q$, $\mathcal{O}_R^u$, and $\mathcal{O}_R^d$ [204]

$$\mathcal{O}_Q^{(3)} = (\bar{Q}\sigma^a\gamma^\mu Q)(iH^\dagger\sigma^a\overleftrightarrow{D}_\mu H), \tag{5.1a}$$

$$\mathcal{O}_Q = (\bar{Q}\gamma^\mu Q)(iH^\dagger\overleftrightarrow{D}_\mu H), \tag{5.1b}$$

$$\mathcal{O}_R^u = (\bar{u_R}\gamma^\mu u_R)(iH^\dagger\overleftrightarrow{D}_\mu H), \tag{5.1c}$$

$$\mathcal{O}_R^d = (\bar{d_R}\gamma^\mu d_R)(iH^\dagger\overleftrightarrow{D}_\mu H), \tag{5.1d}$$

where we follow the usual parametrization of dimension-6 operators according to

$$\Delta\mathcal{L}_{d=6} = \sum_i \frac{c_i}{\Lambda^2}\mathcal{O}_i. \tag{5.2}$$

The coefficients c_i are dimensionless effecive couplings. From an effective field theory perspective the coefficients c_i could have either sign and any values $\lesssim (4\pi)^2$ [219, 220]. In Sec. 5.4 we will see that the sign of c_i matters since the leading new physics contribution is the interference between new physics and the SM. The scale of new physics is Λ. In principle, it can be different for each operator $\mathcal{O}_i$ but we use a common value for simplicity (or equivalently absorb differences in scale into the coefficients).

The expected size of the c_i is $\mathcal{O}(1)$ in known beyond the SM theories [221]. Coefficients as large as $c_i \approx (4\pi)^2$ are technically possible, but require the unlikely scenario of strong coupling between new physics and all particles of the $q\bar{q}VH$ interaction. Even a coupling of $c_i \approx 4\pi$ is not likely [222, 204].

Ref. [204] studied these operators in diboson production ($q\bar{q} \to VV$ and $q\bar{q} \to Vh$) and called them the "high energy primaries." They found that with 300 fb^{-1} the operator $c_Q^{(3)}$ could be probed up to scales of $\Lambda \approx 3$ TeV. The most sensitive diboson channels include a final state W which means only the high energy primary that is probed is $\mathcal{O}_Q^{(3)}$. The other operators required channels such as Zh, which is sensitive to a linear combination of the operators in Eq. (5.1). Ref. [206] studied the $Z(\ell^+\ell^-)h(b\bar{b})$ in detail and found that the scale 2.4 TeV was probed in this channel.

It was pointed out in Ref. [197] that these same operators in Eq. (5.1) contribute to vector boson fusion. Combining the channels $h(\gamma\gamma)jj$ and $h(\tau^+\tau^-)jj$ is sensitive to the scale 2.9 TeV with 300 fb^{-1}, but at 68% C.L. rather than 95% C.L. As expected, VBF has less overall reach compared to diboson, however since it probes a different linear combination of operators, it is an essential input.

5.1.2 Form Factors

If the underlying mechanism for electroweak symmetry breaking is due to some new strong dynamics, it is conceivable to consider that the Higgs boson may not be fundamental, but a composite particle arising from a strongly interacting new dynamics at a scale Λ [151]. In such scenarios, the Higgs interaction may exhibit a momentum-dependent form-factor near or above the new physics scale Λ, rather than a point-like interaction. It is challenging to write a form-factor, in a general form, without prior knowledge of the strong dynamics of the specific composite scenario. Inspired by the nucleon form-factor [153], we adopt the following phenomenological ansatz by adding a form factor to the hW^+W^- vertex

$$(gm_W)hW^+W^- \to \Gamma(Q^2; n, \Lambda^2)(gm_W)hW^+W^-, \tag{5.3}$$

where the form factor is of the form [161, 185]

$$\Gamma(Q^2; n, \Lambda^2) = \frac{1}{(1 + Q^2/\Lambda^2)^n}. \tag{5.4}$$

This form factor approaches unity as $Q^2/\Lambda^2 \to 0$ and suppresses this interaction as Q^2/Λ^2 grows. The suppression depends on the value of n chosen; the larger n is, the faster the suppression. $n = 2$ corresponds to a dipole form factor, as often adopted for the nucleon form factor. In our study we use $Q = p_T^h$ since the transverse momentum of the Higgs characterizes the momentum exchange.

Another option, which we do not pursue in this study, is to use form factors computer from integrating out heavy resonances [223].

5.2 VBF Kinematics

It is important to explore the kinematics of the Higgs boson produced in vector boson fusion in the hope to optimize the dynamical effects. The main purpose is to identify to what extent the phase space with a boosted Higgs can be isolated purely from the kinematics of the two tagging jets.[2]

At leading order there are three objects in the final state: the Higgs h and two tagging jets j_1 and j_2 (where $p_T(j_1) \geq p_T(j_2)$ by convention). Balancing transverse momentum leads to the relationship

$$(\tilde{p}_T^h)^2 = (p_T^{j_1})^2 + (p_T^{j_2})^2 + 2p_T^{j_1}p_T^{j_2}\cos(\phi^{j_1} - \phi^{j_2}), \tag{5.5}$$

where $\phi(x)$ is the azimuthal angle of object x. The notation $\tilde{p}_T(h)$ is to indicate that this would be the transverse momentum of the Higgs in the three-body limit.

There are two notable limits of Eq. (5.5). The first is when $p_T(j_2) \ll p_T(j_1), p_T(h)$. In this case the transverse momentum of the Higgs is primarily balanced by the hardest jet and the three-body space approximately collapses to a two-body space. Even at the high luminosity LHC this limit is out of reach. It could be relevant at a future collider.

The second is when $\cos(\phi^{j_1} - \phi^{j_2}) = \mathcal{O}(1)$. Then $p_T^h \approx p_T^{j_1} + p_T^{j_2}$. In Fig. 27 we compare this quantity with p_T^h and with $\tilde{p}_T^h$ from Eq. (5.5). The events are generating with $p_T^h \geq 150$ GeV. The quantity $\tilde{p}_T^h$ is generally an underestimate due to additional radiation that is ignored in the three-body limit. Empirically, $p_T^{j_1} + p_T^{j_2}$ is a reasonable proxy for p_T^h at high values of p_T^h.

---

[2] In the $b\bar{b}$ channel that we study here, as well as in the $\gamma\gamma$ and hadronic $\tau^+\tau^-$ channels [197] the Higgs is fully reconstructable so one can always directly use $p_T(H)$. Using the tagging jets would be useful in other channels like WW or ZZ.

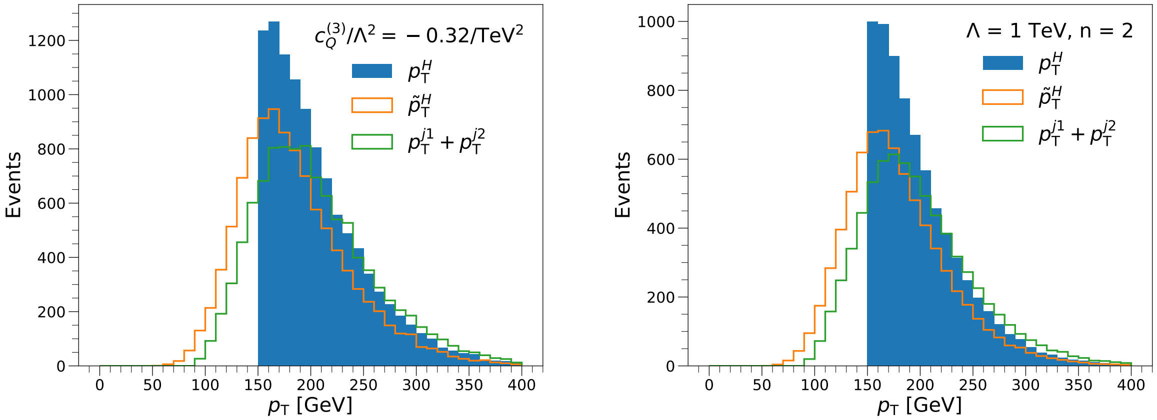

Figure 27: Distribution of Higgs p_T-like variables for operator $\mathcal{O}_Q^{(3)}$ (left) and for the form factor (right).

A number of other Higgs p_T-like variables can be studied. These include $p_T^{j_1}$, $p_T^{j_2}$, and the geometric mean $\sqrt{p_T^{j_1}\, p_T^{j_2}}$ which was suggested in [198, 202]. Fig. 29 will show the search significance as a function of a cut on these variables. We find that $p_T(h)$ gives the best results, followed closely by $p_T(j_1) + p_T(j_2)$ and $\tilde{p}_T^h$. The other Higgs p_T-liked variables are not sufficiently correlated with p_T^h to be optimal in a new physics search.

5.3 Event Simulation

We generate events using `MadGraph 5` 2.7.3 [224]. Both signal and background are generated at leading order at a center-of-mass energy $\sqrt{s} = 13$ TeV with parton distribution functions NNPDF23_lo_as_0130_qed [126]. Events are showered and hadronized with `Pythia` 8.302 [85], and detector simulation is performed by `Delphes` 3.4.1 [87]. Jets are reconstructed with the anti-k_T algorithm with radius $R = 0.5$ [88]. For b-tagging we use the truth flavor from `Delphes` and apply a flat b-tagging efficiency.

Our signal is the process $pp \to h(\to b\bar{b})jj$ with either the dimension-6 operators or the form factor turned on. This process includes the contributions purely from new physics, purely from the Standard Model, and from interference between new physics and the Standard Model. We label the signal as `BSM`. We use dimension-6 operators from the `SMatNLO` model [170].

There are two dominant backgrounds: the Standard Model VBF contribution and the Standard Model QCD contribution. The Standard Model VBF includes a resonant Higgs and is generated from $pp \to h(\to b\bar{b})jj$ with all new physics contributions set to zero. This background is irreducible. We label this background as `VBF`. The QCD background is generated by $pp \to b\bar{b}jj$. We label this background as `QCD`.

5.3.1 Pre-Selection and Validation

We apply cuts to the detector-level events in two stages. The first is the pre-selection which we use for validation with the forward event selection from ATLAS [5] and is listed in this section. The second is the event selection which will be described in the following section. Cuts applied at the generator level are listed in App. C.

We denote b_1 and b_2 as the leading and sub-leading b-tagged jets which form the highest p_T b-jet pair in the events. j_1 and j_2 refer to the tagging jets, where j_1 is the jet with highest p_T and j_2 is the sub-leading jet

- $p_T(b_1) > 85$ GeV and $|\eta(b_1)| < 2.5$. The operating point used for b-tagging this b-jet has a 77% tagging efficiency.
- $p_T(b_2) > 65$ GeV and $|\eta(b_2)| < 2.5$. The operating point used for b-tagging this b-jet has a 85% tagging efficiency.
- $p_T(j_1) > 60$ GeV and $3.2 < |\eta(j_1)| < 4.5$.[3]
- $p_T(j_2) > 30$ GeV and $|\eta(j_2)| < 4.5$.
- $p_T(b\bar{b}) > 150$ GeV, where $p_T(b\bar{b})$ is the transverse momentum of the $b\bar{b}$ system.

To validate our analysis, we compare our `VBF` and `QCD` event yields with the ATLAS study [5] with the above pre-selection applied. The numerical results are shown in Tab. 15. Note

---

[3] Note that j_1 is always the hardest jet. An event where, for example, $p_T(j_1) = 90$ GeV, $\eta(j_1) = 3.0$, $p_T(j_2) = 80$ GeV, $\eta(j_2) = -4.0$ does not pass the selection.

that [5] is searching for the Standard Model Higgs signal so their signal corresponds to our `VBF` while their (data-driven) background corresponds to our `QCD`.

	`VBF`	ATLAS signal	`QCD`	ATLAS data sidebands
after pre-selection	755.8	930.9	1,683,155	2,584,704

Table 15: Event yields from our simulation for `VBF` and `QCD` and expected event yields from [5], at $\sqrt{s} = 13$ TeV with an integrated luminosity of 126 fb^{-1}.

It is expected that our expected number of events is lower than those from ATLAS because we only generate events at leading order. Higher-order corrections can account for this difference. In VBF the k-factor at next-to-leading order is known to be ≈ 1.1 [225]. The ratio between the ATLAS event yield and ours is about 1.2. We apply an effective k-factor of 1.2 to our `VBF` and `BSM` samples. In our `QCD` we use an effective k-factor of 1.5 which makes our results consistent with the ATLAS event yield.

5.3.2 Event Selection

In addition to the above pre-selection, we require the events to satisfy following selections which are based on the characteristics of our `BSM` signal, inspired by [197], but tailored to our final state.

Since the VBF signal features a wide rapidity gap between the two tagging jets, events with large separation in pseudorapidity are selected for

$$\Delta\eta(j_1, j_2) > 3. \tag{5.6}$$

The two tagging jets tend to be in the forward and backward region, so we require them to be in the opposite directions relative to the beam axis

$$\eta(j_1) \cdot \eta(j_2) < 0. \tag{5.7}$$

Due to this back-to-back nature, the two tagging jets also tend to have large invariant mass. So we select events with

$$m(j_1, j_2) > 600 \text{ GeV}. \tag{5.8}$$

To limit additional emissions, we demand the minimum angular separation between any b-jet and any tagging jet to be

$$\Delta R_{\min}(b_i, j_k) > 1.5, \qquad i, k = 1, 2. \tag{5.9}$$

Furthermore, we make use of the azimuthal angular separation between the b-jet pair and the tagging jet pair, and we require

$$\Delta\Phi(b_1 b_2, j_1 j_2) > 1.5, \tag{5.10}$$

where $\Delta\Phi(b_1 b_2, j_1 j_2)$ is the difference in azimuthal angle between the $b_1 b_2$ system and the $j_1 j_2$ system.

Since the QCD background tends to have jets with a relatively large azimuthal angular separation, we select events such that

$$\Delta\Phi(j_1, j_2) < 2. \tag{5.11}$$

In addition, because of the presence of the Higgs boson in the central region, we require it to lie between the two tagging jets

$$y^{min}(j_1, j_2) < y(h) < y^{max}(j_1, j_2), \tag{5.12}$$

where y is the the rapidity of the jet or the reconstructed Higgs boson.

Finally, we cut on the invariant mass of the $b\bar{b}$ system. Due to the mass resolution for $b\bar{b}$, we require a relatively wide mass window around the Higgs boson mass

$$115 \text{ GeV} < m(b_1 b_2) < 135 \text{ GeV}. \tag{5.13}$$

These cuts effectively distinguish `VBF` from `QCD`. Our goal, however, is to identify the contribution of new physics to `BSM` from both `QCD` and from `VBF`.

To distinguish `BSM` from `VBF`, consider Fig. 28 which shows the distribution of the Higgs p_T (after both pre-selection and event selection) with a non-zero value for $c_Q^{(3)}$ (left) and

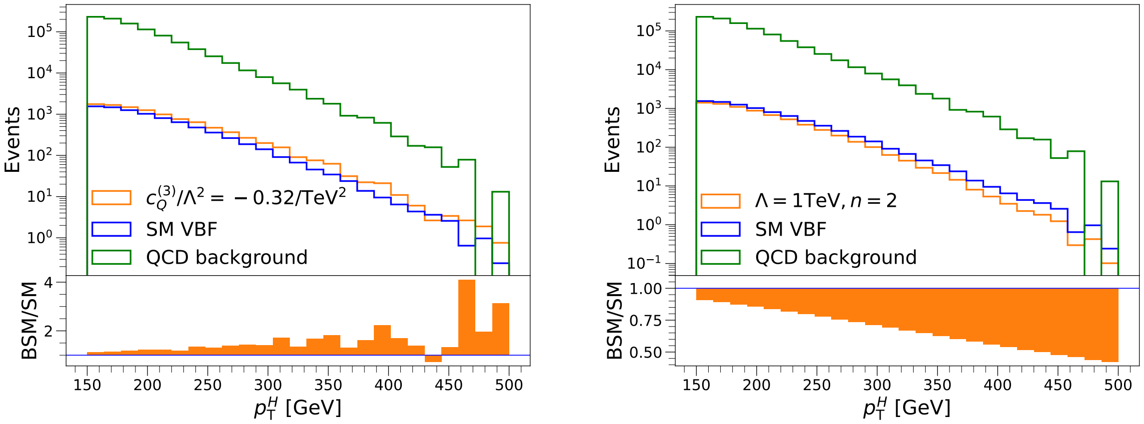

Figure 28: Distribution of the Higgs p_T in `QCD`, `VBF`, and `BSM`. On the left, $c_Q^{(3)}/\Lambda^2$ is set to -0.32 TeV^2, while on the right, a form factor with $n = 2$ and a scale $\Lambda = 1$ TeV is used.

including the form factor (right). We see that this is a powerful discriminant to separate our signal from the backgrounds. Note that new physics can cause an increase or decrease in the number of expected events because the leading effect is the interference between new physics and the SM.

As discussed in Sec. 5.2, there are other variables that are strongly correlated with the Higgs p_T, such as the sum of the two tagging jets.

5.4 Results

To derive the sensitivity to new physics scale at the LHC, we adopt the usual statistical significance,

$$\frac{S}{\sqrt{B}} = \frac{|N_{\mathtt{BSM}} - N_{\mathtt{VBF}}|}{\sqrt{N_{\mathtt{VBF}} + N_{\mathtt{QCD}}}}, \tag{5.14}$$

where $N_i = \mathcal{L} \cdot \sigma_i$ denote the expected numbers of events after event selections at luminosity $\mathcal{L}$ for sample $i = \{\mathtt{BSM}, \mathtt{VBF}, \mathtt{QCD}\}$.

The contribution of new physics can result in either an enhancement or a suppression relative to the SM VBF yield. In particular, the form factor causes a suppression in the signal where the effect becomes more prominent when Λ is small. The effect of the dimension-6 operators depends on the size of the Wilson coefficient and the sign of the interference with the SM. In the case that $N_{\texttt{BSM}}$ is less than $N_{\texttt{VBF}}$, we take the absolute value to ensure a positive significance.

In Fig. 29, we show how selecting different observables at different thresholds affects the significance achieved at high luminosity LHC (assuming $\mathcal{L} = 3\ \text{ab}^{-1}$), in two benchmark scenarios.

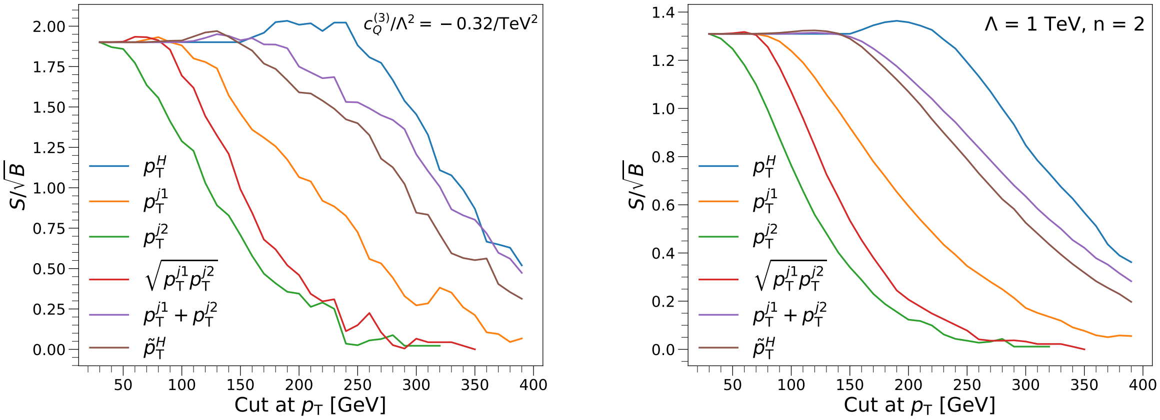

Figure 29: Search significance as a function of cut on Higgs p_T-like variable for coefficient $c_Q^{(3)}$ (left) and for the $n = 2$ form factor (right). Variables used are described in Sec. 5.2.

We find the transverse momentum of the Higgs boson to be the most powerful observable to distinguish new physics from SM, as we discussed in Sec. 5.3. The other variables we consider, in decreasing order of search sensitivity, are $p_T^{j_1} + p_T^{j_2}$, $\tilde{p}_T^h$ (see Eq. (5.5)), $p_T^{j_1}$, $\sqrt{p_T^{j_1} p_T^{j_2}}$, and $p_T^{j_2}$. The tagging jets, in particular the leading jet, can be useful to probe the high momentum-exchange region of VBF. The subleading jet alone, however, does not correlate strongly with the Higgs p_T and is less useful.

Consequently, to compute the new physics reach, we use p_T^h as the final discriminant and select the threshold that optimizes the significance. The corresponding 1σ and 2σ constraints on the dimension-6 operators are shown in Fig. 30.

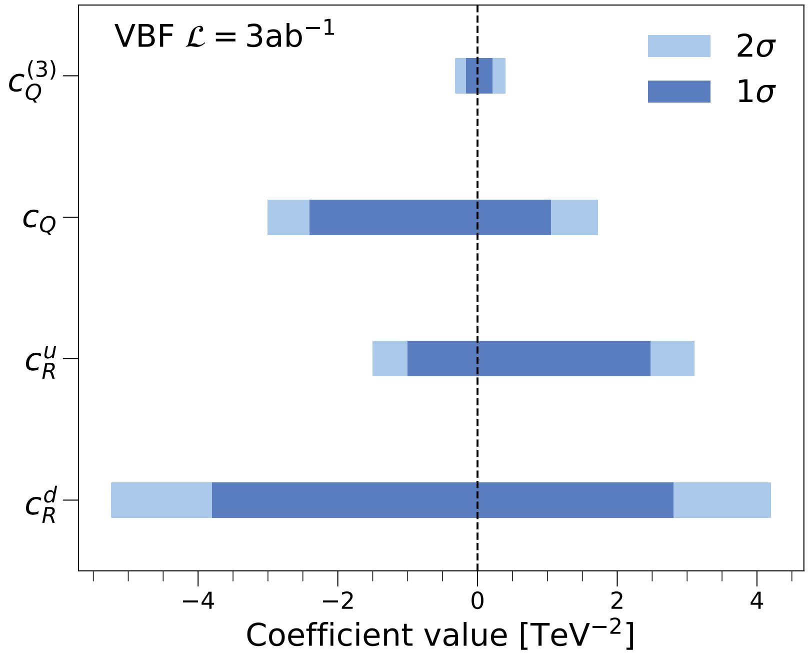

Figure 30: Limits on Wilson coefficients of dimension-6 operators with an integrated luminosity of 3 ab^{-1}.

The 95% C.L. limits are given numerically in Tab. 16. In the top row, we give the limits on c_i/Λ^2 for each operator, one at a time. The VBF search is most sensitive to the $\mathcal{O}_Q^{(3)}$ operator, as expected [197]. Fixing $c_i = \pm 1$ allows us to translate the bound into a limit on the scale Λ which we show in the middle and bottom rows of the table.

	$c_Q^{(3)}$	$c_Q^{(1)}$	c_u	c_d
$c_i/\Lambda^2[\text{TeV}^{-2}]$	[-0.32, 0.40]	[-3, 1.72]	[-1.5, 3.1]	[-5.24, 4.20]
Λ [TeV] ($c_i = +1$)	1.6	0.76	0.57	0.49
Λ [TeV] ($c_i = -1$)	1.8	0.58	0.82	0.44

Table 16: Dimension-6 results at 95% C.L. with an integrated luminosity of 3 ab^{-1}.

Figure 31 shows the search significance as a function of Λ for the form factor, Eq. (5.4), with $n = 2$ and $n = 3$. Since $n = 3$ has a steeper suppression than $n = 2$ the significance for fixed Λ is larger. The 95% C.L. limits are 0.8 TeV and 1 TeV.

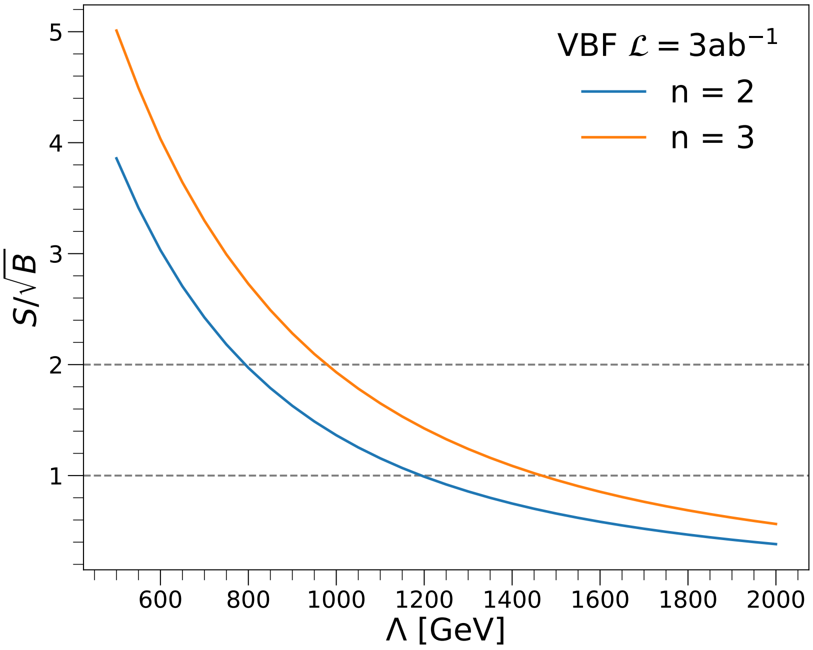

Figure 31: Search significance as a function of the scale Λ for the form factor Eq. (5.4) for $n = 2$ (blue) and for $n = 3$ (orange). An integrated luminosity of 3 ab^{-1} is used.

Finally, we summarize all new physics results together in Fig. 32.

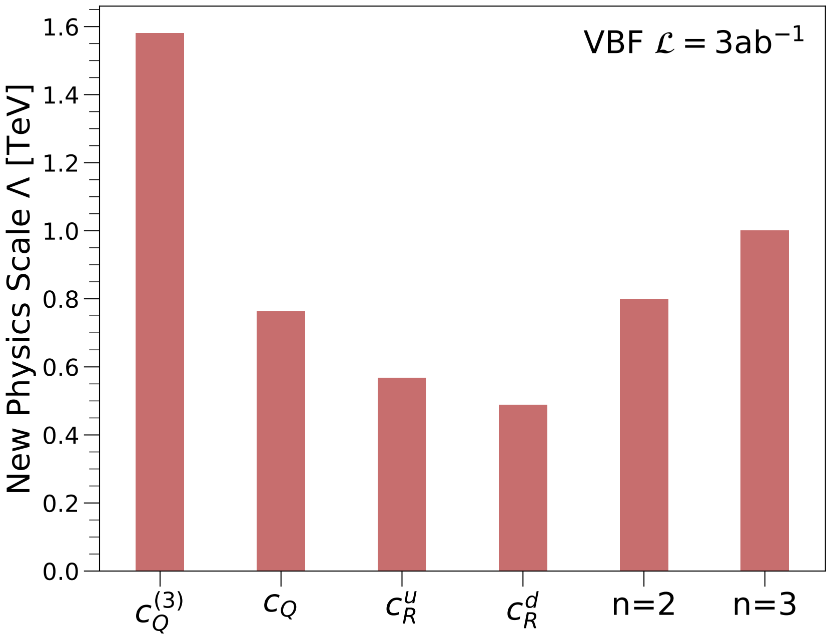

Figure 32: Limits on the scale of new physics Λ at 95% C.L. for dimension-6 operators (assuming positive coefficients) and the form factor with $n = 2$ and $n = 3$ with an integrated luminosity of 3 ab^{-1}.

6.0 Conclusions

Precision measurements of Higgs couplings at high energy scale is of vital importance in today's particle physics research. Any deviation of Higgs couplings from the SM values could be a gateway to possible new physics. We studied the rare Higgs boson decay into charm quarks with a new approach in chapter 2. In chapters 3 and 4, the phenomenology of $Ht\bar{t}$ coupling at TeV scale were studied in details, which highlight the Higgs couplings in time-like domain and space-like domain respectively. At last, chapter 5 features probing HVV coupling at high transverse momentum regime.

In chapter 2, we first reviewed the existing searches at the LHC and obtained the projection at the HL-LHC in probing the charm-Yukawa coupling, as summarized in Table 6. We proposed to study a new channel: the Higgs boson production via the VBF mechanism plus an additional hard photon in the hope to observe the challenging decay mode $H \to c\bar{c}$. The additional photon helps for the trigger to this hadronic decay process and to suppress gluon-rich QCD multi-jet background. The search that we proposed can utilize existing ATLAS and CMS triggers or offer new opportunities, for instance utilizing charm tagging in the HLT. We presented our specific proposal for the trigger design in Sec. 2.1. Based on the trigger considerations and the kinematic features of the signal, we first performed a cut-based analysis in Sec. 2.2.1, which yielded a sensitivity for signal strength μ of about 43 times the SM value at 95% CL_s at the HL-LHC. A boosted decision tree described in Sec. 2.2.2 enhanced the sensitivity by roughly 30% (using the same definition of relative change as used in Sec. 2.2.2), to about 29 times the SM value at 95% CL_s at HL-LHC, corresponding to an upper limit of y_c as 13 times the SM value. Our obtained constraint on charm-Yukawa coupling, summarized in Table 10, is better than the $H \to J/\psi + \gamma$ channel [57]. Even though the limit obtained in our analyses is slightly weaker than the ZH direct search by ATLAS [45], our channel will provide complementary information and a combination of different search channels can further improve the limit. Global analyses of all the Higgs couplings [53, 61, 62, 63] could result in a more sensitive probe than the direct search result $H \to c\bar{c}$, but admittedly depending on model-dependent assumptions, such as

$|\kappa_V| \leq 1$ etc. Direct measurements of charm-Yukawa coupling are nevertheless indispensable. Finally, we provided the first investigation of the VBF cross section with an associated photon at higher collider energies of 30 TeV and 100 TeV. Assuming the same signal and background acceptance as well as the similar detector performance, some improvement of the sensitivity would be anticipated, as shown in Table 10. As we are entering the new phase of the LHC mission, it is important to push for the challenging measurements and to fully realize the potential for discovery at both the energy frontier and the precision frontier.

In chapter 3, we have systematically studied the off-shell Higgs production in the $pp \to H^* \to Z(\ell\ell)Z(\nu\nu)$ channel at the high-luminosity LHC. We showed that this signature is crucial to probe the Higgs couplings across different energy scales potentially shedding light on new physics at the ultraviolet regime. To illustrate its physics potential, we derived the LHC sensitivity to three BSM benchmark scenarios where the new physics effects are parametrized in terms of the Higgs boson width, the effective field theory framework, and a non-local Higgs-top coupling form factor. The combination of a large signal rate and a precise phenomenological probe for the process energy scale, due to the transverse ZZ mass, renders strong limits for all considered BSM scenarios. A summary table and comparison with the existing results in the literature are provided in Table 12. Adopting Machine-learning techniques, we demonstrated in the form of BDT that the HL-LHC, with $\mathcal{L} = 3$ ab^{-1} of data, will display large sensitivity to the Higgs boson width, $\Gamma_H/\Gamma_H^{SM} < 1.31$. Our work is recognized and cited by a recent paper from the ATLAS collaboration on the off-shell Higgs boson production and constraint on the Higgs total width [226]. In addition, the characteristic high energy behavior for the new physics terms within the EFT framework results in relevant bounds on the (κ_t, κ_g) new physics parameters, resolving the low energy degeneracy in the gluon fusion Higgs production. In particular, we observe that the LHC can bound the top Yukawa within $\kappa_t \approx [0.4, 1.1]$ at 95% CL. The upper bound on κ_t is complementary to the direct Yukawa measurement via ttH and can be further improved in conjunction with additional relevant off-shell Higgs channels. Finally, when considering a more general hypothesis that features a non-local momentum-dependent Higgs-top interaction, we obtain that the HL-LHC is sensitive to new physics effects at large energies with $\Lambda = 1.5$ TeV for $n = 2$ and $\Lambda = 2.1$ TeV for $n = 3$ at 95% CL. We conclude that, utilizing the promising $H^* \to Z(\ell^+\ell^-)Z(\nu\bar{\nu})$ channel at the HL-LHC and adopting the Machine-Learning techniques, the combination of a large signal rate and a precise phenomenological probe for the process energy scale renders improved sensitivities beyond the existing literature, to all the three BSM scenarios considered in this work.

In chapter 4, we studied the prospects to **directly** probe the Higgs-top coupling for new physics at high energy scales using the $pp \to t\bar{t}h$ process at the HL-LHC. We considered two beyond the SM scenarios, namely the SMEFT framework and a general Higgs-top form-factor, as discussed in Sec. 4.1. We presented in Sec. 4.2 the general phenomenological effects for these new physics contributions, showing that they could produce augmented new physics effects at high energy scales. Focusing on the boosted Higgs regime in association with jet substructure techniques, we explored the largest Higgs branching fraction $h \to b\bar{b}$ along with the clean leptonic top-quark decays. The BSM effects were constrained through a shape analysis on the p_{Th} spectrum. We observed the potential sensitivity at the TeV-scale for new physics both in the EFT and form-factor scenarios. The chromomagnetic dipole operator was probed up to $\Lambda/\sqrt{c_{tG}} \approx 2.9$ TeV and the $\mathcal{O}_{t\phi}$ operator to $\Lambda/\sqrt{c_{t\phi}} \approx 1.0$ TeV, as shown in Sec. 4.2.1. The limits presented sub-leading differences between the linear and quadratic c_i/Λ^2 expansion, indicating that our phenomenological study satisfies the EFT expansion. Finally, when considering a more general Higgs-top quark form-factor in Sec. 4.2.2, we concluded that the HL-LHC is sensitive to new physics up to the scale $\Lambda =$ 2.1 TeV for $n = 2$ and 2.7 TeV for $n = 3$ at 95% CL. Further details are summarized in Table 14. The $t\bar{t}h$ studies at high scales, which **directly** explore the Higgs-top Yukawa interaction, results in a competitive and complementary pathway for BSM sensitivity in comparison to the off-shell Higgs channels and the current ATLAS and CMS limits. Some improvements in sensitivity can be anticipated by including other modes, such as $t\bar{t}(h \to \gamma\gamma)$, which would yield a cleaner signal but a lower rate [227]. In addition, we can increase our present $t\bar{t}(h \to b\bar{b})$ statistical sample by about a factor of six, if we include one leptonic decay plus one hadronic decay of the $t\bar{t}$. The analysis, however, would be more complex, with significantly larger QCD backgrounds [228]. Finally, while we adopt `MadGraph5_aMC@NLO` as our general Monte Carlo generator (that accounts for the signal EFT contributions at NLO QCD), we acknowledge some other recent important developments associated with the

$t\bar{t}b\bar{b}$ background [229, 230, 231]. We leave those improvements to future work with realistic simulations.

In chapter 5, we study the phase space region of VBF where the Higgs p_T is large. In this region, there is sensitivity to new physics coming from high scales. We study the impact of both dimension-6 operators and a nuclear-physics-inspired form factor. We explore the $h(b\bar{b})jj$ channel where the Higgs decays on-shell to $b\bar{b}$. The main backgrounds are the SM contribution to VBF and QCD where the $b\bar{b}$ is from the splitting of a gluon. For dimension-6 operators, the reach for new physics is up to 1.8 TeV at 95% C.L. This reach is weaker than previous searches in the $\gamma\gamma$ and $\tau^+\tau^-$ channels where the decrease is due to the much larger backgrounds in the $b\bar{b}$ channel. Ultimately to maximize our reach for new physics the next step would be to combine all existing channels. Additionally, it would be useful to include additional decay channels of the Higgs such as $W(\ell\nu)W(\ell\nu)$. As we have discussed, for such a channel with invisible particles, one can cut on $p_T(j_1) + p_T(j_2)$, since $p_T(h)$ would be unavailable, and maintain sensitivity to the high momentum exchange region of phase space. With enough data, it would also be interesting to do a simultaneous fit to VBF and diboson data to better characterize the full space of high energy primary operators.

The discovery of the Higgs boson is a major triumph in particle physics, confirming the existence of the Higgs field and its unique role in electroweak symmetry breaking. Since its discovery, the Higgs boson has been a powerful tool to understand the Standard Model and probe physics beyond it. By studying its properties, we can gain direct insight into the physics landscape beyond the weak scale. So far, the LHC has only collected approximately 5% of its projected full dataset. Important upgrades are currently underway to prepare for its high luminosity phase. With larger datasets to be collected during Run 3 and ultimately at the High Luminosity LHC, we will have even greater opportunities to make fundamental and challenging measurements, and I believe the Higgs boson will be the lamppost to the next discovery.

Appendix A Statistical Methods

Statistical methods are a crucial aspect of particle physics experiments, as we often use statistical significance to determine whether the observed data are consistent with the predictions of a given theory or if they suggest the presence of new phenomena. It is important to evaluate and interpret experimental results to ensure that any observed signals are real and not just random fluctuations in the background. In this appendix, I present the statistical methods used throughout this thesis to characterize the sensitivity to a certain physics signal.

A.1 Gaussian Statistics

In an experiment, the result usually consists of an observed number of events n. This random variable can be modeled by a Poisson distribution with a mean of $\mu s + b$, where s and b are the expected numbers of events of the signal and background processes, given by our theory. We are interested in the discovery significance expected under the assumption of $\mu = 1$. In the limit of large numbers of events, the mentioned Poisson distribution can be approximated as a Gaussian distribution with a mean of $\mu s + b$ and standard deviation of $\sqrt{\mu s + b}$. The p-value of the background-only hypothesis is the probability of finding n greater than or equal to the numer observed:

$$p = \Phi(\frac{n-b}{\sqrt{b}}), \tag{A.1}$$

where Φ is the cumulative distribution function (CDF) of the standard Gaussian distribution. The corresponding significance is then

$$Z = \Phi^{-1}(1-p) = \frac{n-b}{\sqrt{b}}, \tag{A.2}$$

where Φ^{-1} is the quantile function of the standard Gaussian distribution. Assuming $\mu = 1$, then the median of n is equal to $s + b$, thus the significance of discovery is

$$Z = \frac{s}{\sqrt{b}}. \tag{A.3}$$

We adopted this definition to quantify our sensitivity to the signal processes in chapter 2 and 5.

A.2 Binned Log-likelihood

In chapters 3 and 4, we use a more sophisticated method called binned log-likelihood analysis to derive sensitivity to new physics scale. First, we construct the likelihood function which is the product or Poisson probabilities for all bin:

$$L(\mu, \theta) = \prod_{i=1}^{N} \frac{(\mu s_i + b_i)^{n_i}}{n_i!} e^{-(\mu s_i + b_i)}, \tag{A.4}$$

where n_i is the observed number of events in i-th bin, while s_i and b_i are are expected number of events for signal and background in i-th bin. The expected number of events is simply scaled by luminosity $\mathcal{L}$ as

$$s_i = \mathcal{L} \cdot \sigma_i^s, \tag{A.5}$$

$$b_i = \mathcal{L} \cdot \sigma_i^b, \tag{A.6}$$

where σ_i^s and σ_i^b are differential cross-sections in i-th bin for signal and background respectively. The profile likelihood ratio is defined as

$$\lambda(\mu) = \frac{L(\mu, \hat{\hat{\theta}})}{L(\hat{\mu}, \hat{\theta})}, \tag{A.7}$$

where the denominator is the global maximum of likelihood L and θ denotes any nuisance parameters which are not relevant in our case. Then naturally the log-likelihood ratio would be

$$-2 \ln \lambda(\mu) = -2 \ln L(\mu, \hat{\hat{\theta}}) + 2L(\hat{\mu}, \hat{\theta}). \tag{A.8}$$

The test statistic for discovery of a positive signal is defined as

$$q_0 = \begin{cases} -2\ln\lambda(0) & \text{for} \quad \hat{\mu} \geq 0 \\ 0 & \text{for} \quad \hat{\mu} < 0 \end{cases} \tag{A.9}$$

In order to find q_0, we assume the observed number of events is given by BSM, namely $n_i = s_i + b_i$. As a result, the global maximum of likelihood function corresponds to $\hat{\mu} = 1$. Therefore we have

$$-2\ln L_{max} = -2\sum_{i=1}^{N} n_i \ln(s_i + b_i) - (s_i + b_i) - \ln(n_i!). \tag{A.10}$$

By Stirling approximation $\ln n! \approx n\ln n - n$, we can easily see that Eq. A.10 vanishes. Therefore, the only contribution to q_0 is

$$q_0 = -2\ln L(\mu = 0) = -2\sum_{i=1}^{N}(s_i + b_i)\ln\frac{b_i}{s_i + b_i} + s_i. \tag{A.11}$$

The discovery significance is then

$$Z = \sqrt{q_0} = \sqrt{2\sum_{i=1}^{N}(s_i + b_i)\ln(1 + \frac{s_i}{b_i}) - s_i}. \tag{A.12}$$

Appendix B Parton Level Analysis of VBF+γ with $h \to b\bar{b}$

In chapter 2, we presented a new approach to probe the decay of Higgs boson into a pair of charm quarks in the vector boson fusion (VBF) production with a photon radiation. This channel can also be utilized to study Higgs boson decay to a pair of bottom quarks [96, 97]. In parallel to the analysis detailed in chapter 2, we also did a parton-level analysis of $h \to b\bar{b}$ in VBF with a photon.

The calculation of vector boson fusion as a main production mechanism of the Higgs boson is well-known, while VBF+γ is less studied. To validate our calculation set-up, we first followed the LHC Higgs Cross Section Working Group [1] to calculate the differential distributions of four observables in VBF ($pp \to hjj$): transverse momentum of the Higgs boson p_T^H, the transverse momentum of the leading and sub-leading VBF jets $p_T^{j_{1,2}}$ and the invariant mass of the VBF jet pair M_{jj}, with the following cuts

$$\begin{aligned} p_T^j > 20\text{GeV}, \quad |\eta^j| < 5, \\ |\Delta\eta_{jj}| > 3, \quad M_{jj} > 130\text{GeV}. \end{aligned} \tag{B.1}$$

Results are shown in Fig. 33 in red. Our calculations are found to agree with the LHC Higgs Cross Section Working Group within 10%. We proceeded with the same set-up to calculate our desired signal $pp \to hjj\gamma$, with the following requirements on the photon

$$p_T^\gamma > 30\text{GeV}, \quad |\eta^\gamma| < 1.37 \text{ or } 1.52 < |\eta^\gamma| < 2.37. \tag{B.2}$$

The resulting differential distributions are shown in Fig. 33 in blue. As expected, the kinematics of vector boson fusion with a photon radiation are very similar to VBF, but with an event rate of roughly two orders of magnitude less due to the small electromagnetic coupling. This is a trade-off for two advantages of this channel: (i) the additional photon gives us an extra handle to trigger on, improving the trigger efficiencies; (ii) the extra photon also helps suppress the huge QCD backgrounds.

After validating and establishing the calculation set-up, we investigated the decay of the Higgs boson into a pair of bottom quarks in $pp \to hjj\gamma$, which is our signal process.

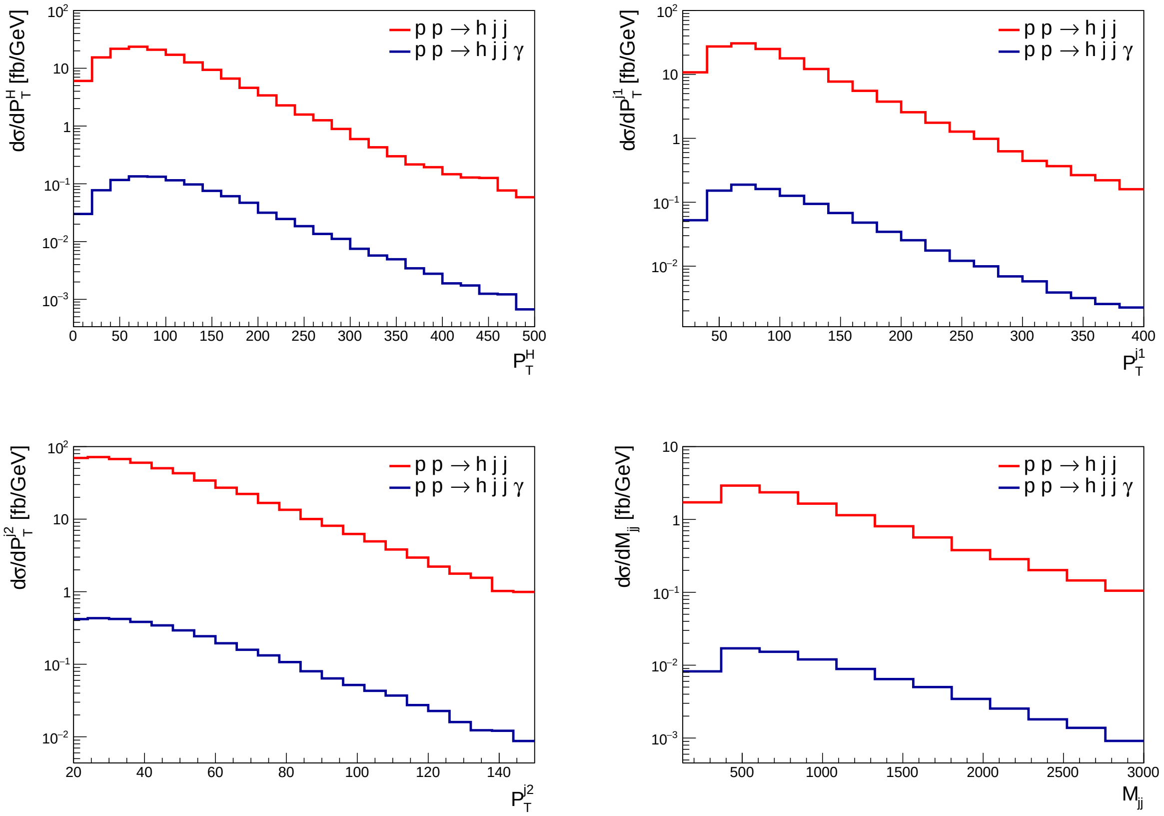

Figure 33: Differential distributions of transverse momentum of the Higgs boson, leading and sub-leading VBF jets as well as invariant mass of the VBF jets at $\sqrt{s} = 13$ TeV.

The dominant background is QCD multijet background $pp \to bbjj\gamma$, calculated with the same set-up. To identify the signal from the background processes, we start with a series of pre-selections, followed from [96]. We require that in the final states there is one photon satisfying

$$p_{\mathrm{T}}^{\gamma} > 30 \text{ GeV}, \quad |\eta^{\gamma}| < 1.37 \ \text{ or } \ 1.52 < |\eta^{\gamma}| < 2.37. \tag{B.3}$$

Events are required to have 4 jets with

$$p_{\mathrm{T}}^{j} > 40 \text{ GeV} \ \text{ and } \ |\eta^{j}| < 4.4. \tag{B.4}$$

At least 2 jets in the central region $|\eta^j| < 2.5$ are required to be b-tagged at 77% efficiency working point. The two highest-p_{T} b-tagged jets are identified as signal jets from the Higgs boson decay while the remaining jets are identified as the VBF jets. The VBF jet pair is required to have high invariant mass

$$M_{jj} > 800\text{GeV}. \tag{B.5}$$

In addition, the signal b-jet pair is required to have $p_{\mathrm{T}}^{bb} > 80$ GeV to remove potential bias in m_{bb} distribution.

To fully utilize the available range of kinematic features, we opt to incorporate several additional kinematic observables that effectively distinguish between signal and background. The distributions of these observables, after applying pre-selections, are illustrated in Fig. 34 and 35. Apart from the pre-selections, we make prudent cuts based on signal kinematics

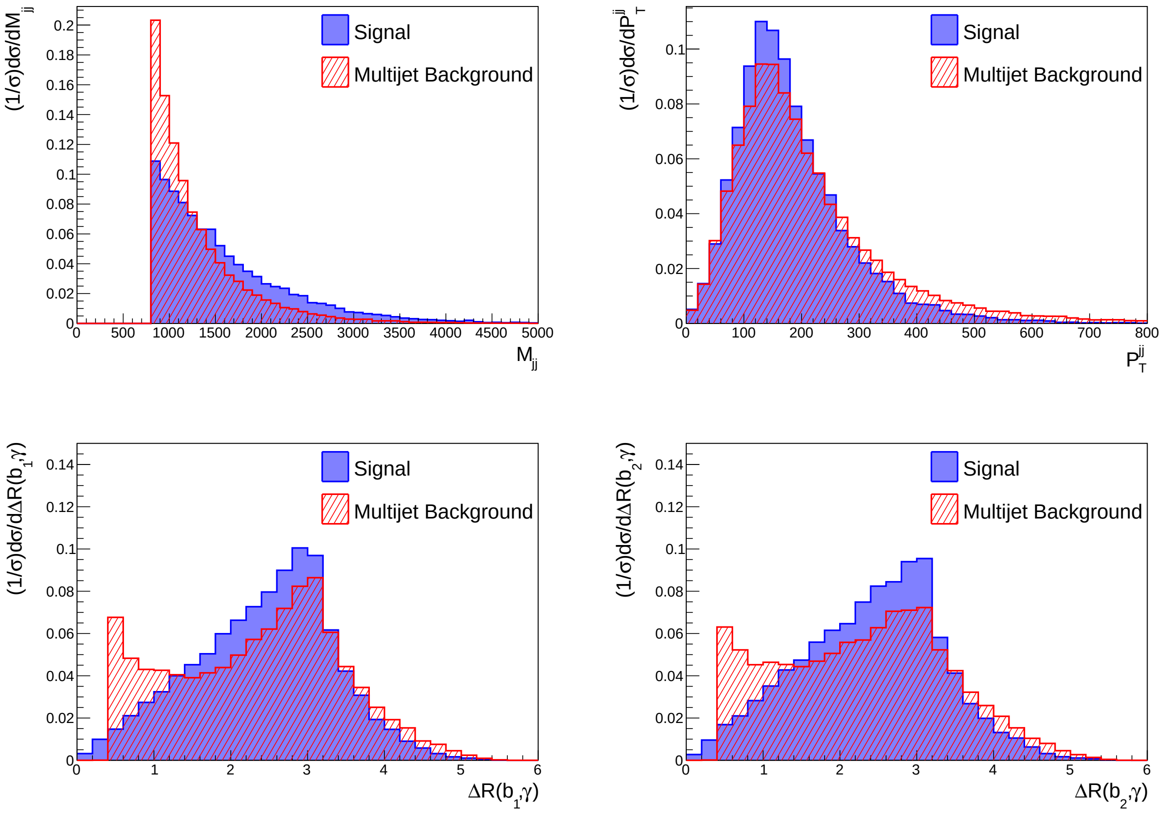

Figure 34: Distributions of useful observables for signal (blue) and multi-jet background (red) after pre-selections.

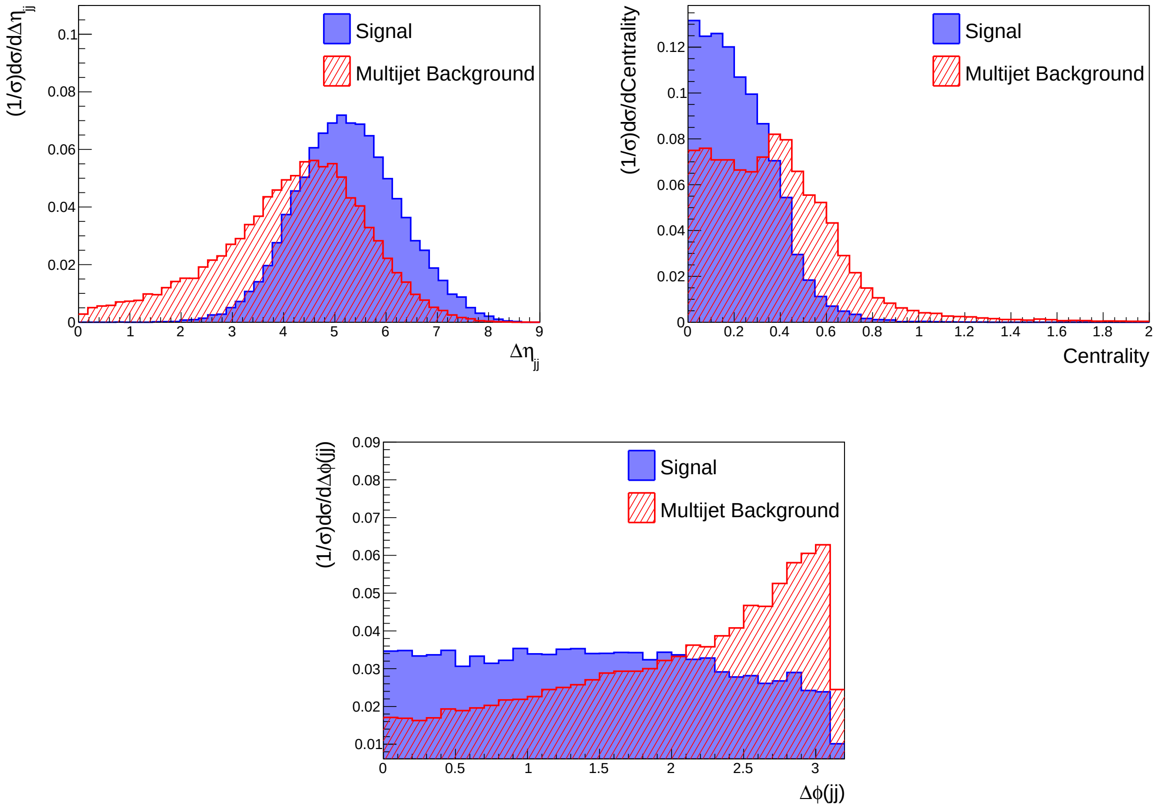

Figure 35: Distributions of useful observables for signal (blue) and multi-jet background (red) after pre-selections.

to further refine our analysis. The invariant mass of the VBF jets tends to be large, so we require

$$M_{jj} > 1300\,\text{GeV}. \tag{B.6}$$

The transverse momentum of the VBF jet pair is governed by the W/Z exchange and thus relatively low, so we demand

$$p_{\text{T}}^{jj} = |\vec{p}_{\text{T}}^{\,j_1} + \vec{p}_{\text{T}}^{\,j_2}| < 300\,\text{GeV}. \tag{B.7}$$

Moreover, as the VBF signal exhibits a significant rapidity gap between the two forward-backward jets, events with substantial pseudo-rapidity separation between the two jets are chosen for

$$\Delta\eta_{jj} = |\eta_{j_1} - \eta_{j_2}| > 4. \tag{B.8}$$

In our signal process, the photon does not radiate from b-jets from Higgs decay. Therefore, the angular separation between the signal b-jets and the photon tends to be larger, which distinguishes it from the QCD background. As a result, we require

$$\Delta R(b_{1,2}, \gamma) > 1.2, \tag{B.9}$$

where $b_{1,2}$ are leading and sub-leading b-jets. We also make use of the centrality of the photon relative to the VBF jets and require

$$\text{centrality} = |\frac{y_\gamma - \frac{y_{j1}+y_{j2}}{2}}{y_{j1} - y_{j2}}| < 0.35, \tag{B.10}$$

where y is the rapidity of the jet or photon. Additionally, we utilize the azimuthal angular information on the transverse plane and require

$$\Delta\phi(jj) < 2 \tag{B.11}$$

The invariant mass of the signal b-jet pair m_{bb} is the most powerful discriminant. Due to finite jet-mass resolution, we expect a relatively wide mass window and therefore require the invariant mass of the b-jet pair to be within

$$100 \text{ GeV} < m_{bb} < 140 \text{ GeV}. \tag{B.12}$$

It should be noted that at parton level, the mass resolution of the signal is infinitely good so the result would be towards the optimistic side. Nevertheless, the physics essence of these selections still applies. The expected numbers of events from signal and background of integrated luminosity 3 ab^{-1} are shown in Table 17.

	Signal	Background
Pre-selections	3117	1.3×10^6
Optimized selections	643	5.3×10^4
100 GeV $< m_{cc} <$ 140 GeV	643	5878
$S/\sqrt{B}$	8.4	

Table 17: Expected yields of signal and multi-jet background at the HL-LHC with 3 ab^{-1} from a cut-based analysis.

Appendix C Generator-Level Cuts in VBF kinematics

In chapter 5, our dominant background is QCD multijet background which is known to be challenging in simulation. Therefore, to enhance the efficiency of event generation, we applied the following cuts at the generator-level. In each sample the final state at parton-level includes two b-quarks and two light flavor quarks. The b-quarks are labelled as b_1 and b_2, in descending order of p_T, while the light flavor quarks are labelled as j_1 and j_2 following the same scheme.

- $p_T(j_1) > 40$ GeV, $p_T(j_2) > 10$ GeV.
- $p_T(b_1) > 65$ GeV, $p_T(b_2) > 45$ GeV.
- $3 < |\eta(j_1)| < 5$, $|\eta(j_2)| < 5$, $|\eta(b_1)| < 3$, $|\eta(b_2)| < 3$
- $|\eta(j_1) - \eta(j_2)| > 2.5$.
- $\Delta R(j_1, j_2) > 0.4$, $\Delta R(b_1, b_2) > 0.4$, $\Delta R(b, j) > 0.4$, where $\Delta R(b, j)$ refers to any pair of b-quark and light flavor quark and $\Delta R(a, b) = \sqrt{(\eta(a) - \eta(b))^2 + (\phi(a) - \phi(b))^2}$.
- $p_T(bb) > 120$ GeV, where $p_T(bb)$ is the transverse momentum of the $b\bar{b}$ system.
- $m(jj) > 550$ GeV where $m(jj)$ is the invariant mass of the dijet system.
- 110 GeV $< m(bb) <$ 140 GeV, where $m(bb)$ is the invariant mass of the $b\bar{b}$ system.

Already with these generator-level cuts, the impact of dimension-6 is observable. Figure 36 shows the cross section of `BSM` where the coefficient of a single dimension-6 operator coefficient is varied.

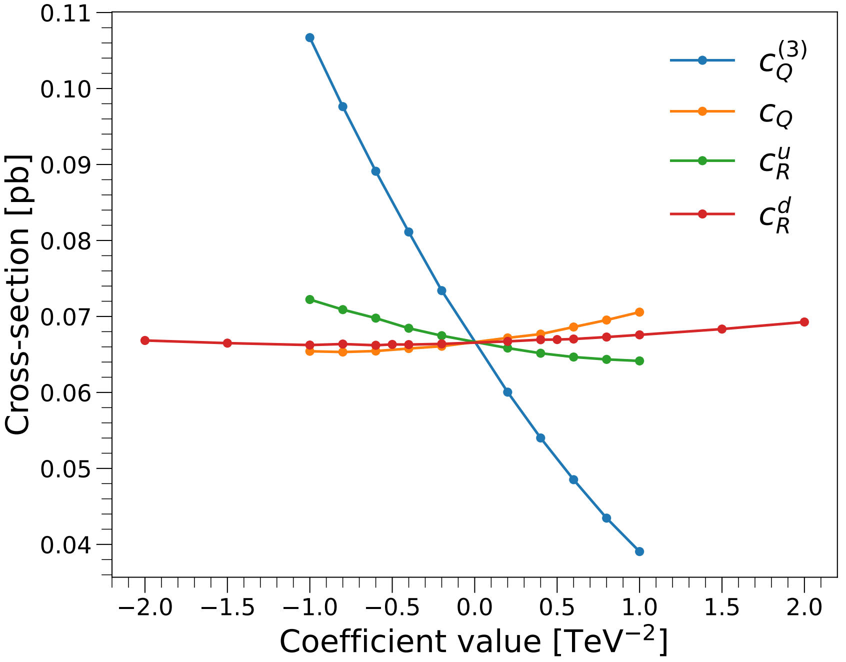

Figure 36: Cross section for `BSM` sample where the coefficient of a single operator is varied.

Appendix D Contribution from $\mathcal{O}_{\phi W}$ to VBF channel

In chapter 5, we focused on four dimension-6 operators that contribute to the vector boson fusion processes. Their effect is to induce new interactions of our interest $q\bar{q}VH$. Operators that modify the existing vertex such as hVV vertex can also contribute. In addition to the operators discussed in chapter 5, we also investigate the effect of operator $\mathcal{O}_{\phi W}$ which defined as

$$\mathcal{O}_{\phi W} = (\phi^\dagger \phi - \frac{v^2}{2}) W_I^{\mu\nu} W^I_{\mu\nu}. \tag{D.1}$$

In Fig. 37, we show the comparison between operators $\mathcal{O}_{\phi W}$ and $\mathcal{O}_Q^{(3)}$ in the parton-level distributions of four observables: transverse momentum of the Higgs boson p_T^H, the transverse momentum of the leading and sub-leading VBF jets $p_T^{j_{1,2}}$ and the invariant mass of the VBF jet pair M_{jj}, after the following cuts

$$\begin{gathered} p_T^j > 20\text{GeV}, \quad |\eta^j| < 5, \\ |\Delta\eta_{jj}| > 3, \quad M_{jj} > 130\text{GeV}. \end{gathered} \tag{D.2}$$

We can see from the figure that $\mathcal{O}_{\phi W}$ has positive interference with the SM while $\mathcal{O}_Q^{(3)}$ has negative interference. It is noted that at high transverse momentum, especially high p_T^H and $p_T^{j_1}$, positive Wilson coefficient of $\mathcal{O}_Q^{(3)}$ can result in an enhancement despite negative interference. This suggests that at high energy, the quadratic contribution from the operator becomes important and cancels with the linear contribution. It is also important to note that among the four observables, M_{jj} is the least sensitive to new physics effect, while p_T^H is the most sensitive one, $p_T^{j_1}$ is also comparable. The figure also shows that $\mathcal{O}_{\phi W}$ is less sensitive than $\mathcal{O}_Q^{(3)}$. Nevertheless, we derive the constraint for $\mathcal{O}_{\phi W}$ following the same procedure in chapter 5, and we found at 95% C.L.,

$$c_{\phi W}/\Lambda^2 \in [-0.82, 0.57]/\text{TeV}^2. \tag{D.3}$$

Assuming $\mathcal{O}(1)$ Wilson coefficient, this can be translated to bound on new physics scale Λ up to 1.3 TeV.

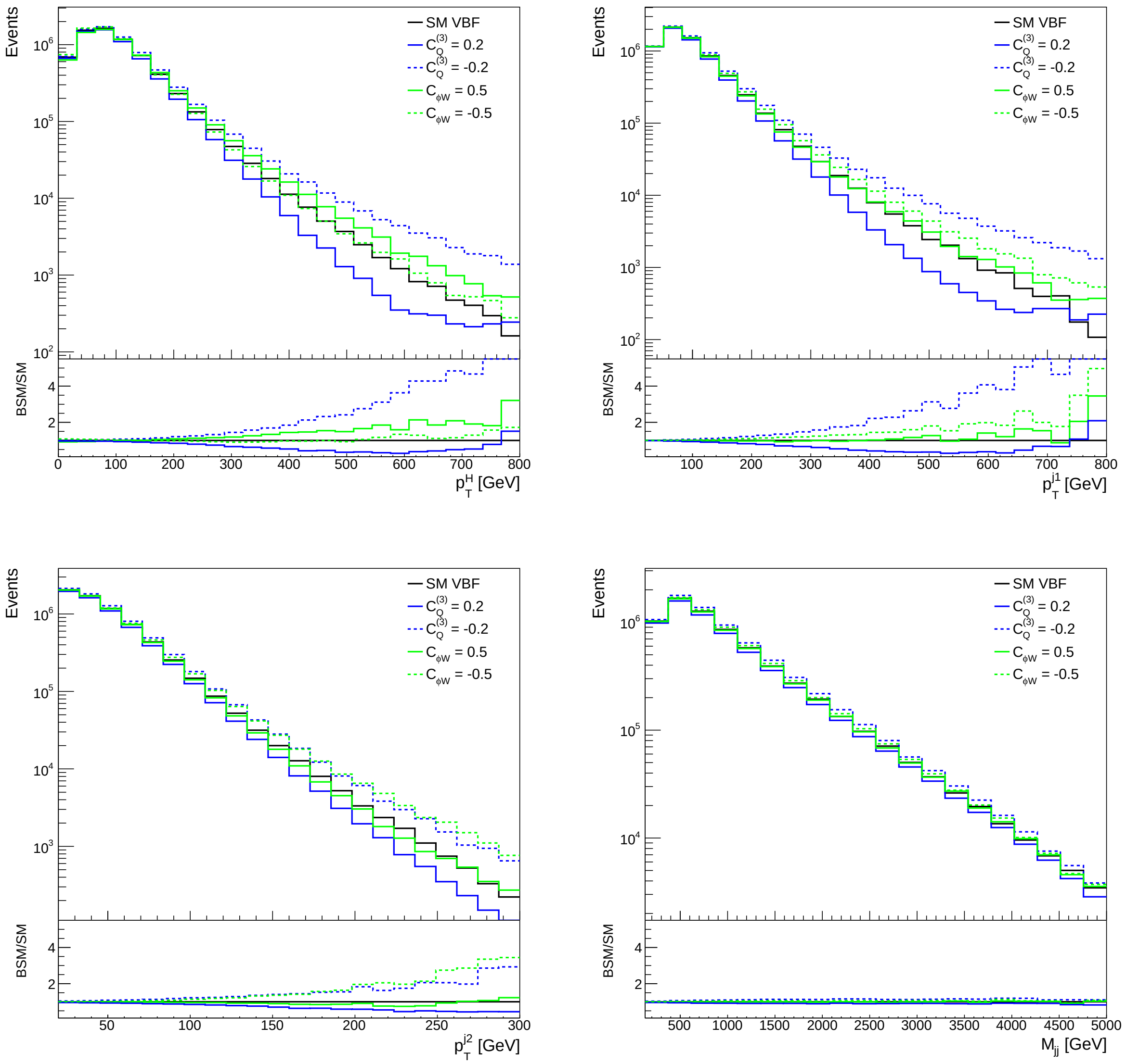

Figure 37: Differential distributions of transverse momentum of the Higgs boson, leading and sub-leading VBF jets as well as invariant mass of the VBF jets.

Bibliography

[1] D. de Florian et al. Handbook of LHC Higgs Cross Sections: 4. Deciphering the Nature of the Higgs Sector. 2/2017, 10 2016.

[2] Geoffrey T. Bodwin, Hee Sok Chung, June-Haak Ee, Jungil Lee, and Frank Petriello. Relativistic corrections to Higgs boson decays to quarkonia. Phys. Rev. D, 90(11):113010, 2014.

[3] Off-shell Higgs boson couplings measurement using $H \to ZZ \to 4l$ events at High Luminosity LHC. 2015.

[4] Sensitivity projections for Higgs boson properties measurements at the HL-LHC. 11 2018.

[5] Georges Aad et al. Measurements of Higgs bosons decaying to bottom quarks from vector boson fusion production with the ATLAS experiment at $\sqrt{s} = 13\,\mathrm{TeV}$. Eur. Phys. J. C, 81(6):537, 2021.

[6] J R Andersen et al. Handbook of LHC Higgs Cross Sections: 3. Higgs Properties. 7 2013.

[7] Georges Aad et al. Observation of a new particle in the search for the Standard Model Higgs boson with the ATLAS detector at the LHC. Phys. Lett. B, 716:1–29, 2012.

[8] Serguei Chatrchyan et al. Observation of a New Boson at a Mass of 125 GeV with the CMS Experiment at the LHC. Phys. Lett. B, 716:30–61, 2012.

[9] Murray Gell-Mann. The Eightfold Way: A Theory of strong interaction symmetry. 3 1961.

[10] G. Zweig. An SU(3) model for strong interaction symmetry and its breaking. Version 1. 1 1964.

[11] S. L. Glashow. Partial Symmetries of Weak Interactions. Nucl. Phys., 22:579–588, 1961.

[12] Steven Weinberg. A Model of Leptons. Phys. Rev. Lett., 19:1264–1266, 1967.

[13] Abdus Salam. Weak and Electromagnetic Interactions. Conf. Proc. C, 680519:367–377, 1968.

[14] Peter W. Higgs. Broken symmetries, massless particles and gauge fields. Phys. Lett., 12:132–133, 1964.

[15] Peter W. Higgs. Broken Symmetries and the Masses of Gauge Bosons. Phys. Rev. Lett., 13:508–509, 1964.

[16] F. Englert and R. Brout. Broken Symmetry and the Mass of Gauge Vector Mesons. Phys. Rev. Lett., 13:321–323, 1964.

[17] R. L. Workman et al. Review of Particle Physics. PTEP, 2022:083C01, 2022.

[18] Measurements of the Higgs boson production and decay rates and constraints on its couplings from a combined ATLAS and CMS analysis of the LHC pp collision data at $\sqrt{s} = 7$ and 8 TeV. 9 2015.

[19] Measurements of the Higgs boson production and decay rates and constraints on its couplings from a combined ATLAS and CMS analysis of the LHC pp collision data at sqrt s = 7 and 8 TeV. 2015.

[20] Morad Aaboud et al. Observation of $H \rightarrow b\bar{b}$ decays and VH production with the ATLAS detector. Phys. Lett. B, 786:59–86, 2018.

[21] A. M. Sirunyan et al. Observation of Higgs boson decay to bottom quarks. Phys. Rev. Lett., 121(12):121801, 2018.

[22] M. Aaboud et al. Observation of Higgs boson production in association with a top quark pair at the LHC with the ATLAS detector. Phys. Lett. B, 784:173–191, 2018.

[23] Albert M Sirunyan et al. Observation of $\mathrm{t\bar{t}H}$ production. Phys. Rev. Lett., 120(23):231801, 2018.

[24] Morad Aaboud et al. Constraints on off-shell Higgs boson production and the Higgs boson total width in $ZZ \rightarrow 4\ell$ and $ZZ \rightarrow 2\ell 2\nu$ final states with the ATLAS detector. Phys. Lett. B, 786:223–244, 2018.

[25] Albert M Sirunyan et al. Measurements of the Higgs boson width and anomalous HVV couplings from on-shell and off-shell production in the four-lepton final state. Phys. Rev. D, 99(11):112003, 2019.

[26] Morad Aaboud et al. Cross-section measurements of the Higgs boson decaying into a pair of τ-leptons in proton-proton collisions at $\sqrt{s} = 13$ TeV with the ATLAS detector. Phys. Rev. D, 99:072001, 2019.

[27] Albert M Sirunyan et al. Observation of the Higgs boson decay to a pair of τ leptons with the CMS detector. Phys. Lett. B, 779:283–316, 2018.

[28] Georges Aad et al. A search for the dimuon decay of the Standard Model Higgs boson with the ATLAS detector. Phys. Lett. B, 812:135980, 2021.

[29] Albert M Sirunyan et al. Evidence for Higgs boson decay to a pair of muons. JHEP, 01:148, 2021.

[30] A. M. Sirunyan et al. Observation of Higgs boson decay to bottom quarks. Phys. Rev. Lett., 121(12):121801, 2018.

[31] Georges Aad et al. Measurements of WH and ZH production in the $H \to b\bar{b}$ decay channel in pp collisions at 13 TeV with the ATLAS detector. Eur. Phys. J. C, 81(2):178, 2021.

[32] M. Aaboud et al. Observation of Higgs boson production in association with a top quark pair at the LHC with the ATLAS detector. Phys. Lett. B, 784:173–191, 2018.

[33] Albert M Sirunyan et al. Observation of $\mathrm{t\bar{t}H}$ production. Phys. Rev. Lett., 120(23):231801, 2018.

[34] Georges Aad et al. Measurements of the Higgs boson production and decay rates and constraints on its couplings from a combined ATLAS and CMS analysis of the LHC pp collision data at $\sqrt{s} = 7$ and 8 TeV. JHEP, 08:045, 2016.

[35] Morad Aaboud et al. Cross-section measurements of the Higgs boson decaying into a pair of τ-leptons in proton-proton collisions at $\sqrt{s} = 13$ TeV with the ATLAS detector. Phys. Rev. D, 99:072001, 2019.

[36] Albert M Sirunyan et al. Observation of the Higgs boson decay to a pair of τ leptons with the CMS detector. Phys. Lett. B, 779:283–316, 2018.

[37] Daniel Egana-Ugrinovic, Samuel Homiller, and Patrick Roddy Meade. Higgs bosons with large couplings to light quarks. Phys. Rev. D, 100(11):115041, 2019.

[38] Shaouly Bar-Shalom and Amarjit Soni. Universally enhanced light-quarks Yukawa couplings paradigm. Phys. Rev. D, 98(5):055001, 2018.

[39] Tao Han and Bob McElrath. $\mathrm{h} \to \mu^+\mu^-$ via gluon fusion at the LHC. Phys. Lett. B, 528:81–85, 2002.

[40] Tilman Plehn and David L. Rainwater. Higgs Decays to Muons in Weak Boson Fusion. Phys. Lett. B, 520:108–114, 2001.

[41] Projections for measurements of Higgs boson cross sections, branching ratios, coupling parameters and mass with the ATLAS detector at the HL-LHC. ATL-PHYS-PUB-2018-054, 2018.

[42] Sensitivity projections for Higgs boson properties measurements at the HL-LHC. CMS-PAS-FTR-18-011, 2018.

[43] Alexandre Alves and Felipe F. Freitas. Towards recognizing the light facet of the Higgs Boson. Mach. Learn. Sci. Tech., 1(4):045025, 2020.

[44] M. Aaboud et al. Search for the Decay of the Higgs Boson to Charm Quarks with the ATLAS Experiment. Phys. Rev. Lett., 120(21):211802, 2018.

[45] Prospects for $H \to c\bar{c}$ using Charm Tagging with the ATLAS Experiment at the HL-LHC. ATL-PHYS-PUB-2018-016, 2018.

[46] Direct constraint on the Higgs-charm coupling from a search for Higgs boson decays to charm quarks with the ATLAS detector. ATLAS-CONF-2021-021, 2021.

[47] Albert M Sirunyan et al. A search for the standard model Higgs boson decaying to charm quarks. JHEP, 03:131, 2020.

[48] Search for $H^0 \to b\bar{b}$ or $c\bar{c}$ in association with a W or Z boson in the forward region of pp collisions. LHCb-CONF-2016-006, 2016.

[49] Roel Aaij et al. Physics case for an LHCb Upgrade II - Opportunities in flavour physics, and beyond, in the HL-LHC era, 2016.

[50] Geoffrey Bodwin, Frank Petriello, Stoyan Stoynev, and Mayda Velasco. Higgs boson decays to quarkonia and the $h\bar{c}c$ coupling. Phys. Rev. D, 88:053003, Sep 2013.

[51] Geoffrey T. Bodwin, Hee Sok Chung, June-Haak Ee, and Jungil Lee. New approach to the resummation of logarithms in Higgs-boson decays to a vector quarkonium plus a photon. Phys. Rev. D, 95(5):054018, 2017.

[52] Gilad Perez, Yotam Soreq, Emmanuel Stamou, and Kohsaku Tobioka. Prospects for measuring the Higgs boson coupling to light quarks. Phys. Rev. D, 93(1):013001, 2016.

[53] Gilad Perez, Yotam Soreq, Emmanuel Stamou, and Kohsaku Tobioka. Constraining the charm Yukawa and Higgs-quark coupling universality. Phys. Rev. D, 92(3):033016, 2015.

[54] Georges Aad et al. Search for Higgs and Z Boson Decays to $J/\psi\gamma$ and $\Upsilon(n\mathrm{S})\gamma$ with the ATLAS Detector. Phys. Rev. Lett., 114(12):121801, 2015.

[55] Morad Aaboud et al. Searches for exclusive Higgs and Z boson decays into $J/\psi\gamma$, $\psi(2S)\gamma$, and $\Upsilon(nS)\gamma$ at $\sqrt{s}$ = 13 TeV with the ATLAS detector. Phys. Lett. B, 786:134–155, 2018.

[56] Albert M Sirunyan et al. Search for rare decays of Z and Higgs bosons to J/ψ and a photon in proton-proton collisions at $\sqrt{s} = 13$ TeV. Eur. Phys. J. C, 79(2):94, 2019.

[57] Search for the Standard Model Higgs and Z Boson decays to $J/\psi\,\gamma$: HL-LHC projections. ATL-PHYS-PUB-2015-043, 2015.

[58] Matthias König and Matthias Neubert. Exclusive Radiative Higgs Decays as Probes of Light-Quark Yukawa Couplings. JHEP, 08:012, 2015.

[59] M. Cepeda et al. Report from Working Group 2: Higgs Physics at the HL-LHC and HE-LHC. CERN Yellow Rep. Monogr., 7:221–584, 2019.

[60] Ilaria Brivio, Florian Goertz, and Gino Isidori. Probing the Charm Quark Yukawa Coupling in Higgs+Charm Production. Phys. Rev. Lett., 115(21):211801, 2015.

[61] Nina M. Coyle, Carlos E. M. Wagner, and Viska Wei. Bounding the charm Yukawa coupling. Phys. Rev. D, 100(7):073013, 2019.

[62] J. de Blas et al. Higgs Boson Studies at Future Particle Colliders. JHEP, 01:139, 2020.

[63] Linda M. Carpenter, Tao Han, Khalida Hendricks, Zhuoni Qian, and Ning Zhou. Higgs Boson Decay to Light Jets at the LHC. Phys. Rev. D, 95(5):053003, 2017.

[64] Yotam Soreq, Hua Xing Zhu, and Jure Zupan. Light quark yukawa couplings from higgs kinematics. Journal of High Energy Physics, 2016(12), Dec 2016.

[65] Jonathan Cohen, Shaouly Bar-Shalom, Gad Eilam, and Amarjit Soni. Light-quarks Yukawa couplings and new physics in exclusive high- p_T Higgs boson+jet and Higgs boson + b -jet events. Phys. Rev. D, 97(5):055014, 2018.

[66] Fady Bishara, Ulrich Haisch, Pier Francesco Monni, and Emanuele Re. Constraining Light-Quark Yukawa Couplings from Higgs Distributions. Phys. Rev. Lett., 118(12):121801, 2017.

[67] Albert M Sirunyan et al. Measurement and interpretation of differential cross sections for Higgs boson production at $\sqrt{s} = 13$ TeV. Phys. Lett. B, 792:369–396, 2019.

[68] Felix Yu. Phenomenology of Enhanced Light Quark Yukawa Couplings and the $W^{\pm}h$ Charge Asymmetry. JHEP, 02:083, 2017.

[69] Lina Alasfar, Roberto Corral Lopez, and Ramona Gröber. Probing Higgs couplings to light quarks via Higgs pair production. JHEP, 11:088, 2019.

[70] Daniel Egana-Ugrinovic, Samuel Homiller, and Patrick Meade. Multi-Higgs Production Probes Higgs Flavor, 1 2021.

[71] Hamzeh Khanpour, Sara Khatibi, and Mojtaba Mohammadi Najafabadi. Probing Higgs boson couplings in H+γ production at the LHC. Phys. Lett. B, 773:462–469, 2017.

[72] Tao Han, Benjamin Nachman, and Xing Wang. Charm-quark Yukawa Coupling in $h \to c\bar{c}\gamma$ at LHC. Phys. Lett. B, 793:90–96, 2019.

[73] J. A. Aguilar-Saavedra, J. M. Cano, and J. M. No. More light on Higgs flavor at the LHC: Higgs couplings to light quarks through $h + \gamma$ production, 8 2020.

[74] Barbara Mele. Rescuing $H \to b\bar{b}$ in VBF at the LHC by requiring a central photon. In 19th Conference on High Energy Physics, 10 2007.

[75] Emidio Gabrielli, Fabio Maltoni, Barbara Mele, Mauro Moretti, Fulvio Piccinini, and Roberto Pittau. Higgs Boson Production in Association with a Photon in Vector Boson Fusion at the LHC. Nucl. Phys. B, 781:64–84, 2007.

[76] F. Piccinini. H $\rightarrow b\bar{b}$ in VBF at the LHC with an extra central photon. Nuovo Cim. C, 32N5-6:323–328, 2009.

[77] D. Asner, M. Cunningham, S. Dejong, K. Randrianarivony, C. Santamarina Rios, and M. Schram. Search for a Light Standard Model Higgs Boson Produced in Association with a Photon in Vector Boson Fusion, 6 2010.

[78] Ken Arnold, Terrance Figy, Barbara Jager, and Dieter Zeppenfeld. Higgs boson production in association with a photon via weak boson fusion. In International Conference on the Structure and Interactions of the Photon and 19th International W 10 2011.

[79] Emidio Gabrielli, Barbara Mele, Fulvio Piccinini, and Roberto Pittau. Asking for an extra photon in Higgs production at the LHC and beyond. JHEP, 07:003, 2016.

[80] Anke Biekötter, Raquel Gomez-Ambrosio, Parisa Gregg, Frank Krauss, and Marek Schönherr. Constraining SMEFT operators with associated $h\gamma$ production in weak boson fusion. Phys. Lett. B, 814:136079, 2021.

[81] D. de Florian et al. Handbook of LHC Higgs Cross Sections: 4. Deciphering the Nature of the Higgs Sector, 10 2016.

[82] J. Alwall, R. Frederix, S. Frixione, V. Hirschi, F. Maltoni, O. Mattelaer, H. S. Shao, T. Stelzer, P. Torrielli, and M. Zaro. The automated computation of tree-level and next-to-leading order differential cross sections, and their matching to parton shower simulations. JHEP, 07:079, 2014.

[83] Jon Butterworth et al. PDF4LHC recommendations for LHC Run II. J. Phys. G, 43:023001, 2016.

[84] Pierre Artoisenet, Rikkert Frederix, Olivier Mattelaer, and Robbert Rietkerk. Automatic spin-entangled decays of heavy resonances in Monte Carlo simulations. JHEP, 03:015, 2013.

[85] Torbjörn Sjöstrand, Stefan Ask, Jesper R. Christiansen, Richard Corke, Nishita Desai, Philip Ilten, Stephen Mrenna, Stefan Prestel, Christine O. Rasmussen, and Peter Z. Skands. An Introduction to PYTHIA 8.2. Comput. Phys. Commun., 191:159–177, 2015.

[86] S. Ovyn, X. Rouby, and V. Lemaitre. DELPHES, a framework for fast simulation of a generic collider experiment. 2009.

[87] J. de Favereau, C. Delaere, P. Demin, A. Giammanco, V. Lemaître, A. Mertens, and M. Selvaggi. DELPHES 3, A modular framework for fast simulation of a generic collider experiment. JHEP, 02:057, 2014.

[88] Matteo Cacciari, Gavin P. Salam, and Gregory Soyez. The anti-k_t jet clustering algorithm. JHEP, 04:063, 2008.

[89] Morad Aaboud et al. Performance of the ATLAS Trigger System in 2015. Eur. Phys. J. C, 77(5):317, 2017.

[90] CMS Collaboration. The CMS trigger system. JINST, 12:P01020, 2017.

[91] Georges Aad et al. Performance of electron and photon triggers in ATLAS during LHC Run 2. Eur. Phys. J. C, 80(1):47, 2020.

[92] 2015 start-up trigger menu and initial performance assessment of the ATLAS trigger using Run-2 data. ATL-DAQ-PUB-2016-001, 2016.

[93] Trigger Menu in 2016. ATL-DAQ-PUB-2017-001, 2017.

[94] Trigger Menu in 2017. ATL-DAQ-PUB-2018-002, 2018.

[95] Trigger menu in 2018. ATL-DAQ-PUB-2019-001, 2019.

[96] Morad Aaboud et al. Search for Higgs bosons produced via vector-boson fusion and decaying into bottom quark pairs in $\sqrt{s} = 13$ TeV pp collisions with the ATLAS detector. Phys. Rev. D, 98(5):052003, 2018.

[97] Georges Aad et al. Search for Higgs boson production in association with a high-energy photon via vector-boson fusion with decay into bottom quark pairs at $\sqrt{s}$=13 TeV with the ATLAS detector, 10 2020.

[98] Georges Aad et al. Performance of the ATLAS Level-1 topological trigger in Run 2, 5 2021.

[99] Oscar J. P. Eboli and D. Zeppenfeld. Observing an invisible Higgs boson. Phys. Lett. B, 495:147–154, 2000.

[100] V. M. Abazov et al. Evidence for production of single top quarks and first direct measurement of —Vtb—. Phys. Rev. Lett., 98:181802, 2007.

[101] Andreas Hoecker, Joerg Stelzer, et al. TMVA - Toolkit for Multivariate Data Analysis, 3 2007.

[102] Probing the $\mathcal{CP}$ nature of the Higgs boson coupling to τ leptons at HL-LHC. ATL-PHYS-PUB-2019-008, 2019.

[103] A. Abada et al. HE-LHC: The High-Energy Large Hadron Collider: Future Circular Collider Conceptual Design Report Volume 4. Eur. Phys. J. ST, 228(5):1109–1382, 2019.

[104] A. Abada et al. FCC-hh: The Hadron Collider: Future Circular Collider Conceptual Design Report Volume 3. Eur. Phys. J. ST, 228(4):755–1107, 2019.

[105] Peter W. Higgs. Broken symmetries and the masses of gauge bosons. Phys. Rev. Lett., 13:508–509, Oct 1964.

[106] F. Englert and R. Brout. Broken symmetry and the mass of gauge vector mesons. Phys. Rev. Lett., 13:321–323, Aug 1964.

[107] G. Aad, T. Abajyan, B. Abbott, J. Abdallah, S. Abdel Khalek, A.A. Abdelalim, O. Abdinov, R. Aben, B. Abi, M. Abolins, and et al. Observation of a new particle in the search for the standard model higgs boson with the atlas detector at the lhc. Physics Letters B, 716(1):1–29, Sep 2012.

[108] S. Chatrchyan, V. Khachatryan, A.M. Sirunyan, A. Tumasyan, W. Adam, E. Aguilo, T. Bergauer, M. Dragicevic, J. Erö, C. Fabjan, and et al. Observation of a new boson at a mass of 125 gev with the cms experiment at the lhc. Physics Letters B, 716(1):30–61, Sep 2012.

[109] Nikolas Kauer and Giampiero Passarino. Inadequacy of zero-width approximation for a light Higgs boson signal. JHEP, 08:116, 2012.

[110] Fabrizio Caola and Kirill Melnikov. Constraining the Higgs boson width with ZZ production at the LHC. Phys. Rev., D88:054024, 2013.

[111] John M. Campbell, R. Keith Ellis, and Ciaran Williams. Bounding the Higgs width at the LHC using full analytic results for $gg- > e^-e^+\mu^-\mu^+$. JHEP, 04:060, 2014.

[112] Morad Aaboud et al. Constraints on off-shell Higgs boson production and the Higgs boson total width in $ZZ \to 4\ell$ and $ZZ \to 2\ell 2\nu$ final states with the ATLAS detector. Phys. Lett. B, 786:223–244, 2018.

[113] Albert M Sirunyan et al. Measurements of the Higgs boson width and anomalous HVV couplings from on-shell and off-shell production in the four-lepton final state. Phys. Rev. D, 99(11):112003, 2019.

[114] James S. Gainer, Joseph Lykken, Konstantin T. Matchev, Stephen Mrenna, and Myeonghun Park. Beyond Geolocating: Constraining Higher Dimensional Operators in $H \to 4\ell$ with Off-Shell Production and More. Phys. Rev. D, 91(3):035011, 2015.

[115] Giacomo Cacciapaglia, Aldo Deandrea, Guillaume Drieu La Rochelle, and Jean-Baptiste Flament. Higgs couplings: disentangling New Physics with off-shell measurements. Phys. Rev. Lett., 113(20):201802, 2014.

[116] Aleksandr Azatov, Christophe Grojean, Ayan Paul, and Ennio Salvioni. Taming the off-shell Higgs boson. Zh. Eksp. Teor. Fiz., 147:410–425, 2015.

[117] Christoph Englert and Michael Spannowsky. Limitations and Opportunities of Off-Shell Coupling Measurements. Phys. Rev. D, 90:053003, 2014.

[118] Malte Buschmann, Dorival Goncalves, Silvan Kuttimalai, Marek Schonherr, Frank Krauss, and Tilman Plehn. Mass Effects in the Higgs-Gluon Coupling: Boosted vs Off-Shell Production. JHEP, 02:038, 2015.

[119] Tyler Corbett, Oscar J. P. Eboli, Dorival Goncalves, J. Gonzalez-Fraile, Tilman Plehn, and Michael Rauch. The Higgs Legacy of the LHC Run I. JHEP, 08:156, 2015.

[120] Dorival Goncalves, Tao Han, and Satyanarayan Mukhopadhyay. Off-Shell Higgs Probe of Naturalness. Phys. Rev. Lett., 120(11):111801, 2018. [Erratum: Phys.Rev.Lett. 121, 079902 (2018)].

[121] Dorival Gonçalves, Tao Han, and Satyanarayan Mukhopadhyay. Higgs Couplings at High Scales. Phys. Rev., D98(1):015023, 2018.

[122] Christoph Englert, Yotam Soreq, and Michael Spannowsky. Off-Shell Higgs Coupling Measurements in BSM scenarios. JHEP, 05:145, 2015.

[123] Valentin Hirschi and Olivier Mattelaer. Automated event generation for loop-induced processes. JHEP, 10:146, 2015.

[124] Stefano Frixione and Bryan R. Webber. Matching NLO QCD computations and parton shower simulations. JHEP, 06:029, 2002.

[125] Marco Bonvini, Fabrizio Caola, Stefano Forte, Kirill Melnikov, and Giovanni Ridolfi. Signal-background interference effects for $gg \to H \to W^+W^-$ beyond leading order. Phys. Rev., D88(3):034032, 2013.

[126] Richard D. Ball, Valerio Bertone, Stefano Carrazza, Luigi Del Debbio, Stefano Forte, Alberto Guffanti, Nathan P. Hartland, and Juan Rojo. Parton distributions with QED corrections. Nucl. Phys., B877:290–320, 2013.

[127] Andreas Hoecker, Peter Speckmayer, Joerg Stelzer, Jan Therhaag, Eckhard von Toerne, and Helge Voss. TMVA: Toolkit for Multivariate Data Analysis. PoS, ACAT:040, 2007.

[128] Dorival Goncalves and Junya Nakamura. Role of the Z polarization in the $H \to b\bar{b}$ measurement. Phys. Rev., D98(9):093005, 2018.

[129] Dorival Goncalves and Junya Nakamura. Boosting the $H \to$ invisibles searches with Z boson polarization. Phys. Rev., D99(5):055021, 2019.

[130] John C. Collins and Davison E. Soper. Angular Distribution of Dileptons in High-Energy Hadron Collisions. Phys. Rev., D16:2219, 1977.

[131] Dorival Goncalves, Tilman Plehn, and Jennifer M. Thompson. Weak boson fusion at 100 TeV. Phys. Rev., D95(9):095011, 2017.

[132] Thomas Appelquist and J. Carazzone. Infrared Singularities and Massive Fields. Phys. Rev. D, 11:2856, 1975.

[133] W. Buchmuller and D. Wyler. Effective Lagrangian Analysis of New Interactions and Flavor Conservation. Nucl. Phys. B, 268:621–653, 1986.

[134] B. Grzadkowski, M. Iskrzynski, M. Misiak, and J. Rosiek. Dimension-Six Terms in the Standard Model Lagrangian. JHEP, 10:085, 2010.

[135] Mikhail A. Shifman, A.I. Vainshtein, M.B. Voloshin, and Valentin I. Zakharov. Low-Energy Theorems for Higgs Boson Couplings to Photons. Sov. J. Nucl. Phys., 30:711–716, 1979.

[136] Bernd A. Kniehl and Michael Spira. Low-energy theorems in Higgs physics. Z. Phys. C, 69:77–88, 1995.

[137] U. Baur and E.W.Nigel Glover. Higgs Boson Production at Large Transverse Momentum in Hadronic Collisions. Nucl. Phys. B, 339:38–66, 1990.

[138] Robert V. Harlander and Tobias Neumann. Probing the nature of the Higgs-gluon coupling. Phys. Rev. D, 88:074015, 2013.

[139] Andrea Banfi, Adam Martin, and Veronica Sanz. Probing top-partners in Higgs+jets. JHEP, 08:053, 2014.

[140] Aleksandr Azatov and Ayan Paul. Probing Higgs couplings with high p_T Higgs production. JHEP, 01:014, 2014.

[141] Christophe Grojean, Ennio Salvioni, Matthias Schlaffer, and Andreas Weiler. Very boosted Higgs in gluon fusion. JHEP, 05:022, 2014.

[142] Malte Buschmann, Christoph Englert, Dorival Goncalves, Tilman Plehn, and Michael Spannowsky. Resolving the Higgs-Gluon Coupling with Jets. Phys. Rev. D, 90(1):013010, 2014.

[143] Aleksandr Azatov, Christophe Grojean, Ayan Paul, and Ennio Salvioni. Resolving gluon fusion loops at current and future hadron colliders. JHEP, 09:123, 2016.

[144] Michelangelo L. Mangano, Tilman Plehn, Peter Reimitz, Torben Schell, and Hua-Sheng Shao. Measuring the Top Yukawa Coupling at 100 TeV. J. Phys. G, 43(3):035001, 2016.

[145] E.W.Nigel Glover and J.J. van der Bij. Z BOSON PAIR PRODUCTION VIA GLUON FUSION. Nucl. Phys. B, 321:561–590, 1989.

[146] Adam Alloul, Neil D. Christensen, Céline Degrande, Claude Duhr, and Benjamin Fuks. FeynRules 2.0 - A complete toolbox for tree-level phenomenology. Comput. Phys. Commun., 185:2250–2300, 2014.

[147] Celine Degrande. Automatic evaluation of UV and R2 terms for beyond the Standard Model Lagrangians: a proof-of-principle. Comput. Phys. Commun., 197:239–262, 2015.

[148] Céline Degrande, Claude Duhr, Benjamin Fuks, David Grellscheid, Olivier Mattelaer, and Thomas Reiter. Ufo – the universal feynrules output. Computer Physics Communications, 183(6):1201–1214, Jun 2012.

[149] Alex Pomarol and Francesco Riva. The Composite Higgs and Light Resonance Connection. JHEP, 08:135, 2012.

[150] Giuliano Panico and Andrea Wulzer. The Discrete Composite Higgs Model. JHEP, 09:135, 2011.

[151] Giuliano Panico and Andrea Wulzer. The Composite Nambu-Goldstone Higgs. Lect. Notes Phys., 913:pp.1–316, 2016.

[152] Da Liu, Ian Low, and Carlos E. M. Wagner. Modification of Higgs Couplings in Minimal Composite Models. Phys. Rev., D96(3):035013, 2017.

[153] V. Punjabi, C. F. Perdrisat, M. K. Jones, E. J. Brash, and C. E. Carlson. The Structure of the Nucleon: Elastic Electromagnetic Form Factors. Eur. Phys. J., A51:79, 2015.

[154] Christopher T. Hill and Elizabeth H. Simmons. Strong Dynamics and Electroweak Symmetry Breaking. Phys. Rept., 381:235–402, 2003. [Erratum: Phys.Rept. 390, 553–554 (2004)].

[155] Dario Buttazzo, Giuseppe Degrassi, Pier Paolo Giardino, Gian F. Giudice, Filippo Sala, Alberto Salvio, and Alessandro Strumia. Investigating the near-criticality of the Higgs boson. JHEP, 12:089, 2013.

[156] Fedor Bezrukov and Mikhail Shaposhnikov. Why should we care about the top quark Yukawa coupling? J. Exp. Theor. Phys., 120:335–343, 2015.

[157] Marcela Carena, M. Olechowski, S. Pokorski, and C. E. M. Wagner. Radiative electroweak symmetry breaking and the infrared fixed point of the top quark mass. Nucl. Phys. B, 419:213–239, 1994.

[158] Oleksii Matsedonskyi, Giuliano Panico, and Andrea Wulzer. Light Top Partners for a Light Composite Higgs. JHEP, 01:164, 2013.

[159] Brando Bellazzini, Csaba Csáki, and Javi Serra. Composite Higgses. Eur. Phys. J. C, 74(5):2766, 2014.

[160] Georges Aad et al. Combined measurements of Higgs boson production and decay using up to 80 fb^{-1} of proton-proton collision data at $\sqrt{s} = 13$ TeV collected with the ATLAS experiment. Phys. Rev. D, 101(1):012002, 2020.

[161] Dorival Gonçalves, Tao Han, Sze Ching Iris Leung, and Han Qin. Off-shell Higgs couplings in $H^* \to ZZ \to \ell\ell\nu\nu$. Phys. Lett. B, 817:136329, 2021.

[162] John Ellis, Maeve Madigan, Ken Mimasu, Veronica Sanz, and Tevong You. Top, Higgs, Diboson and Electroweak Fit to the Standard Model Effective Field Theory. 12 2020.

[163] Jacob J. Ethier, Fabio Maltoni, Luca Mantani, Emanuele R. Nocera, Juan Rojo, Emma Slade, Eleni Vryonidou, and Cen Zhang. Combined SMEFT interpretation of Higgs, diboson, and top quark data from the LHC. 4 2021.

[164] Ilaria Brivio, Sebastian Bruggisser, Fabio Maltoni, Rhea Moutafis, Tilman Plehn, Eleni Vryonidou, Susanne Westhoff, and C. Zhang. O new physics, where art thou? A global search in the top sector. JHEP, 02:131, 2020.

[165] Anke Biekötter, Dorival Gonçalves, Tilman Plehn, Michihisa Takeuchi, and Dirk Zerwas. The global Higgs picture at 27 TeV. SciPost Phys., 6(2):024, 2019.

[166] Fabio Maltoni, Eleni Vryonidou, and Cen Zhang. Higgs production in association with a top-antitop pair in the Standard Model Effective Field Theory at NLO in QCD. JHEP, 10:123, 2016.

[167] A combination of measurements of Higgs boson production and decay using up to 139 fb^{-1} of proton–proton collision data at $\sqrt{s} = 13$ TeV collected with the ATLAS experiment. Technical report, CERN, Geneva, Aug 2020.

[168] Albert M Sirunyan et al. Measurement of the top quark polarization and $\mathrm{t\bar{t}}$ spin correlations using dilepton final states in proton-proton collisions at $\sqrt{s} = 13$ TeV. Phys. Rev. D, 100(7):072002, 2019.

[169] Avik Banerjee, Sayan Dasgupta, and Tirtha Sankar Ray. Chasing the Higgs shape at HL-LHC. 5 2021.

[170] Céline Degrande, Gauthier Durieux, Fabio Maltoni, Ken Mimasu, Eleni Vryonidou, and Cen Zhang. Automated one-loop computations in the SMEFT. 8 2020.

[171] Reza Goldouzian, Jeong Han Kim, Kevin Lannon, Adam Martin, Kelci Mohrman, and Andrew Wightman. Matching in $pp \to t\bar{t}W/Z/h+$ jet SMEFT studies. 12 2020.

[172] Peter Skands, Stefano Carrazza, and Juan Rojo. Tuning PYTHIA 8.1: the Monash 2013 Tune. Eur. Phys. J. C, 74(8):3024, 2014.

[173] L. A. Harland-Lang, A. D. Martin, P. Motylinski, and R. S. Thorne. Parton distributions in the LHC era: MMHT 2014 PDFs. Eur. Phys. J. C, 75(5):204, 2015.

[174] Matthew R. Buckley and Dorival Goncalves. Boosting the Direct CP Measurement of the Higgs-Top Coupling. Phys. Rev. Lett., 116(9):091801, 2016.

[175] Matteo Cacciari, Gavin P. Salam, and Gregory Soyez. FastJet User Manual. Eur. Phys. J. C, 72:1896, 2012.

[176] Jonathan M. Butterworth, Adam R. Davison, Mathieu Rubin, and Gavin P. Salam. Jet substructure as a new Higgs search channel at the LHC. Phys. Rev. Lett., 100:242001, 2008.

[177] Tilman Plehn, Gavin P. Salam, and Michael Spannowsky. Fat Jets for a Light Higgs. Phys. Rev. Lett., 104:111801, 2010.

[178] Technical Design Report for the ATLAS Inner Tracker Pixel Detector. Technical Report CERN-LHCC-2017-021. ATLAS-TDR-030, CERN, Geneva, Sep 2017.

[179] Using associated top quark production to probe for new physics within the framework of effective field theory. Technical report, CERN, Geneva, 2020.

[180] Georges Aad et al. Observation of a new particle in the search for the Standard Model Higgs boson with the ATLAS detector at the LHC. Phys. Lett. B, 716:1–29, 2012.

[181] Serguei Chatrchyan et al. Observation of a New Boson at a Mass of 125 GeV with the CMS Experiment at the LHC. Phys. Lett. B, 716:30–61, 2012.

[182] Steven Weinberg. Implications of Dynamical Symmetry Breaking. Phys. Rev. D, 13:974–996, 1976. [Addendum: Phys.Rev.D 19, 1277–1280 (1979)].

[183] Eldad Gildener. Gauge Symmetry Hierarchies. Phys. Rev. D, 14:1667, 1976.

[184] Gerard 't Hooft, C. Itzykson, A. Jaffe, H. Lehmann, P. K. Mitter, I. M. Singer, and R. Stora, editors. Recent Developments in Gauge Theories. Proceedings, Nato Advanced Study Institute, Cargese, F volume 59, 1980.

[185] Roshan Mammen Abraham, Dorival Gonçalves, Tao Han, Sze Ching Iris Leung, and Han Qin. Directly probing the Higgs-top coupling at high scales. Phys. Lett. B, 825:136839, 2022.

[186] Benjamin W. Lee, C. Quigg, and H. B. Thacker. Weak Interactions at Very High-Energies: The Role of the Higgs Boson Mass. Phys. Rev. D, 16:1519, 1977.

[187] Benjamin W. Lee, C. Quigg, and H. B. Thacker. The Strength of Weak Interactions at Very High-Energies and the Higgs Boson Mass. Phys. Rev. Lett., 38:883–885, 1977.

[188] Abdus Salam and John Clive Ward. Electromagnetic and weak interactions. Phys. Lett., 13:168–171, 1964.

[189] Michael Rauch. Vector-Boson Fusion and Vector-Boson Scattering. 10 2016.

[190] Daniel R. Green, Patrick Meade, and Marc-Andre Pleier. Multiboson interactions at the LHC. Rev. Mod. Phys., 89(3):035008, 2017.

[191] C. F. Anders et al. Vector boson scattering: Recent experimental and theory developments. Rev. Phys., 3:44–63, 2018.

[192] Riccardo Bellan et al. VBSCan Thessaloniki 2018 Workshop Summary. In 2nd Vector Boson Scattering Coordination and Action Network Annual Meeting, 6 2019.

[193] Julien Baglio et al. VBSCan Mid-Term Scientific Meeting. In VBSCan Mid-Term Scientific Meeting, 4 2020.

[194] Roberto Covarelli, Mathieu Pellen, and Marco Zaro. Vector-Boson scattering at the LHC: Unraveling the electroweak sector. Int. J. Mod. Phys. A, 36(16):2130009, 2021.

[195] Georges Aad et al. Combined search for the Standard Model Higgs boson in pp collisions at $\sqrt{s} = 7$ TeV with the ATLAS detector. Phys. Rev. D, 86:032003, 2012.

[196] Serguei Chatrchyan et al. Combined results of searches for the standard model Higgs boson in pp collisions at $\sqrt{s} = 7$ TeV. Phys. Lett. B, 710:26–48, 2012.

[197] Jack Y. Araz, Shankha Banerjee, Rick S. Gupta, and Michael Spannowsky. Precision SMEFT bounds from the VBF Higgs at high transverse momentum. JHEP, 04:125, 2021.

[198] Shankha Banerjee, Satyanarayan Mukhopadhyay, and Biswarup Mukhopadhyaya. Higher dimensional operators and the LHC Higgs data: The role of modified kinematics. Phys. Rev. D, 89(5):053010, 2014.

[199] John Ellis, Veronica Sanz, and Tevong You. Complete Higgs Sector Constraints on Dimension-6 Operators. JHEP, 07:036, 2014.

[200] Raquel Gomez-Ambrosio. Studies of Dimension-Six EFT effects in Vector Boson Scattering. Eur. Phys. J. C, 79(5):389, 2019.

[201] Jacob J. Ethier, Raquel Gomez-Ambrosio, Giacomo Magni, and Juan Rojo. SMEFT analysis of vector boson scattering and diboson data from the LHC Run II. Eur. Phys. J. C, 81(6):560, 2021.

[202] Tisa Biswas, Anindya Datta, and Biswarup Mukhopadhyaya. Following the trail of new physics via the vector boson fusion Higgs boson signal at the Large Hadron Collider. Phys. Rev. D, 105(5):055028, 2022.

[203] Haeyun Hwang, Ui Min, Junghyeon Park, Minho Son, and Jae Hyeok Yoo. Anomalous triple gauge couplings in electroweak dilepton tails at the LHC and interference resurrection. 1 2023.

[204] Roberto Franceschini, Giuliano Panico, Alex Pomarol, Francesco Riva, and Andrea Wulzer. Electroweak Precision Tests in High-Energy Diboson Processes. JHEP, 02:111, 2018.

[205] Da Liu and Lian-Tao Wang. Prospects for precision measurement of diboson processes in the semileptonic decay channel in future LHC runs. Phys. Rev. D, 99(5):055001, 2019.

[206] Shankha Banerjee, Christoph Englert, Rick S. Gupta, and Michael Spannowsky. Probing Electroweak Precision Physics via boosted Higgs-strahlung at the LHC. Phys. Rev. D, 98(9):095012, 2018.

[207] Christophe Grojean, Marc Montull, and Marc Riembau. Diboson at the LHC vs LEP. JHEP, 03:020, 2019.

[208] A. Azatov, D. Barducci, and E. Venturini. Precision diboson measurements at hadron colliders. JHEP, 04:075, 2019.

[209] Felipe F. Freitas, Charanjit K. Khosa, and Verónica Sanz. Exploring the standard model EFT in VH production with machine learning. Phys. Rev. D, 100(3):035040, 2019.

[210] Shankha Banerjee, Rick S. Gupta, Joey Y. Reiness, and Michael Spannowsky. Resolving the tensor structure of the Higgs coupling to Z-bosons via Higgs-strahlung. Phys. Rev. D, 100(11):115004, 2019.

[211] Johann Brehmer, Sally Dawson, Samuel Homiller, Felix Kling, and Tilman Plehn. Benchmarking simplified template cross sections in WH production. JHEP, 11:034, 2019.

[212] Wen Han Chiu, Zhen Liu, and Lian-Tao Wang. Probing flavor nonuniversal theories through Higgs physics at the LHC and future colliders. Phys. Rev. D, 101(3):035045, 2020.

[213] Shankha Banerjee, Rick S. Gupta, Joey Y. Reiness, Satyajit Seth, and Michael Spannowsky. Towards the ultimate differential SMEFT analysis. JHEP, 09:170, 2020.

[214] Julien Baglio, Sally Dawson, Samuel Homiller, Samuel D. Lane, and Ian M. Lewis. Validity of standard model EFT studies of VH and VV production at NLO. Phys. Rev. D, 101(11):115004, 2020.

[215] Fady Bishara, Philipp Englert, Christophe Grojean, Marc Montull, Giuliano Panico, and Alejo N. Rossia. A New Precision Process at FCC-hh: the diphoton leptonic Wh channel. JHEP, 07:075, 2020.

[216] Fady Bishara, Stefania De Curtis, Luigi Delle Rose, Philipp Englert, Christophe Grojean, Marc Montull, Giuliano Panico, and Alejo N. Rossia. Precision from the diphoton Zh channel at FCC-hh. JHEP, 04:154, 2021.

[217] Li Huang, Samuel D. Lane, Ian M. Lewis, and Zhen Liu. Electroweak Restoration at the LHC and Beyond: The Vh Channel. Phys. Rev. D, 103(5):053007, 2021.

[218] Fady Bishara, Philipp Englert, Christophe Grojean, Giuliano Panico, and Alejo N. Rossia. Revisiting $\mathbf{Vh}(\to \mathbf{b\bar{b}})$ at the LHC and FCC-hh. 8 2022.

[219] Aneesh Manohar and Howard Georgi. Chiral Quarks and the Nonrelativistic Quark Model. Nucl. Phys. B, 234:189–212, 1984.

[220] H. Georgi. Weak Interactions and Modern Particle Theory. Dover, 1984.

[221] G. F. Giudice, C. Grojean, A. Pomarol, and R. Rattazzi. The Strongly-Interacting Light Higgs. JHEP, 06:045, 2007.

[222] Da Liu, Alex Pomarol, Riccardo Rattazzi, and Francesco Riva. Patterns of Strong Coupling for LHC Searches. JHEP, 11:141, 2016.

[223] Pedro Bittar and Gustavo Burdman. Form factors in Higgs couplings from physics beyond the standard model. JHEP, 10:004, 2022.

[224] Johan Alwall, Michel Herquet, Fabio Maltoni, Olivier Mattelaer, and Tim Stelzer. MadGraph 5 : Going Beyond. JHEP, 06:128, 2011.

[225] Admir Greljo, Gino Isidori, Jonas M. Lindert, David Marzocca, and Hantian Zhang. Electroweak Higgs production with HiggsPO at NLO QCD. Eur. Phys. J. C, 77(12):838, 2017.

[226] Georges Aad et al. Evidence of off-shell Higgs boson production from ZZ leptonic decay channels and constraints on its total width with the ATLAS detector. 4 2023.

[227] Johann Brehmer, Felix Kling, Irina Espejo, and Kyle Cranmer. MadMiner: Machine learning-based inference for particle physics. Comput. Softw. Big Sci., 4(1):3, 2020.

[228] Morad Aaboud et al. Search for the standard model Higgs boson produced in association with top quarks and decaying into a $b\bar{b}$ pair in pp collisions at $\sqrt{s} = 13$ TeV with the ATLAS detector. Phys. Rev. D, 97(7):072016, 2018.

[229] Tomáš Ježo, Jonas M. Lindert, Niccolo Moretti, and Stefano Pozzorini. New NLOPS predictions for $t\bar{t} + b$ -jet production at the LHC. Eur. Phys. J. C, 78(6):502, 2018.

[230] Ansgar Denner, Jean-Nicolas Lang, and Mathieu Pellen. Full NLO QCD corrections to off-shell tt¯bb¯ production. Phys. Rev. D, 104(5):056018, 2021.

[231] Giuseppe Bevilacqua, Huan-Yu Bi, Heribertus Bayu Hartanto, Manfred Kraus, Michele Lupattelli, and Malgorzata Worek. $t\bar{t}b\bar{b}$ at the LHC: on the size of corrections and b-jet definitions. JHEP, 08:008, 2021.